

**Hemodynamic Indices and Shape-Based Models of Left Atrial Appendage to Enhance Stroke Prediction in Atrial Fibrillation**

by

**Soroosh Sanatkhani**

B.Sc., Automotive Engineering, Iran University of Science & Technology, 2013

M.Sc., Mechanical Engineering-Energy Conversion, Sharif University of Technology, 2016

Submitted to the Graduate Faculty of the  
Swanson School of Engineering in partial fulfillment  
of the requirements for the degree of  
Doctor of Philosophy

University of Pittsburgh

2021

UNIVERSITY OF PITTSBURGH  
SWANSON SCHOOL OF ENGINEERING

This dissertation was presented

by

**Soroosh Sanatkhani**

It was defended on

August 18, 2021

and approved by

Harvey Borovetz, PhD, Distinguished Professor, Department of Bioengineering

William J. Federspiel, PhD, John A. Swanson Professor, Department of Bioengineering

Sandeep Jain, MD, Professor, Department of Medicine

Ramakrishna Mukkamala, PhD, Professor, Department of Bioengineering and Anesthesiology &  
Perioperative Medicine

Samir Saba, MD, Professor, Department of Medicine

Dissertation Co-Director: Prahlad Menon, PhD, Assistant Professor, Department of  
Bioengineering

Dissertation Director: Sanjeev Shroff, PhD, Distinguished Professor, Department of  
Bioengineering

Copyright © by Soroosh Sanatkhani

2021

# Hemodynamic Indices and Shape-Based Models of Left Atrial Appendage to Enhance Stroke Prediction in Atrial Fibrillation

Soroosh Sanatkhani, PhD

University of Pittsburgh, 2021

Atrial fibrillation (AF) is the most common arrhythmia that leads to thrombus formation, mostly in the left atrial appendage (LAA). The current standard of stratifying stroke risk, based on the CHA<sub>2</sub>DS<sub>2</sub>-VASc score, does not consider LAA morphology/hemodynamics. The aim of this study was to determine whether LAA morphology and hemodynamics-based indices can stratify stroke risk independent of CHA<sub>2</sub>DS<sub>2</sub>-VASc score, left atrium size, and AF type. In a retrospective matched case-control study, patient-specific measurements in 128 AF patients included left atrial (LA) and LAA 3D geometry obtained by cardiac computed tomography, heart rate, cardiac output, and hematocrit. We quantified patient-specific 3D LAA morphology in terms of a novel LAA appearance complexity index (LAA-*ACI*) and employed computational fluid dynamics (CFD) analysis to quantify LAA mean residence time,  $t_m$  and asymptotic concentration,  $C_\infty$  of blood-borne particles.

Effects of confounding variables were examined to optimize the CFD analysis. cardiac output, but not by the temporal pattern of pulmonary vein inlet flow, significantly affected LAA  $t_m$ . Both the hematocrit level and the blood rheology model (Newtonian vs. non-Newtonian) also significantly affected LAA  $t_m$ . Finally, 10,000 s was found to be a sufficient length of CFD simulation to calculate LAA  $t_m$  in a consistent and reliable manner.

LAA  $t_m$  varied significantly within a given LAA morphology as defined by the current subjective method, and it was not simply a reflection of LAA geometry/appearance. In addition,

LAA- $ACI$  and  $t_m$  varied significantly for a given CHA<sub>2</sub>DS<sub>2</sub>-VASc score, indicating that these two indices of stasis are not simply a reflection of the subjects' clinical status. Using multiple logistic regression, we observed that  $ACI$ ,  $t_m$ , and  $C_\infty$  had a modest, but statistically insignificant performance in predicting stroke (area under the ROC curve = 0.56–0.61). The temporal dissociation between adverse changes in LAA shape and hemodynamics-based indices and the actual stroke event can contribute to the negative result; a longitudinal study is necessary to address this issue. In addition, it is possible that a multiscale model that combines CFD-based hemodynamics simulation and biology-based thrombus formation can yield indices that can better stratify stroke risk in AF patients.

# Table of Contents

<b>Preface.....</b>	<b>xv</b>
<b>Abbreviations and Symbols .....</b>	<b>xvi</b>
<b>1.0 Introduction.....</b>	<b>1</b>
<b>1.1 Left Atrium Anatomy and Electrophysiology .....</b>	<b>1</b>
<b>1.2 Atrial Fibrillation, The Most Common Arrhythmia.....</b>	<b>2</b>
<b>1.3 Current AF Management Guidelines .....</b>	<b>4</b>
<b>1.3.1 Rate Control .....</b>	<b>6</b>
<b>1.3.2 Rhythm Control .....</b>	<b>6</b>
<b>1.3.2.1 Ablation and Atrial Remodeling .....</b>	<b>6</b>
<b>1.3.3 Anticoagulation Therapy.....</b>	<b>7</b>
<b>1.3.4 Left Atrial Appendage Closure Devices.....</b>	<b>10</b>
<b>1.4 Current Clinical Risk Stratification Schemes.....</b>	<b>11</b>
<b>1.5 LAA: The Most Prominent Region for Thrombus Formation in AF.....</b>	<b>12</b>
<b>1.6 Correlation of LAA Appearance/Shape with Stroke Risk .....</b>	<b>13</b>
<b>1.7 Correlation of LAA Hemodynamics with Stroke Risk .....</b>	<b>15</b>
<b>1.7.1 Systems-Based Approach to Quantify Patient-Specific Indices of Thrombosis         Formation Risk.....</b>	<b>16</b>
<b>1.8 Objective and Specific Aims .....</b>	<b>17</b>
<b>1.8.1 Specific Aim 1: Develop a Quantitative Index of LAA Appearance .....</b>	<b>18</b>
<b>1.8.2 Specific Aim 2: Develop a Quantitative Index of LAA Residence Time Using         a Systems Approach.....</b>	<b>18</b>

1.8.3 Specific Aim 3: Develop a Predictive Model to Stratify Stroke Risk Using LAA Appearance and LAA Residence Time Indices .....	18
1.9 Organization of Dissertation .....	19
2.0 Specific Aim 1: Develop a Quantitative Index of LAA Appearance .....	21
2.1 Methodology.....	22
2.1.1 Study Subject Characteristics.....	22
2.1.2 Image Segmentation and Feature Vector Preparation.....	22
2.1.3 Principal Component Analysis (PCA).....	24
2.1.4 LAA Appearance Complexity Index (LAA- <i>ACI</i> ).....	25
2.1.5 Statistical Analysis .....	26
2.2 Results.....	26
2.2.1 Proof of Concept.....	26
2.2.2 Quantitative Characterization .....	29
2.2.3 Minimum Number of Subjects for Principal Component Analysis .....	31
2.2.4 Relating LAA- <i>ACI</i> to Traditional LAA Shape Classification.....	32
2.2.5 Relating LAA- <i>ACI</i> to CHA <sub>2</sub> DS <sub>2</sub> -VASc Score.....	33
2.3 Discussion .....	34
2.3.1 Limitations.....	37
3.0 Specific Aim 2: Develop a Quantitative Index of LAA Residence Time of Blood-Borne Particles Using a Systems Approach.....	39
3.1 Methodology.....	40
3.1.1 Study Subject Characteristics.....	40
3.1.2 Imaging and Segmentation.....	40

3.1.3 Particle image velocimetry .....	42
3.1.4 Meshing .....	44
3.1.5 Governing Equations .....	44
3.1.6 Quemada Viscosity Model.....	46
3.1.7 Boundary Conditions .....	47
3.1.8 OpenFOAM Solvers.....	48
3.1.9 LAA Residence Time of Blood-Borne Particles .....	49
3.2 Results.....	50
3.2.1 CFD Validation .....	50
3.2.2 Confounding Variables.....	53
3.2.2.1 Pulsatility .....	53
3.2.2.2 Hematocrit and Non-Newtonian Fluid .....	57
3.2.2.3 Length of Simulation .....	60
3.2.3 Relating LAA RTD Function to Traditional LAA Shape Classification .....	63
3.2.4 Relating LAA Mean Residence Time to LAA Asymptotic Tracer Concentration .....	65
3.2.5 Relating LAA Mean Residence Time to LAA Appearance Complexity .....	66
3.2.6 Relating LAA Mean Residence Time to CHA <sub>2</sub> DS <sub>2</sub> -VASc Score .....	67
3.3 Discussion .....	68
3.3.1 Limitations .....	72
<b>4.0 Specific Aim 3: Improve CHA<sub>2</sub>DS<sub>2</sub>-VASc-Based Stroke Risk Stratification Using LAA Appearance and LAA Residence Time Indices .....</b>	<b>75</b>
4.1 Methodology.....	77

4.1.1 Study Design .....	77
4.1.2 Data Acquisition .....	77
4.1.3 Statistical Analysis .....	78
4.2 Results.....	79
4.2.1 Patients Characteristics .....	79
4.2.2 Multiple Logistic Regression.....	79
4.3 Discussion .....	81
4.3.1 Limitations.....	85
5.0 Summary and Future Directions.....	87
5.1 Summary .....	87
5.2 Future Directions.....	90
5.2.1 Improving the Current CFD-Based Predictive Model .....	90
5.2.1.1 Patient-Specific Compliant LA/LAA Walls .....	90
5.2.1.2 Incorporation of Blood Thrombosis Biology.....	91
5.2.1.3 Machine Learning to Accelerate the CFD-Based Simulations .....	91
5.2.2 Improving the Study Design.....	92
Appendix A LAA- <i>ACI</i> Calculation .....	93
Appendix A.1 Masking.....	93
Appendix A.2 Reshaping 3D Images into Vectors.....	99
Appendix A.3 Principal Component Analysis .....	100
Appendix B OpenFOAM.....	102
Appendix B.1 ScalarAdvection.....	102
Appendix B.1.1 Sample Simulation Setup Using <i>ScalarAdvection</i> Solver .....	114

<b>Appendix B.2 <i>nonNewtonianDistVel</i></b> .....	<b>117</b>
<b>Appendix B.3 <i>icoFoamDistVel</i></b> .....	<b>125</b>
<b>Appendix B.4 <i>passiveScalarAdvection</i></b> .....	<b>127</b>
<b>Appendix C Curve fitting, Mean Residence Time, Asymptotic Concentration</b> .....	<b>129</b>
<b>Appendix C.1 MATLAB Code for Curve Fitting</b> .....	<b>130</b>
<b>Appendix D Raw Data</b> .....	<b>133</b>
<b>Appendix D.1 Clinical Data</b> .....	<b>133</b>
<b>Appendix D.2 Calculated Hemodynamic and Appearance Indices</b> .....	<b>136</b>
<b>Bibliography</b> .....	<b>140</b>

## List of Tables

<b>Table 1.1 Scoring strategies for CHADS<sub>2</sub> and CHA<sub>2</sub>DS<sub>2</sub>-VASc schemes.....</b>	<b>12</b>
<b>Table 3.1 Quemada viscosity model coefficients .....</b>	<b>47</b>
<b>Table 3.2 PV Blood flow waveform pulsatility indices .....</b>	<b>56</b>
<b>Table 3.3 Spearman rank correlation coefficient for left atrial appendage mean residence time (LAA <math>t_m</math>) obtained with pulmonary vein waveform with no pulsatility and two other waveform types .....</b>	<b>57</b>
<b>Table 4.1 Variables in the multiple logistic regression equation .....</b>	<b>80</b>
<b>Table 4.2 Population and percentage of top 25% and bottom 25% of each variable with respect to the history of prior stroke.....</b>	<b>85</b>
<b>Appendix Table 1 Boundary conditions used with ScalarAdvection solver.....</b>	<b>115</b>
<b>Appendix Table 2 Clinical Data.....</b>	<b>133</b>
<b>Appendix Table 3 Hemodynamic and appearance indices .....</b>	<b>136</b>

## List of Figures

<b>Figure 1.1 Left atrium wall regions.....</b>	<b>2</b>
<b>Figure 1.2 Simplified overall diagram of atrial fibrillation management .....</b>	<b>5</b>
<b>Figure 1.3 Simplified decision making flowchart for anticoagulation in atrial fibrillation... 9</b>	<b>9</b>
<b>Figure 1.4 Clinically identified left atrial appendage shape categories .....</b>	<b>14</b>
<b>Figure 1.5 Systmes-based appraoch to quantify patient-specific indices of thombus formation risk.....</b>	<b>17</b>
<b>Figure 2.1 Flowchart for the left atrial appendage extraction process.....</b>	<b>24</b>
<b>Figure 2.2 Visualization of 16 eigen-shapes created in the principal component analysis... 27</b>	<b>27</b>
<b>Figure 2.3 Reconstructed left atrial appendages using different number of principal components .....</b>	<b>28</b>
<b>Figure 2.4 Visualization of reconstruction two left atrial appendage images using different number of principal components.....</b>	<b>29</b>
<b>Figure 2.5 Left atrial appendage appearance complexity index of three sample subjects... 30</b>	<b>30</b>
<b>Figure 2.6 Left atrial appendage appearacne complexity index (LAA-<i>ACI</i>) and rank order correlation between LAA-<i>ACI</i> calculated using 128 subjects and smaller subcohorts .....</b>	<b>32</b>
<b>Figure 2.7 Left atrial appeadage (LAA) Appearcne Complexity Index (LAA-<i>ACI</i>) variability among traditional shape groups .....</b>	<b>33</b>
<b>Figure 2.8 Relationship between left atrial appendage appearance complexity index and CHA<sub>2</sub>DS<sub>2</sub>-VASc score.....</b>	<b>34</b>
<b>Figure 3.1 LA and LAA segmentation and meshing workflow .....</b>	<b>41</b>

<b>Figure 3.2 Particle Image Velocimetry (PIV) setup.....</b>	<b>43</b>
<b>Figure 3.3 CFD assessment using particle image velocimetry .....</b>	<b>52</b>
<b>Figure 3.4 Three pulmonary vein flow waveform types and their relation with the hemodynamic indices.....</b>	<b>54</b>
<b>Figure 3.5 Blood viscosity as a function of shear strain rate and hematocrit using Quemada viscosity model and Newtonian fluid model .....</b>	<b>58</b>
<b>Figure 3.6 Mean residence time and asymptotic concentration inside left atrial appendage as a function of hematocrit using Newtonian and non-Newtonian models. ....</b>	<b>59</b>
<b>Figure 3.7 Left atrial appendage mean residence time, LAA <math>t_m</math>, and asymptotic concentration, <math>C_\infty</math> as a function of simulation length.....</b>	<b>61</b>
<b>Figure 3.8 Left atrial appendage mean residence time, LAA <math>t_m</math>, and asymptotic concentration, <math>C_\infty</math> rank order correlation coefficient as a function of the length of simulation.....</b>	<b>62</b>
<b>Figure 3.9 Tracer concentration washout, residence time function, and mean residence time intercategory variability .....</b>	<b>65</b>
<b>Figure 3.10 Relationship between the two indices of left atrial appendage (LAA) residence time distribution (RTD) function: mean residence time, <math>t_m</math>, and asymptotic LAA concentration, <math>C_\infty</math>. ....</b>	<b>66</b>
<b>Figure 3.11 Relationship between left atrial appendage (LAA) appearance complexity index (LAA-ACI) and LAA <math>t_m</math>. ....</b>	<b>67</b>
<b>Figure 3.12 Relationship between left atrial appendage mean residence time, LAA <math>t_m</math>, and CHA<sub>2</sub>DS<sub>2</sub>-VASc score.....</b>	<b>68</b>
<b>Figure 4.1 Schematic workflow of the overall study.....</b>	<b>76</b>

**Figure 4.2 Receiver operating characteristic (ROC) curve for prediction of stroke..... 81**

## Preface

Most of all, I thank Professor Sanjeev Shroff for all his science-related guidance, constructive criticism, and overall mentoring during the conduct of the work presented in this dissertation. And of course, special thanks for participating in the long sessions for crafting grants and manuscripts, which helped me secure an American Heart Association Predoctoral Fellowship.

A special thank you to Professor Prahlad Menon, who was instrumental in recruiting me to the University of Pittsburgh bioengineering graduate program. His support throughout my graduate school tenure as a thesis co-advisor and as a friend is greatly appreciated.

Thank you to Dr. Samir Saba, Dr. Sandeep Jain, and Dr. Sotirios Nedios for providing critical clinical input and advice, along with the patient hemodynamic and imaging data. I thank Professor William Federspiel for his valuable feedback regarding the hemodynamics modeling and the calculation of particle residence time.

I acknowledge the funding sources including the Berenfield Graduate Fellowship, Pickard Fellowship, and American Heart Association Predoctoral Fellowship. The resources available at the University of Pittsburgh Center for Research Computing were critical in carrying out the computationally expensive simulations required for the conduct of the current research work.

Thank you to my family who provided tremendous support from far away. Their constant encouragement gave me the energy to persevere and reach my destination. Thank you to my friends, Adam, Kevin, Utkars, Shiv, and Giorgio, who made my graduate school and Pittsburgh experiences very enjoyable. Finally, many thanks to Rachel for making the past couple of years some of the best years of my life.

## Abbreviations and Symbols

---

<b>Abbreviations /Symbols</b>	<b>Definition</b>
AAD	antiarrhythmic drug
<i>ACI</i>	appearance complexity index
AERP	atrial effective refractory period
AF	atrial fibrillation
ANS	autonomous nervous system
$C(t)$	tracer concentration inside the LAA
$C_\infty$	asymptotic concentration remaining inside LAA
CCD	charge-coupled device
CCT	cardiac computed tomography
CFD	computational fluid dynamics
CI	confidence interval
$D/Dt$	material derivative
DCCV	direct current cardioversion
DICOM	digital imaging and communications in medicine
$E(t)$	residence time distribution function
$e_{ij}$	strain rate tensor
GP	ganglionated plexi
<i>Hct</i>	hematocrit
LA	left atrium
LAA	left atrial appendage
$M(t)$	outflow of tracer material from LAA at the LAA ostium
$M_{total}, N_0$	total amount of tracer that will leave the LAA over the period 0 to infinity
OR	odds ratio
p	pressure

*Table (continued)*

$P$	p-value
PC	principal component
PCA	principal component analysis
Pe	Peclet number
PIV	particle image velocimetry
PV	pulmonary vein
PVI	pulmonary vein isolation
$RE(i)$	residual error
ROC	receiver operating characteristic
$RSS(i)$	residual sum of squares
RTD	residence time distribution
TE	thromboembolism
TEE	transesophageal echocardiography
$t_m$	mean residence time
TSS	total sum of squares
$u$	velocity
$\beta$	multiple linear regression coefficient
$\delta$	Kronecker delta
$\delta(t)$	Dirac delta
$\eta$	kinematic viscosity
$\mu$	dynamic viscosity
$\rho$	density; correlation coefficient
$\dot{\gamma}$	strain rate
$\tau_{ij}$	stress tensor
$\mu_a$	blood apparent viscosity
$\mu_p$	plasma viscosity

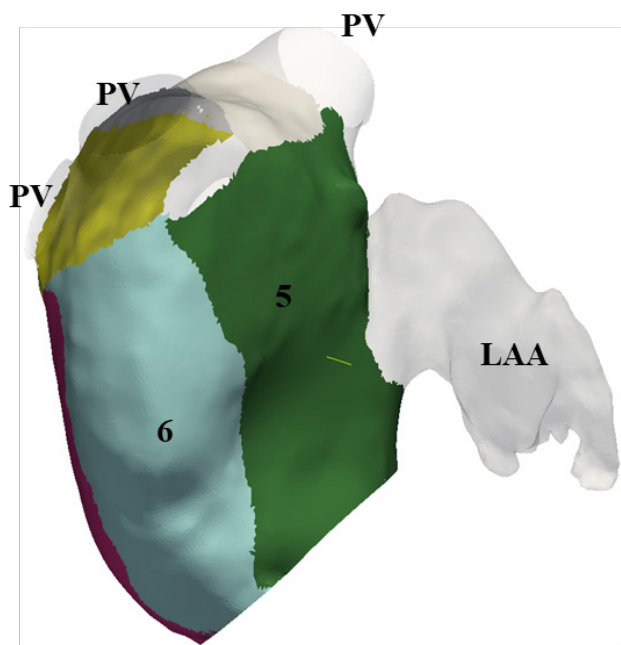
---

## 1.0 Introduction

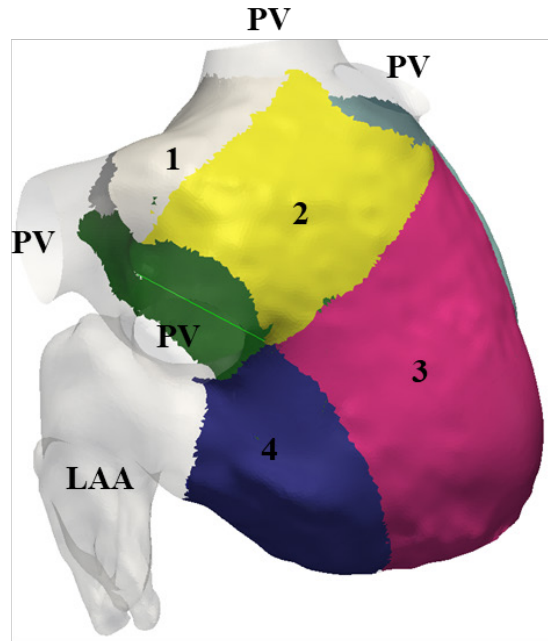
### 1.1 Left Atrium Anatomy and Electrophysiology

LA wall can be segmented into six regions as it is demonstrated in **Figure 1.1**. Left atrium (LA) is situated posterior and superior with respect to the right atrial chamber, and it is separated from the right atrium by the Septum wall. In most cases, two right and two left pulmonary veins (PV) enter the posterior wall of the LA, with the left PVs being superior to the right PVs (Sánchez-Quintana et al., 2014) (**Figure 1.1**). LA has vestibule that leads to mitral valve which is the connection to the left ventricle. The left atrium has a smooth wall in all regions except for the left atrial appendage (LAA) which is the prominent region for thrombus formation in LA (**Section 1.5**). Knowledge of LA/LAA wall geometry is essential for this study as we perform patient-specific LA/LAA geometry reconstruction and hemodynamic modeling of LA/LAA.

An arrhythmia can be initiated by the presence of substrates, triggers, and other altering factors of the electrophysiologic properties. In case of atrial fibrillation (AF), remodeling of atrial electrical pathways (i.e., substrate modification) together with a trigger is required to initiate the arrhythmia (Shimizu and Centurion, 2002). Various clinical factors (e.g., aging, AF, heart disease, drugs, autonomic nerve system, etc.) change the electrophysiologic properties of the LA and consequently determine the progression, treatment, and termination of AF. In the following sections we will present an overview of implications and significance of AF, current management guidelines, followed by risk stratification in AF which is the topic of this study.



- 1. Roof
- 2. Posterior
- 3. Septum



- 4. Lateral wall
- 5. Inferior-posterior
- 6. Inferior-septum

**Figure 1.1 Left atrium wall regions**

**PV: pulmonary vein; LAA: left atrial appendage. Reprinted with permission from (Sanatkhani et al., 2018).**

## **1.2 Atrial Fibrillation, The Most Common Arrhythmia**

A disturbance in the autonomous nervous system and spontaneous pulmonary vein triggers can interfere with sinus rhythm and cause AF (Chen et al., 2014). These triggers are typically automatic foci of tachycardia type or multiple wavelets spreading through the LA. This arrhythmia causes the atrium to quiver at high frequency (approximately 400-600 beats per minute), instead of contracting in a synchronized manner. Loss of effective atrial contractile function and sinus rhythm contribute to reduction in cardiac output and subsequently result in flow stasis and

thrombus formation, which in-turn increase the risk of cardioembolic complications and stroke (Gloekler et al., 2017).

AF is the most common arrhythmia and is a major cause of mortality and morbidity. In the U.S., as the baby boomers are getting older and since AF is more prevalent in the aged, the number of strokes attributable to AF is expected to increase. Currently, AF is affecting three to six million US patients a year. This number is rapidly increasing, with 12.1 million AF patients expected by 2030 and 15.9 million by 2050 (Mozaffarian et al., 2016, Virani et al., 2020). Due to the significant complications associated with AF, including stroke, heart failure (HF), tachycardia, and myocardial infarction, AF has considerable economic implications. Currently, this disease costs ~\$6 Billion each year (Vainrib et al., 2017).

There are numerous underlying risk factors for developing AF, including but not limited to age  $\geq 60$  years, diabetes, HF, hypertension, coronary artery disease, thyroid disease, structural heart disease, prior open heart surgery, prior myocardial infarction, untreated atrial flutter, obstructive sleep apnea, excessive alcohol or stimulant use, chronic lung disease, and serious illness or infection (January et al., 2014).

According to various longitudinal studies, AF patients are clearly at an increased risk of morbidity and mortality. The most dangerous complication is thromboembolic stroke for which AF is an independent risk factor. AF patients have a 3-5 fold higher risk of stroke and it is estimated that about 15% to 20% of strokes in the US each year can be related to AF (Gloekler et al., 2017, Kamel et al., 2016).

Considering the significance AF, numerous studies have been carried out with the goal of improving the clinical management of AF and guidelines have been published regularly as a results of these studies (January et al., 2019).

### 1.3 Current AF Management Guidelines

AF is commonly classified based on its duration of onset and the ability to restore the normal sinus rhythm: 1) Paroxysmal, a self-terminating AF episode lasting less than 7 days, 2) Persistent, AF episode lasting longer than 7 days and less than a year, and 3) Permanent, when AF persists over a year. Management of AF including rate control (e.g., pharmacologic intervention, nonpharmacologic intervention) and rhythm control (e.g., antiarrhythmic therapy, ablation therapy) strategies are primarily guided based on patient's AF classification and clinical evaluation (Amin et al., 2016, Kakar et al., 2007).

Initially, the hemodynamic stability of each AF patient is evaluated. In case of hemodynamic stability, the management starts with a consideration of the symptomatology and its duration. On the other hand, if hemodynamic instability exists, patients are treated by restoring sinus rhythm and/or reducing ventricular rates. Sinus rhythm can be restored using direct current cardioversion (DCCV). Further, irrespective of hemodynamic status, anticoagulation therapy is initiated at this stage with respect to the patients ability and tolerance (Amin et al., 2016).

After the initial evaluation and treatment, the long-term management of AF focuses on managing patient's symptoms by rate and/or rhythm control strategies. Further, each patient is evaluated for thromboembolic risk and treated with anticoagulation accordingly to prevent ischemic stroke and other thromboembolic events (**Figure 1.2**). Further, surgical excision or stapling of LAA is performed in association with open heart surgery because most thrombi originate in LAA. More recently, there has been improvements in performing the LAA exclusion using minimally invasive procedures as an alternative to oral anticoagulation (**Section 1.3.4**). However, patients still might need antithrombotic therapy even after the exclusion of the LAA (Camm et al., 2012).

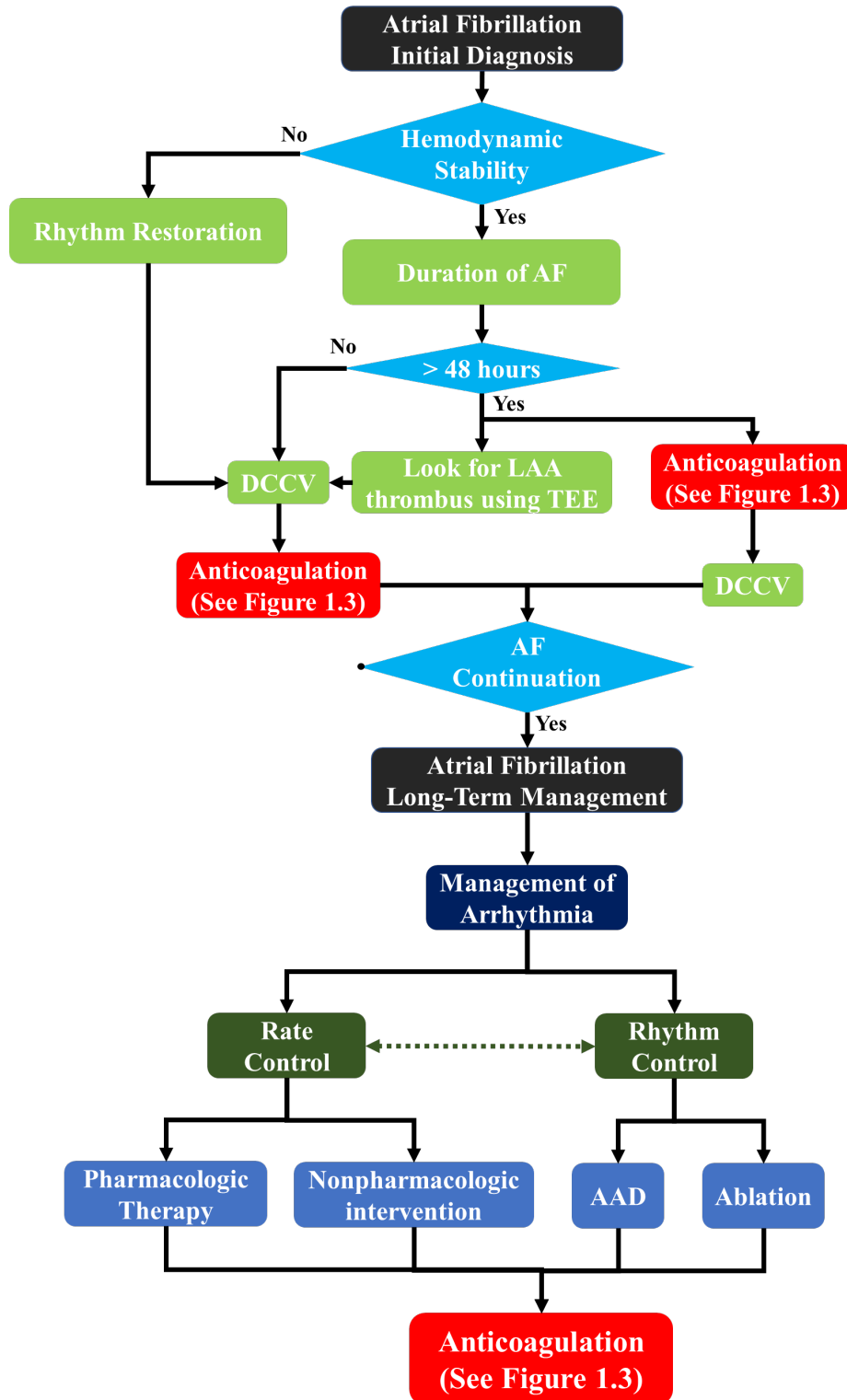


Figure 1.2 Simplified overall diagram of atrial fibrillation management

AF: atrial fibrillation; DCCV: direct current cardioversion; LAA: atrial fibrillation; TEE: transesophageal echocardiography; AAD: antiarrhythmic drug.

### **1.3.1 Rate Control**

Rate control can be achieved by either pharmacologic therapy (i.e., beta blockers such as metoprolol, propranolol, and esmolol or nondihydropyridine calcium channel blockers such as verapamil and diltiazem) or nonpharmacologic interventions (e.g., AV node and permanent pacemaker) based on patient's other conditions. The goal is to decrease the resting and exertion rate of the ventricle. In patients with permanent AF, chronic heart failure, and low left ventricular ejection fraction, biventricular pacemaker implantation post AV node ablation is recommended (Doshi et al., 2005).

### **1.3.2 Rhythm Control**

The goal of rhythm control is to maintain the sinus rhythm. Antiarrhythmic therapy is carried out based on the AF type and the antiarrhythmic drugs (AAD) side effect profile, and underlying heart disease and comorbidities (January et al., 2014).

#### **1.3.2.1 Ablation and Atrial Remodeling**

The triggers that lead to AF are not objective to characterize although a hypothesis have been described in regard to the role of disturbance to the autonomous nervous system (ANS) and activation of AF triggers (Chen et al., 2014). The extrinsic and intrinsic nervous systems both have roles in AF pathogenesis. The intrinsic cardiac ANS in consisted of large ganglionated plexi (GP). Ablation of GP can disconnect the intrinsic nervous system from extrinsic nervous system and mitigate the AF. However, autonomic remodeling in term of reinnervation and sprouting of nerves causes the return of fibrillation after an atrial effective refractory period (AERP).

Due to the low success rates of AADs and their potential long-term side effects, ablative therapy is considered as an alternative approach where PVs are isolated with radiofrequency ablation or balloon cryoablation. Ablation therapies have proven to be better than AADs in patients with paroxysmal or persistent AF, with ~70% of patients maintaining sinus rhythm during a 12 month period (Pappone et al., 2003). Due to the necessity of anticoagulation therapy after ablation, patients must have the tolerance for anticoagulation.

LA ablation has become a common AF treatment, however, pre-procedural substrate prediction is very important for patient selection (Calkins, 2012). Depending on the AF stage, some patients could undergo a simple ablation on the pulmonary veins ostium to eliminate the AF triggers (i.e., pulmonary vein isolation, PVI), whereas other patients may require more intricate modification of AF substrate in order to avoid recurrences. Further, many factors have been associated as predictors of success rate for ablation, including age, left atrial volume, BMI, sleep apnea, etc. (Abecasis et al., 2009, Berruezo et al., 2007, Jongnarangsin et al., 2008).

Despite substrate remodeling with ablative techniques, recurrence of AF is still possible. Thus, the prediction of AF recurrence is of great value to reduce the per- and post-procedure complications (e.g., phrenic nerves injuries which in critical cases can lead to hemi-paralysis (Goff et al., 2016)). Atrial remodeling via enlargement/ballooning due to existence of persistence AF has been accepted to be associated to the AF recurrence after PVI. All the patients in the cohort of this study have had ablation procedure.

### **1.3.3 Anticoagulation Therapy**

Every AF patient is initially evaluated for thromboembolic risk (**Section 1.4**), with a re-evaluation performed at each stage of management. A general decision-making flowchart for

anticoagulant therapy is illustrated in **Figure 1.3**. The existence of valvular or nonvalvular AF plays a vital role in choosing the type of anticoagulant. AF with moderate-to-severe mitral stenosis or artificial heart valves is generally referred to valvular AF. They usually require long-term oral anticoagulation with vitamin K antagonist. In case of nonvalvular AF and having low risk (CHA<sub>2</sub>DS<sub>2</sub>-VASc score = 0) with age < 65, or when there are contraindications to anticoagulation, no antithrombotic therapy is administered. Otherwise, depending on the risk of stroke assessed by the CHA<sub>2</sub>DS<sub>2</sub>-VASc score and risk of bleeding, assessed by HAS-BLED score and other individualized assessments, some type of anticoagulation therapy, depending on patient's tolerance and drug to drug compatibility, is needed (**Figure 1.3**).

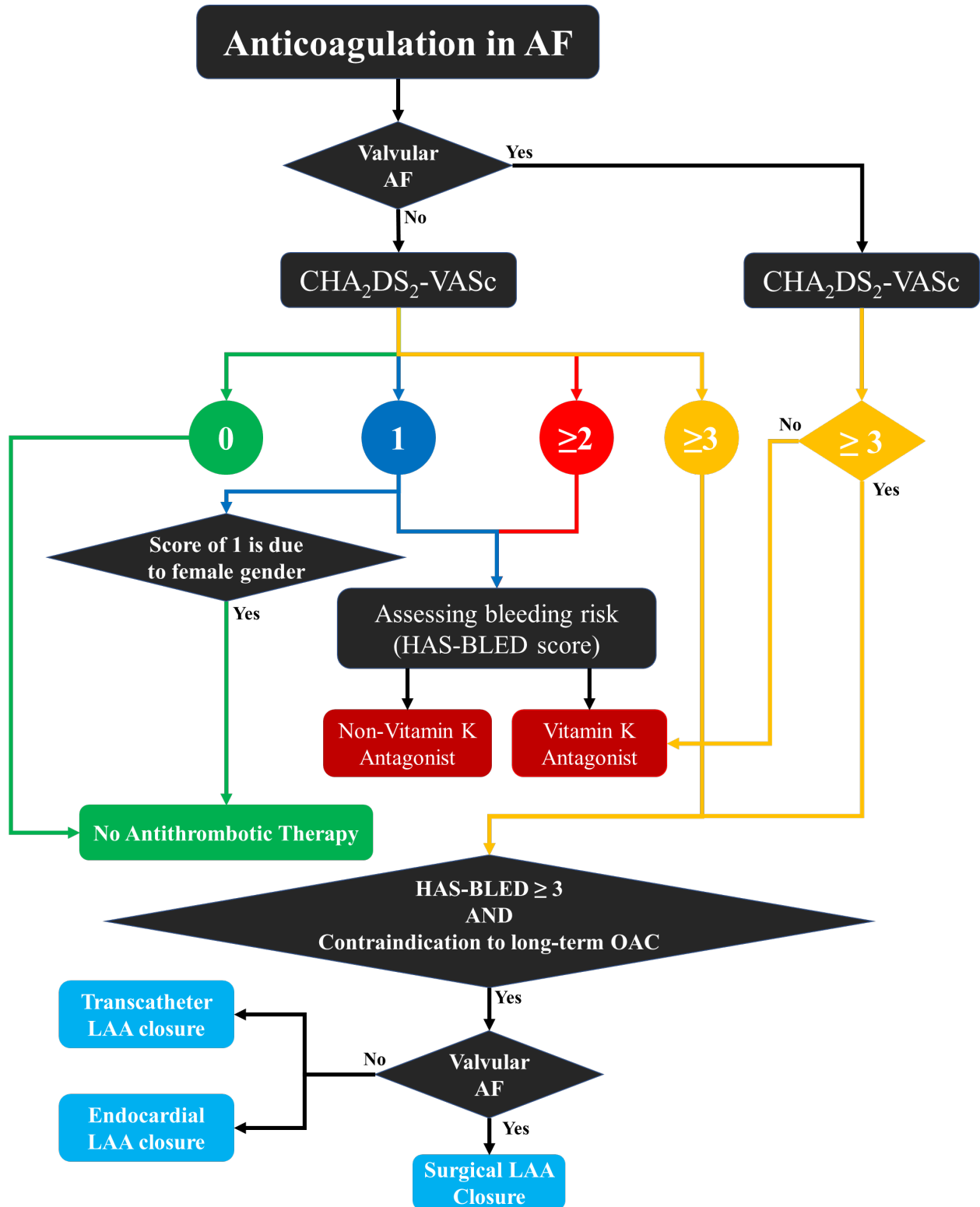


Figure 1.3 Simplified decision making flowchart for anticoagulation in atrial fibrillation

AF: atrial fibrillation; LAA: left atrial appendage.

### 1.3.4 Left Atrial Appendage Closure Devices

LAA is the prominent location for thrombus formation in AF (**Section 1.5**). Anticoagulation with vitamin K antagonist therapy is contraindicated in 14-44% of AF patients (Sakellaridis et al., 2014). These patients have a very narrow therapeutic window, require specific dietary restrictions, and potential for drug-drug interactions. Therefore, LAA closure is desirable in these cases. There are three approaches for excluding LAA: 1) surgical approach to amputate or ligate the LAA, 2) percutaneous endovascular approach to inset the occlusion device inside the LAA, and 3) percutaneous epicardial ligation to externally exclude the LAA.

Watchman device and Amplatzer cardiac plug are example of percutaneous left atrial appendage transcatheter occlusion devices that have shown encouraging results. Even though Current results show that LAA occlusion reduces long-term stroke risk, its efficacy and safety are controversial (Apostolakis et al., 2013). According to the guidelines, oral anticoagulation is still the preferred therapy in most cases for stroke prevention. However, patients with bleeding risk or poor drug tolerance or adherence who are poor candidates for long-term oral anticoagulation can be considered for Watchman device. These patients must be suitable for short-term warfarin administration and should have  $CHADS_2 \geq 2$  and  $CHA_2DS_2-VASc \geq 3$  (January et al., 2019) (**Figure 1.3**).

Anticoagulation therapy is one of the most important parts of clinical management in AF. Stroke risk stratification is essential when making decisions about anticoagulation therapy or LAA closure. Accurate stroke stratification is critical to improve the patient selection decision for LAA exclusion/occlusion and increase the effectiveness of anticoagulant management while lowering the side effects.

## 1.4 Current Clinical Risk Stratification Schemes

Most stroke and thromboembolism (TE) risk predictions for AF patients are based on clinical risk stratification schemes like Framingham, NICE, CHADS<sub>2</sub>, and CHA<sub>2</sub>DS<sub>2</sub>-VASc, which have been developed on the basis of risk factors identified from trial cohorts (January et al., 2014). Efforts have been made to improve the risk stratification for thromboprophylaxis to find the higher risk patients more effectively (Kakar et al., 2007). However, many inconsistencies have been reported among the risk stratification schemes (Lip and Boos, 2008). The most commonly used and validated risk stratification scheme for making clinical decisions regarding the anticoagulant or antiplatelet therapy for the management of AF patients are CHADS<sub>2</sub> and newer CHA<sub>2</sub>DS<sub>2</sub>-VASc schemes. Everyone has a score with range of 0 to 6 and 0 to 9 based on CHADS<sub>2</sub> and CHA<sub>2</sub>DS<sub>2</sub>-VASc schemes, respectively. The scoring strategies for CHADS<sub>2</sub> and CHA<sub>2</sub>DS<sub>2</sub>-VASc schemes are shown in **Table 1.1**. According to the CHADS<sub>2</sub> scheme, score of 0 is considered minimal risk, score of 1 or 2 is moderate, and score of  $\geq 3$  are high risk. Similarly, according to the CHA<sub>2</sub>DS<sub>2</sub>-VASc scheme, a score of 0 is considered insignificant risk, a score of 1 is considered moderate, and  $\geq 2$  is considered elevated risk. Because of the added risk factors compared to the CHADS<sub>2</sub> scheme, CHA<sub>2</sub>DS<sub>2</sub>-VASc scheme has a better ability to identify low risk patients. Further, it has the tendency to classify more patients into the higher risk group rather than moderate risk group (Chen et al., 2013). It is recommended that patients who receive score of  $\geq 2$  from either scheme to be treated with anticoagulation therapy. These guidelines are constantly changing to improve their accuracy, however, even more refined versions of these schemes (January et al., 2019, Lip et al., 2010) do not determine stroke risk based on the patient-specific hemodynamics and physics. Presently, we stay very limited in predicting who will have a stroke in the context of AF.

**Table 1.1 Scoring strategies for CHADS<sub>2</sub> and CHA<sub>2</sub>DS<sub>2</sub>-VASc schemes**

<b>CHADS<sub>2</sub> Scheme (0-6)</b>		<b>CHA<sub>2</sub>DS<sub>2</sub>-VASc Scheme (0-9)</b>	
<b>Risk Factor</b>	<b>Score</b>	<b>Risk Factor</b>	<b>Score</b>
History of Stroke/ Transient Ischemic Attack	2	History of Stroke/ Transient Ischemic Attack	2
Age > 75 years	1	Age (years): > 75 <b>or</b> > 65 and < 75	2 <b>or</b> 1
Hypertension	1	Hypertension	1
Diabetes Mellitus	1	Diabetes Mellitus	1
Heart Failure	1	Heart Failure	1
		Vascular Disease	1
		Female Gender	1

### **1.5 LAA: The Most Prominent Region for Thrombus Formation in AF**

LAA, due to its complex morphology as compared to the smooth-walled LA, is a favored location for thrombi formation: 91% and 50% of thrombi in nonvalvular AF and valvular AF, respectively, are found in LAA (Al-Saady et al., 1999, Holmes et al., 2009, Reddy et al., 2013). These thrombi are known to cause stroke in AF patients. As explained in **Sections 1.3 and 1.4**, cardioversion, antiarrhythmic drug therapy, or ablation therapy are used to restore the normal sinus rhythm. In addition, to prevent stroke in AF patients, anticoagulation management is required. A major limitation to using anticoagulation is the risk of bleeding which is estimated to ~1.4-3% per year when all AF patients are considered (Camm et al., 2010, Hughes et al., 2007, Vainrib et al., 2017). CHA<sub>2</sub>DS<sub>2</sub>-VASc score is the most used index for making clinical decisions regarding the management of AF patients. While this index is based on clinical data (**Table 1.1**), it does not incorporate the role of LA–LAA geometry or local hemodynamics in the thromboembolic risk assessment. Because of the concern for bleeding, about 30-40% of AF patients who are eligible for anticoagulation based on the CHA<sub>2</sub>DS<sub>2</sub>-VASc score are not on any anticoagulation agents.

Recent technologies aiming at LAA occlusion/exclusion are being developed to mitigate this problem and exclude the critical origin of thrombus (**Section 1.3.4**). There is always a tradeoff between the risk of bleeding and the risk of stroke but the decision to anticoagulation or not is currently not informed by the morphology of patient-specific LAA/LA.

### **1.6 Correlation of LAA Appearance/Shape with Stroke Risk**

LAA is a complex structure which arises from the anterolateral of LA. It typically starts with an ovoid orifice and reaches the apex via the neck, and it may contain multiple lobes. LAA is the most prominent region for thrombus formation in AF patients (Al-Saady et al., 1999). The hypothesis that there is a correlation between the LAA morphology and stroke risk has been assessed in several studies. Many indices have been examined in this context: LAA orifice diameter; number of branches and twigs; degree of coverage with fine structures (Ernst et al., 1995); LAA volume, depth, and number of lobes (Beinart et al., 2011); LAA takeoff from mitral valve (Nedios et al., 2014); and existence of a bend in LAA with an acute angle (Yaghi et al., 2020). Di Biase et al. (2012) categorized LAA shapes into four groups: chicken wing, windsock, cactus, and cauliflower shapes (**Figure 1.4**). This classification is solely based on the visualization of LAA morphology: shape, geometrical features such as the existence of obvious bend, length, number of lobes, etc. (Beigel et al., 2014, Wang et al., 2010). Di Biase et al. (2012) concluded that patients with the ChickenWing morphology are less likely to have a stroke while Cauliflower morphology is associated with more stroke. Although these results are promising, there is a large variability in stroke occurrence within a given LAA shape category (Khurram et al., 2013, Nedios et al., 2014, Sanatkhani and Menon, 2017, Sanatkhani et al., 2021, Yaghi et al., 2018). The

subjective nature of LAA shape categorization may contribute to this variability. In this study, we will show an objective index to quantify LAA morphology using the principal component analysis (Sanatkhani and Menon, 2018). This approach uses the entire three-dimensional cardiac computed tomography (CCT) image, as opposed to isolated measurements of LAA dimensions, and therefore is more objective and comprehensive in quantifying LAA appearance. We are proposing a methodology that will quantify the complexity of LAA.

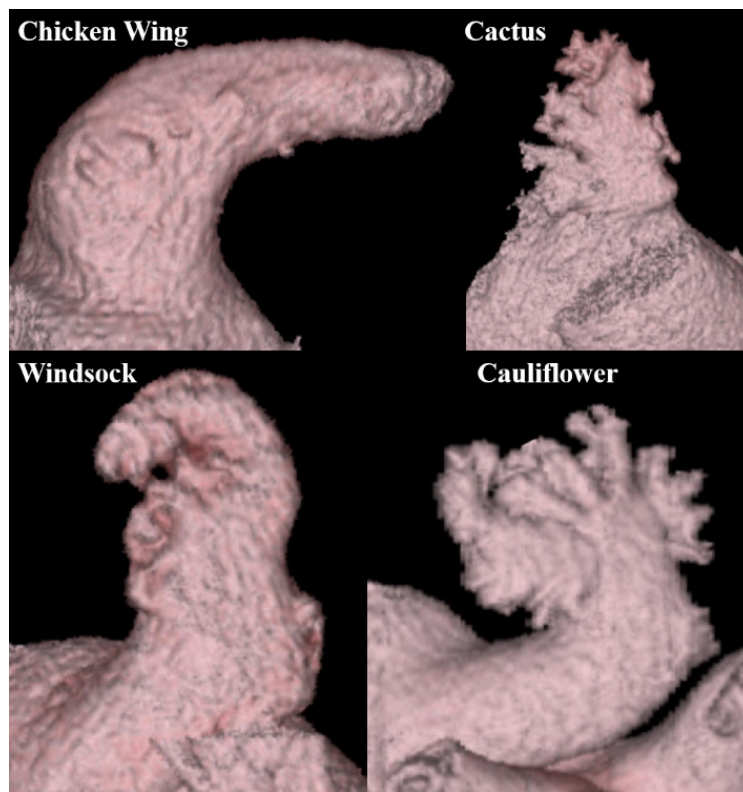


Figure 1.4 Clinically identified left atrial appendage shape categories

**ChickenWing**: This is the most common shape (48%), with a dominant lobe and an obvious bend in its proximal or middle part that folds back on itself. It also may have secondary lobes. **Cactus**: This is the second most common shape (30%), with one dominant central lobe and secondary lobes arising from the dominant lobe superiorly and inferiorly. **Windsock**: With an occurrence frequency of 19%, the primary structure here is a dominant lobe and secondary or tertiary lobes may exist at different locations. **Cauliflower**: It is the least common shape (3%), without a dominant lobe and having complex twigs (i.e., small and short-length lobes).

Reprinted with permission from (Di Biase et al., 2012).

## 1.7 Correlation of LAA Hemodynamics with Stroke Risk

In the presence of atrial fibrillation (AF), the loss of effective atrial contractile function and sinus rhythm contribute to reduction in cardiac output and results in flow stasis and thrombus formation, which in-turn increases the risk of cardioembolic complications and stroke. Several surrogates of thrombus-promoting flow patterns have been used to relate blood flow in vascular structures (including LA and LAA) to probability of clot formation: wall shear stress, shear strain rate, time-averaged wall shear stress, oscillatory shear index (Koizumi et al., 2015), time-averaged velocity, mean resident time (Rayz et al., 2010), local residence (Esmaily-Moghadam et al., 2013), residual virtual contrast agent (Bosi et al., 2018, Otani et al., 2016), and vortex structure (Masci et al., 2019, Masci et al., 2020). The most realistic solution to simulate clot formation is to model the transport of blood cells (i.e., platelets, red blood cells, etc.) in each geometry. A Lagrangian approach can be used for this purpose (Bernsdorf et al., 2006), which requires tracking of a large number of particles and a very fine mesh to resolve the flow field for particle tracking, making it computationally very expensive (Rayz et al., 2010). An Eulerian approach, where tracer concentration transport approximates the Lagrangian particle transport, has been used with reasonable success for quantifying indices correlated with thrombus formation (Bosi et al., 2018, Esmaily-Moghadam et al., 2013, Masci et al., 2020, Otani et al., 2016, Rayz et al., 2010, Sanatkhani et al., 2018, Sanatkhani et al., 2021). However, an index to quantify the stroke risk based on LA/LAA hemodynamics is still needed. In the next section we present the theory behind our systems-based approach to quantify patient-specific LA/LAA hemodynamics and consequently, indices that are likely to be related to the thrombus formation risk.

## 1.7.1 Systems-Based Approach to Quantify Patient-Specific Indices of Thrombosis

### Formation Risk

We treat LA/LAA as a system to quantify the relevant hemodynamics and consequently, the patient-specific indices of thrombosis risk. For the hemodynamic characterization, LA/LAA in patients with AF is assumed to be a nonlinear, time-invariant system whose hemodynamic behavior is mathematically modeled using the well-established fluid dynamics and material transport principles (details in **Section 3.1**). The system properties (parameters) are comprised of the patient-specific attributes: LA/LAA geometry, hematocrit, pulmonary vein input (cardiac output), heart rate, etc.). As illustrated in **Figure 1.5**, an injection of a tracer in LAA corresponds to the **input** of the system and we wish to observe how this tracer is cleared from LAA. The tracer clearance is quantified in terms of the **output** of the system (**Figure 1.5**): residence time distribution function,  $E(t)$ . Physically,  $E(t)\Delta t$  represents the fraction of tracer exiting the LAA that has spent between time  $t$  and  $t+\Delta t$  inside the LAA. Two indices of tracer clearance are calculated from  $E(t)$ : mean residence time of the tracer in the LAA (first moment of  $E(t)$ ) and asymptotic tracer concentration remaining in the LAA. These two indices are expected to be positively correlated with the risk of thrombus formation. Details regarding  $E(t)$  and subsequently calculated indices using  $E(t)$  are presented in **Section 3.1.9**. According to the systems-based approach, the observed output of the system for an impulse input (i.e., impulse response of the system) is exclusively dependent of the system properties (parameters). Therefore, we inject tracer material into the LAA instantaneously such that the LAA concentration of the tracer is 1 at  $t = 0$  and observe the output,  $E(t)$ , to learn about the tracer clearance dynamics of our system and consequently, calculate tracer clearance indices that are expected to be correlated with thrombus formation.

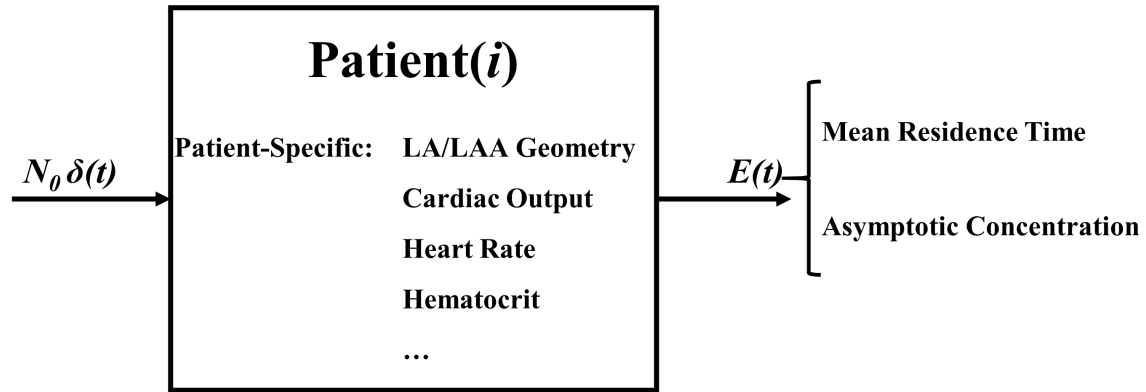


**Figure 1.5** Systemes-based approach to quantify patient-specific indices of thrombus formation risk  
**System:** left atrium/left atrial appendage (LA/LAA) with patient-specific system properties (i.e., patient-specific LA/LAA geometry, cardiac output, and hematocrit); **Input,**  $N_0 \delta(t)$ : Impulse injection of the tracer material inside the LAA, with  $N_0$  being the total amount of injected tracer that results in LAA tracer concentration of 1 at  $t = 0$  and  $\delta(t)$  is the dirac delta; **Output:** patient-specific residence time distribution function,  $E(t)$ , and associated calculated indices (i.e., mean residence time of the tracer in the LAA and asymptotic tracer concentration remaining in the LAA).

## 1.8 Objective and Specific Aims

Current methodologies for shape quantification are subjective and they do not fully characterize LAA shape complexities. Calculated particle residence time using the analysis of LA/LAA hemodynamics, may correlate with stroke risk in AF patients; but this has not been investigated systematically. **The objective of the present study was to determine whether LAA residence time and LAA appearance indices are able to independently improve stroke stratification in AF patients and consequently enhance clinical decision making.** There are three aims to address the stated objective.

### **1.8.1 Specific Aim 1: Develop a Quantitative Index of LAA Appearance**

The goal here was to develop a new quantitative index of the complexity of LAA appearance (shape) directly from measured image data, without using any *a priori* geometric models. This index is based on the Principal Component Analysis (PCA) of the entire three-dimensional image of the LAA. It is expected that this quantitative index will characterize the complex LAA appearance in a comprehensive manner and enhance the current approach for stroke risk stratification and clinical management in AF patients.

### **1.8.2 Specific Aim 2: Develop a Quantitative Index of LAA Residence Time Using a Systems Approach**

The goal here was to develop a computational-fluid dynamics (CFD)-based approach to calculate LAA residence time and associated indices in a patient-specific manner and examine the effects of confounding variables such as the pulsatility of pulmonary vein waveform, non-Newtonian blood properties, and hematocrit levels to optimize the computational protocol.

### **1.8.3 Specific Aim 3: Develop a Predictive Model to Stratify Stroke Risk Using LAA Appearance and LAA Residence Time Indices**

The goal here was to examine whether indices calculated in Specific Aims 1 and 2 (i.e., LAA appearance index and LAA mean residence time and associated indices) have the ability to predict stroke in AF patients. Multiple logistic regression is used to predict stroke. This effort is

expected to improve significantly stroke risk prediction in AF patients and consequently, enhance the decisions made about thromboprophylaxis.

## **1.9 Organization of Dissertation**

Methods and the workflow used to quantify the LAA appearance objectively are presented in Chapter 2.0. The calculated index (i.e., LAA appearance complexity index) is assessed by examining sample subjects. Further, the correlations of LAA appearance complexity index and the traditional LAA shape classification and CHA<sub>2</sub>DS<sub>2</sub>-VASc score are examined in this chapter.

The CFD-based methodology for calculating the proposed hemodynamic index (i.e., mean residence time) in a patient-specific manner is presented in Chapter 3.0. In addition, the effects of confounding physiological variables (patient-specific pulmonary vein waveform, non-Newtonian blood properties, and hematocrit levels) and the length the CFD simulation on mean residence time are examined. Finally, the correlation between the LAA mean residence time and LAA appearance complexity index (*LAA-ACI*) and between the LAA mean residence time and CHA<sub>2</sub>DS<sub>2</sub>-VASc score are examined.

The results regarding whether the LAA appearance and residence time indices enhance the current approach for stroke risk stratification in AF patients are presented in In Chapter 4.0.

An overall summary of our work and suggestions for the future directions are presented in Chapter 5.0.

Supplementary details of our methodologies, such as the detailed workflow of preparing LAA images to calculate the appearance complexity index, implementation of custom CFD solver

in C++ into the OpenFOAM software, and the analytical tools used for calculating the mean residence time, are presented in the appendices.

## 2.0 Specific Aim 1: Develop a Quantitative Index of LAA Appearance

As discussed in **Section 1.5**, LAA has more complex morphology as compared to the rest of the LA, and this is a favored location for thrombus formation. The complex LAA morphology can result in complex flow patterns within LAA, including recirculating zones and blood stasis, which increase the risk of thrombus formation. It is surprising to note that the current clinically used stroke risk stratification metric in AF patients, CHA<sub>2</sub>DS<sub>2</sub>-VASc score, does not take into account LAA morphological features of LAA. Therefore, it is reasonable to expect that the quantification of LAA morphological features (appearance) and establishing its utility in stroke risk stratification can improve the AF management, which in-turn can reduce the likelihood of future complications.

The currently available characterization of LAA appearance is very limited owing to the qualitative nature of the appearance classification paradigm. This approach is problematic not only because of the subjectivity of human interpretation but also the inadequacies of the descriptors of the geometric features used as the basis for the classification (Khurram et al., 2013). Further, experienced electrophysiologists don't always agree; a given LAA is often classified in different shape-based groups, marked with a different risk score, and treated in a different way depending on the reader's subjective interpretation of the images. The quantitative characterization of LAA appearance using patient-specific clinical images of the left atrium and an algorithmic approach is highly desirable and such a quantitative characterization is expected to improve stroke risk stratification.

## 2.1 Methodology

### 2.1.1 Study Subject Characteristics

A total of 128 subjects with symptomatic AF (111 paroxysmal, 17 persistent) were studied (11 males). All patients included in this study were undergoing evaluation and treatment of AF, including medical management and procedural based treatments. Children were excluded from this study. Cardiac-computed tomography (CCT) was performed in subjects prior to an AF catheter ablation procedure at University of Pittsburgh Medical Center (UPMC, Pittsburgh, PA, USA). CCT images were obtained using a multidetector 64-row helical system (Brilliance 64, Philips, Netherlands). Scanning was performed gated to the cardiac cycle in cranio-caudal direction from the aortic arch towards the diaphragm. The imaging parameters were: 70–120 kV, 850 mA s, 0.6 mm beam collimation, 0.625–1.25 mm thickness, and 20–30 cm field-of-view. During an end-inspiratory breath-hold of 20 s and following a timing bolus-chase injection (20 ml at 5 ml s<sup>-1</sup>), 90 ml of an iodinated contrast medium (Ultravist 370, Bayer Vital, Cologne, Germany) was administered. The average age, heart rate, and cardiac output were  $63.6 \pm 9.0$  years (range: 35–79 years), 66 bpm (range: 40–132 bpm), and 4.0 L min<sup>-1</sup> (range 1.5–8.7 L min<sup>-1</sup>), respectively. The range of CHA<sub>2</sub>DS<sub>2</sub>-VASc scores was 0 to 5 (mean =  $2.0 \pm 1.1$ ).

### 2.1.2 Image Segmentation and Feature Vector Preparation

Contrast-enhanced CCT DICOM (Digital Imaging and Communications in Medicine) images were cropped and then smoothed using a median filter with a kernel of  $5 \times 5 \times 5$  to remove the high frequency noise in the image. Next, using the marching cubes method a surface body was

created in ParaView (version 5.9.1, Kitware, Inc., Albuquerque, NM, USA) representing the LAA surface. Unwanted surfaces attached to the LAA were manually removed in Geomagic Studio (version 10, Geomagic, Inc., Research Triangle Park, NC, USA). The remaining surfaces were smoothed out in Geomagic Studio. Next, a voxelization filter was used to generate a volume body out of the cleaned-up LAA surfaces, in ParaView. This generated volume body was used as a binary mask to segment just the LAA from the original CCT image in MATLAB® (version R2020b, MathWorks, Inc., Natick, MA) (**Figure 2.1**). Finally, all volume images were reoriented in a similar manner in which the ostium sit on the x-y plane with the surface normal points to +z axis. In case the LAA was bent (which almost always at least a slight bend exists), then the centerline pointed towards +x axis (i.e., the centerline vector was rotated until it had no y component). Next, every LAA was cropped using a cube as tight as possible with the LAA position at the center. Finally, LAA images were resampled into a 100×100×100 grid. A detailed flowchart of LAA segmentation is presented in **Figure 2.1**.

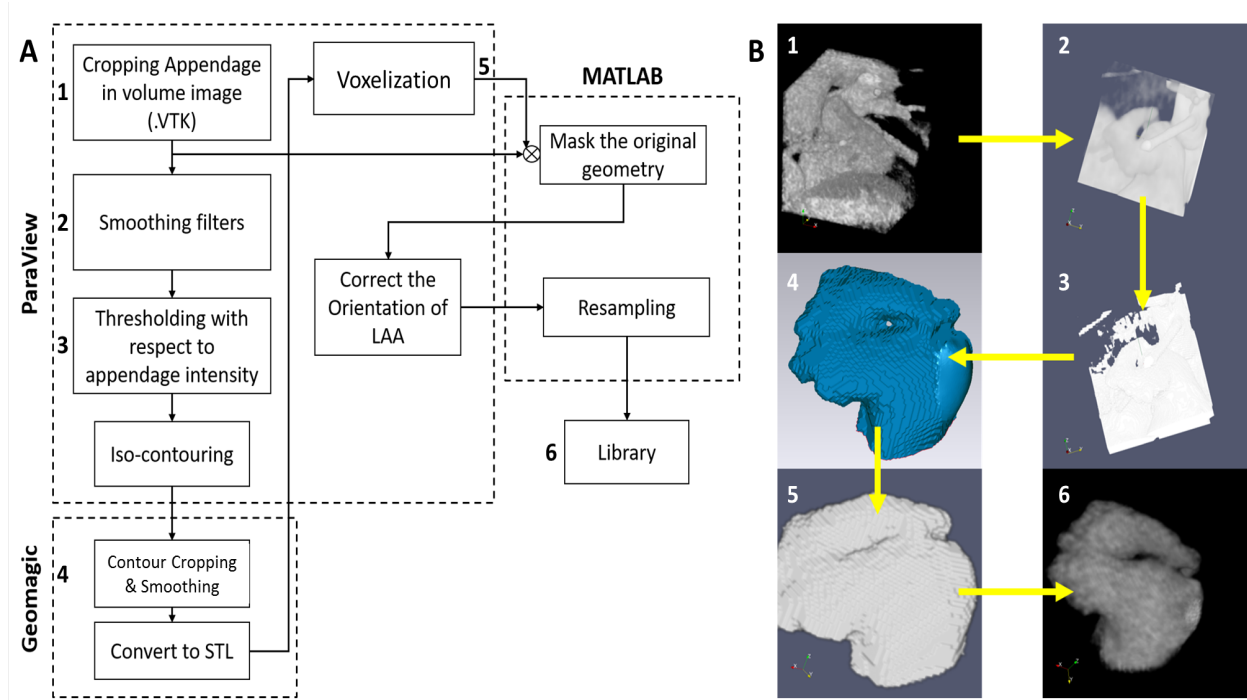


**Figure 2.1** Flowchart for the left atrial appendage extraction process

**A) Flowchart of the procedure employed to extract each patient’s left atrial appendage and prepared it for statistical analysis. The numbers alongside boxes are illustrated in section (B) of the figure, to visualize an example of each major step. VTK: Visualization Toolkit; LAA: left atrial appendage; STL: stereolithography. Adopted with permission from (Sanatkhani and Menon, 2018).**

### 2.1.3 Principal Component Analysis (PCA)

PCA is a method for simplifying a multidimensional dataset to lower dimensions for analysis, visualization, or data compression. In PCA we look for a set of linear, orthogonal projections of the data for which the variance in the corresponding direction (i.e., eigen vectors) is maximized. To parametrize LAA volume regions based on principal components (i.e., PCs or eigen mode) of greyscale appearance, each LAA image (100×100×100) was reshaped into a long vector ( $X_i$ ) with length of  $10^6$  samples, making each patient-specific LAA in the analysis a column

with  $10^6$  intensity observations in the cohort data matrix  $\mathbf{X} = (\mathbf{X}_1, \dots, \mathbf{X}_{128})^T$ . The average intensity vector  $\boldsymbol{\mu}$  was subtracted from each column of population matrix before generating the (128×128) covariance matrix ( $\boldsymbol{\Sigma}_{XX}$ ). Next, we computed the projections of the individual intensity vectors,  $\xi_j$  on the PCs viz. the eigen vectors of covariance matrix of  $\mathbf{X}$  (**Eq. 2.1**). The PCs were arranged in decreasing order according to the associated eigen values. By sorting the eigen vectors in this manner, the first PC corresponds to a component that explains the variation in the intensity data the most. Finally, by reshaping each PC vector ( $\boldsymbol{\xi}$ ) back into a 3D matrix we can generate the 128 eigen-shapes representing the principal modes of intensity variation in the study cohort:

$$\boldsymbol{\xi}_j = \mathbf{b}_j^T \mathbf{X} = b_{j1} \mathbf{X}_1 + \dots + b_{j128} \mathbf{X}_{128} \quad \text{Eq. 2.1}$$

To reconstruct the original LAA images,  $\mathbf{X}_i$ , the inner product of weights,  $\mathbf{b}_j$ , and the transposed matrix of sorted eigen vectors,  $\boldsymbol{\xi}$ , was computed (Izenman, 2008).<sup>1</sup>

#### 2.1.4 LAA Appearance Complexity Index (LAA-ACI)

We reconstructed each patient-specific LAA using a successively increasing number of PCs and calculated a normalized residual error in appearance reconstruction for each step,  $RE(i)$ , as follows (**Eq. 2.2**):

$$RE(i) = \sqrt{\frac{RSS(i)}{TSS}} \quad \text{Eq. 2.2}$$

where  $RSS(i)$  is the residual sum of squares for the  $i$ th step (i.e.,  $i$  PCs used in the reconstruction), and  $TSS$  is the total sum of squares.  $RE(i)$  decreases with increasing  $i$  because the more PCs we use to reconstruct an image, the more information is available to describe the details of the original

---

<sup>1</sup> In this chapter, vectors are shown in bold and italics and matrices in bold fonts. Other variables are shown in italics.

image. Using all PCs would result in the original LAA image with zero residual error [ $RE(128) = 0$ ]. We have defined the normalized area under the curve (AUC) of  $RE(i)$  vs.  $i$  (i.e.,  $\frac{1}{N} AUC(RE(i))$ , where  $N$  is the total number of patients in the cohort) as the LAA- $ACI$ ; a larger area under the curve would correspond to a more complex appearance (e.g., **Figure 2.2A**).

### 2.1.5 Statistical Analysis

Continuous variables are expressed as mean  $\pm$  standard deviation. Correlations between variables were determined by Spearman rank correlation. All statistical analyses were performed in SAS software (version 9.4, SAS Institute, Inc., NC, USA).

## 2.2 Results

### 2.2.1 Proof of Concept

In a subcohort of 16 patients, the LAA appearance was quantified using the PCA, generating 16 eigen-shapes of appearance variation (**Figure 2.2**). The zero<sup>th</sup> eigen-mode (i.e., first PC) of LAA appearance which explains the highest variances in LAA appearance in the study cohort had a strong resemblance to the ChickenWing LAA shape, which is known to have the lowest stroke risk (**Figure 2.2**). Further, the ChickenWing shape again was found to appear when we subtracted two standard deviations of the weight of the first eigen-mode (i.e., second PC) from the cohort average LAA appearance.

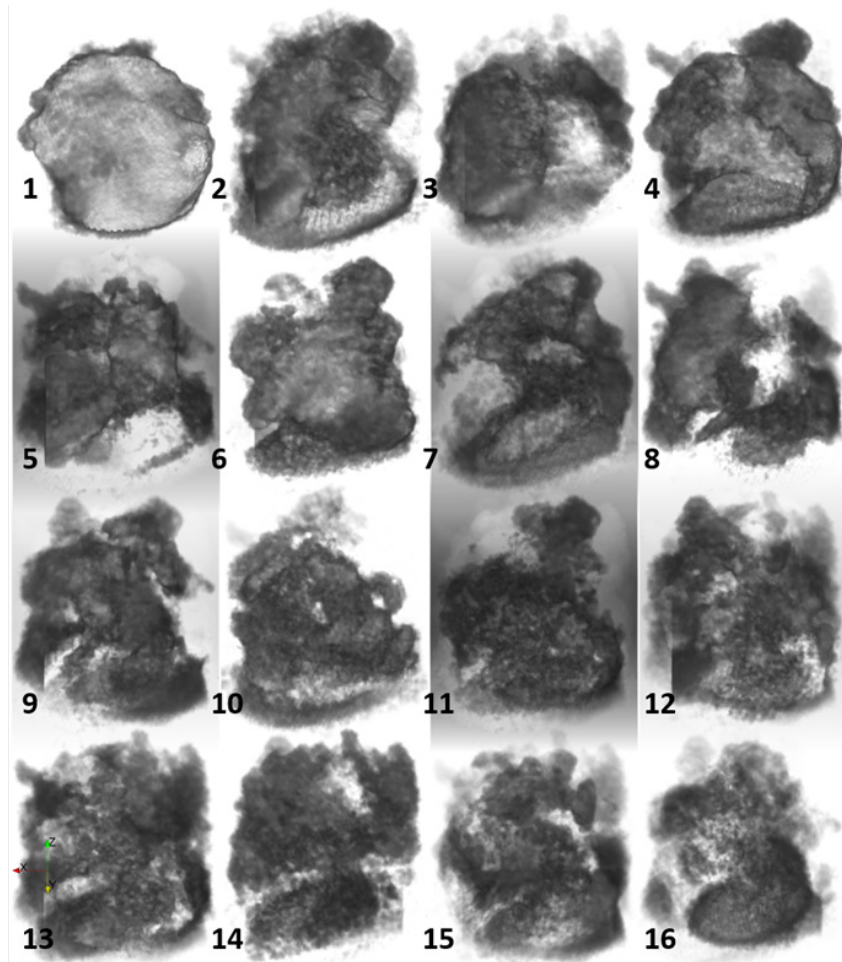


**Figure 2.2 Visualization of 16 eigen-shapes created in the principal component analysis**

**Reprinted with permission from (Sanatkhani and Menon, 2018).**

The ChickenWing and Windsock appendages were found to be distinguishable in terms of appearance reconstructions based up to 6 PCs, the Cactus shaped LAA reconstructed using up to 6 most dominant PCs was found to bear a strong resemblance to the ChickenWing (**Figure 2.3**).

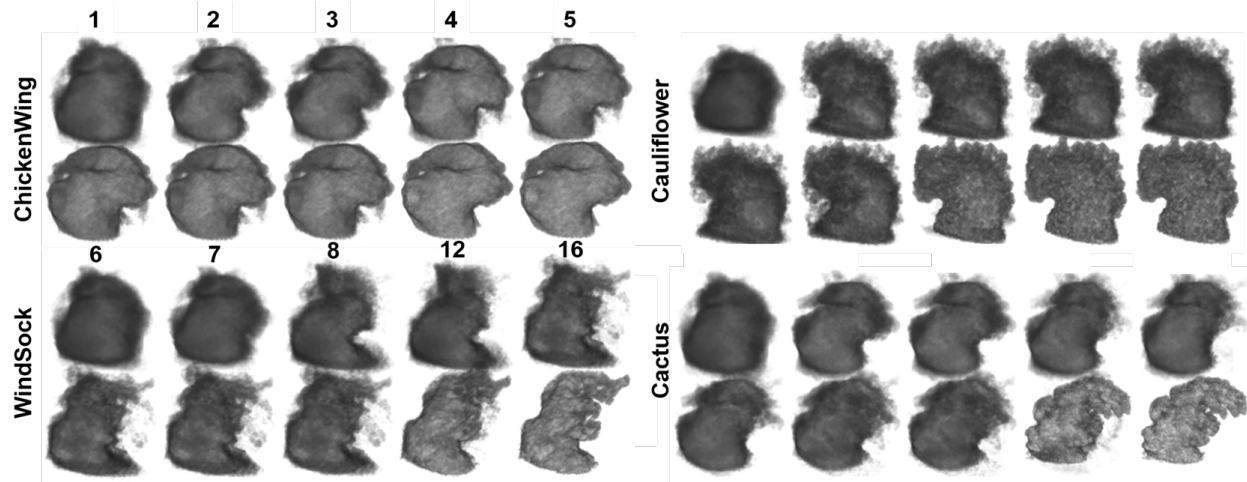


**Figure 2.3 Reconstructed left atrial appendages using different number of principal components**

The reconstructed image of all four categories using just one principal component (PC) look the same and resemble a ChickenWing appendage. This resemblance continues even when using two or more PCs in the Windsock and Cactus category, whereas in the Cauliflower case we see a more rapid evolution of appearance away from the ChickenWing shape after using two PCs. Reprinted with permission from (Sanatkhani and Menon, 2018).

Next, we chose two sample LAAs, 1) low risk and 2) high risk, based on the traditional classification (Di Biase et al., 2012). We reconstructed each LAA image using successively increasing number of PCs up to the point where the reconstructed LAA image was easily distinguishable. We were able to recognize the low risk LAA image with only using 4 PCs, while we used 12 PCs to reconstruct a recognizable image of the high risk LAA sample (**Figure 2.4**).

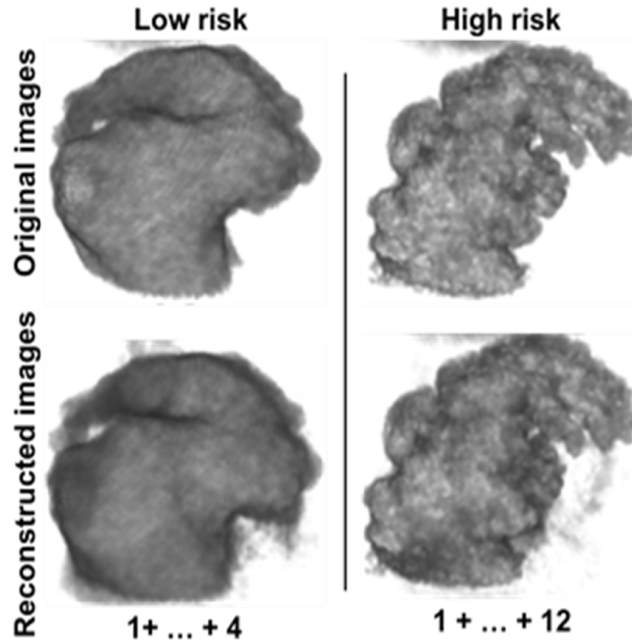
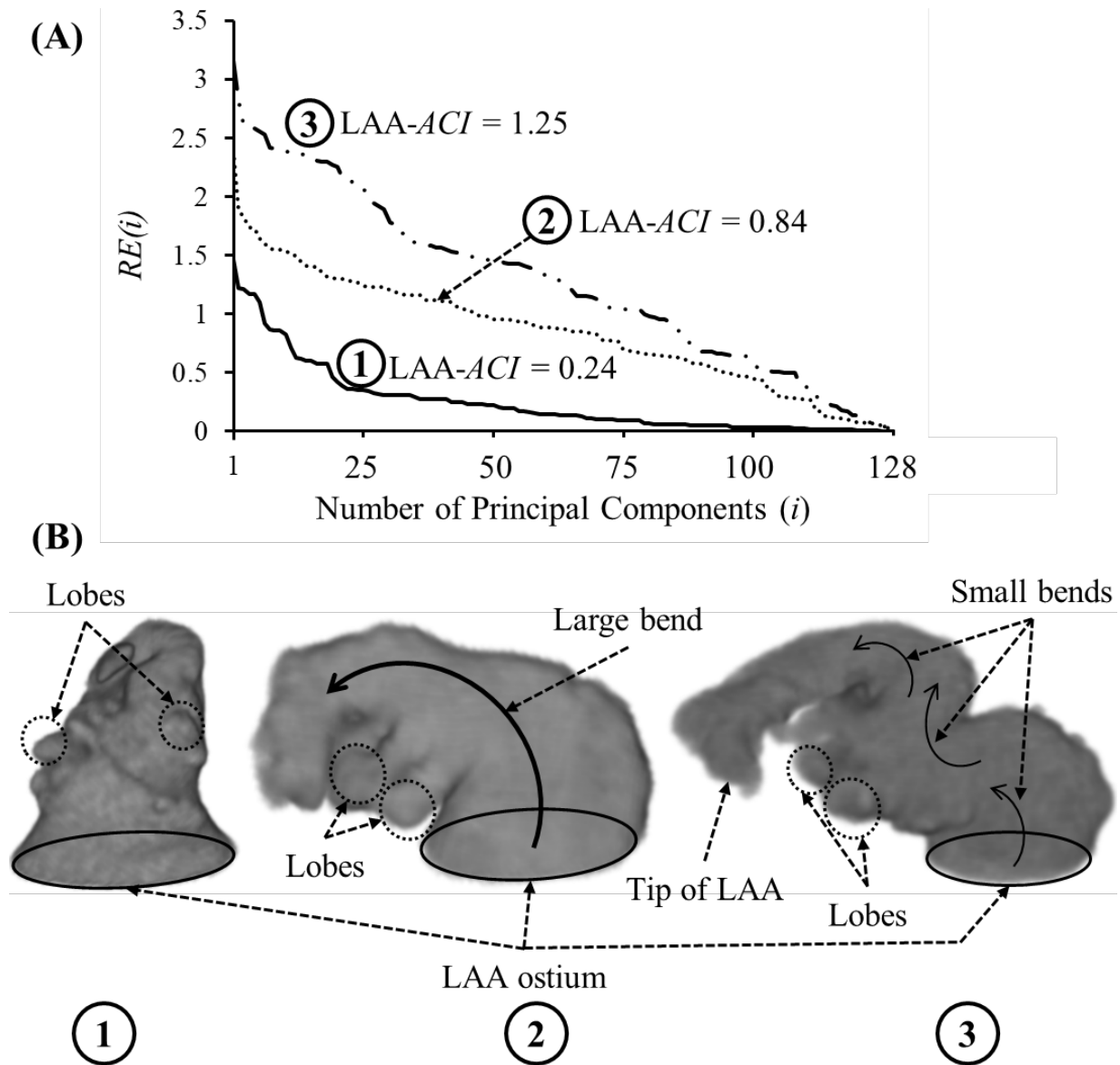


Figure 2.4 Visualization of reconstruction two left atrial appendage images using different number of principal components

The left atrial appendage (LAA) on the left with lower stroke risk requires only 4 principal components (PCs) while the higher stroke risk LAA on the right requires 12 PCs.

## 2.2.2 Quantitative Characterization

The residual error for step  $i$ ,  $RE(i)$ , vs.  $i$  curves for three representative subjects is shown in **Figure 2.5A**, along with the corresponding geometry of the three LAAs (**Figure 2.5B**). Subject #3 requires significantly more PCs for accurate reconstruction and, therefore, has the largest LAA- $ACI$  (i.e., area under the curve), indicating that this is the most complex appearance. The rank ordering based on the LAA- $ACI$  is subject #3, subject #2, and subject #1.



**Figure 2.5 Left atrial appendage appearance complexity index of three sample subjects**

**(A)** Normalized residual error,  $RE(i)$ , plotted as a function of the number of principal components ( $i$ ) used to reconstruct the left atrial appendage (LAA) appearance for three subjects. As  $i$  increases,  $RE(i)$  decreases, reaching a value of zero when  $i = 128$ , corresponding to a perfect reconstruction. LAA appearance complexity index ( $LAA-ACI$ ) is defined as the area under the  $RE(i)-i$  curve; larger  $LAA-ACI$  corresponds to a more complex LAA appearance. **(B)** Geometrical features of these three LAAs, including LAA ostium, tip of the LAA, LAA lobes (shown by circles), and LAA centerline bend (shown by curved arrows). The rank ordering of these three LAAs based on the  $LAA-ACI$  (simplest to most complex) is subject #1, subject #2, and subject #3.

### 2.2.3 Minimum Number of Subjects for Principal Component Analysis

The proposed methodology for computing *LAA-ACI* for a given subject requires the principal component analysis (PCA) of a cohort of AF subjects. We wanted to examine how the number of subjects in the cohort used for the PCA affects the calculated values of *LAA-ACI* and their rank ordering with respect to the complexity of LAA appearance. We randomly selected 25 out of 128 subjects as the reference test group. We then performed the PCA using this reference test group and calculated the *LAA-ACI* value for each of the 25 subjects in this reference test group. Next, we performed four additional PCAs using 50, 75, 100, and 128 subjects, each time including the 25 subjects from the reference test group and calculating the *LAA-ACI* value for each of the 25 subjects from the reference test group. Thus, we had 5 sets of *LAA-ACI* values for the 25 subjects from the reference test group corresponding to the varying number of subjects used in the PCA (25, 50, 75, 100, and 128). The average value of *LAA-ACI* for the reference test group was not affected by the number of subjects used in the PCA, especially above 75 (**Figure 2.6**). The Spearman rank order correlation analysis was performed between each of the 5 sets of *LAA-ACI* values and *LAA-ACI* values for the set with 128 subjects in the PCA. As illustrated in **Figure 2.6**, the Spearman rank order correlation coefficient is  $> 0.99$  for the number of subjects in the PCA above 75 (Note: By definition, the Spearman rank order correlation coefficient for 128 subjects in the principal component analysis is equal to 1). Based on these results, our cohort of 128 subjects is adequate to calculate *LAA-ACI* of an individual subject.

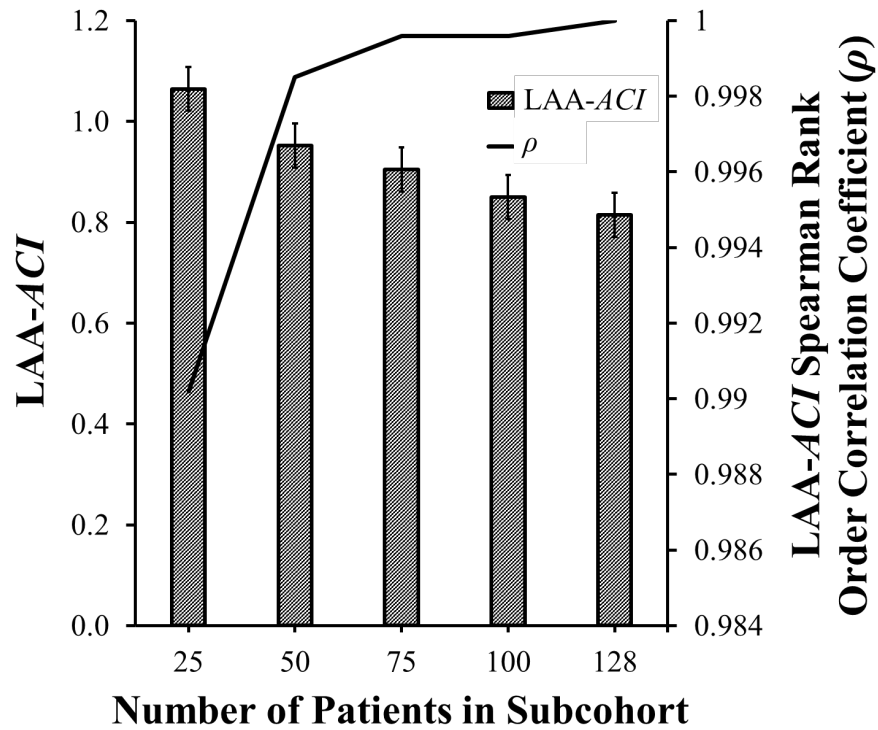
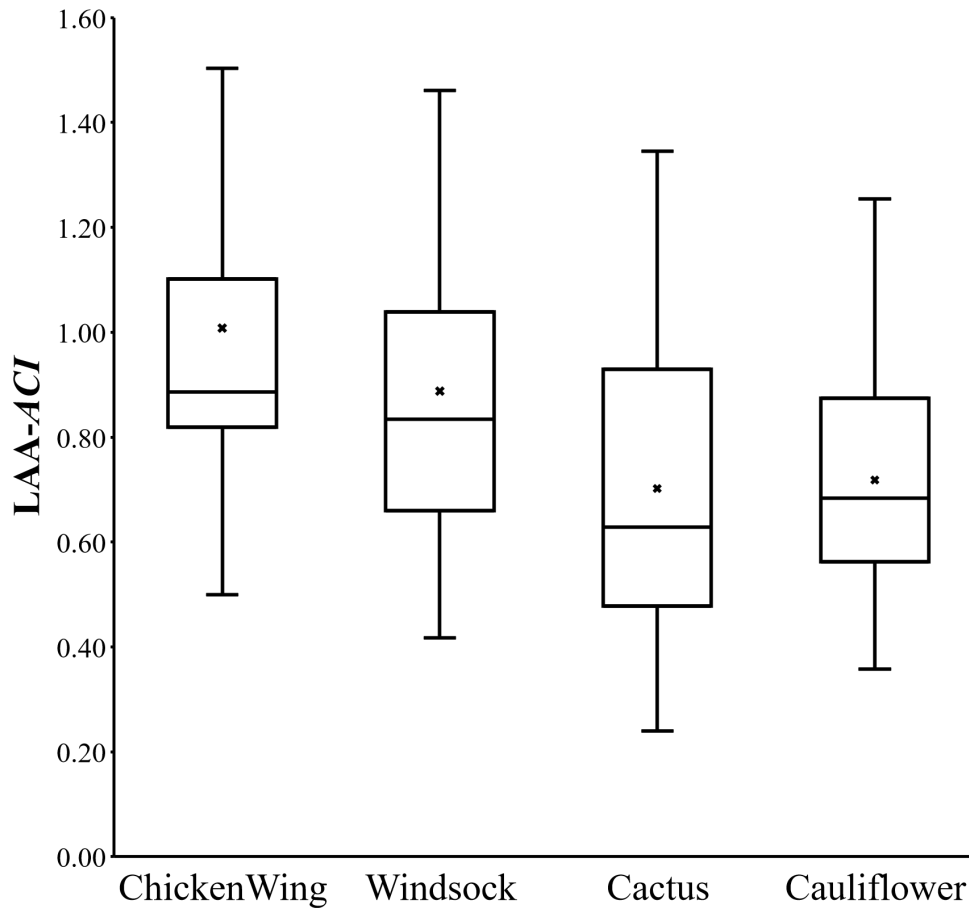


Figure 2.6 Left atrial appendage appearance complexity index (LAA-ACI) and rank order correlation between LAA-ACI calculated using 128 subjects and smaller subcohorts

Bar graph: Values of LAA-ACI (mean  $\pm$  SEM) for the 25 subjects from the reference test group for different number of patients in the subcohort used for the principal component analysis. Solid line: The Spearman rank order correlation coefficient,  $\rho$ , between the LAA-ACI values calculated for the reference test group using the entire cohort of 128 subjects ( $\rho = 1$ , by definition) and LAA-ACI calculated using smaller subcohorts.

### 2.2.4 Relating LAA-ACI to Traditional LAA Shape Classification

The LAA appearance for each of the 128 subjects in the present study was classified into one of four groups based on the study by Di Biase et al. (2012). Group data for LAA-ACI (Figure 2.7) indicated that LAA-ACI had a large variability within each group, resulting in a significant overlap of this index of appearance complexity among the four LAA shape groups.



**Figure 2.7 Left atrial appendage (LAA) Appearance Complexity Index (LAA-ACI) variability among traditional shape groups**

Box plots showing the LAA-ACI for each of the four traditional LAA shape groups. There is large variability in LAA-ACI within each traditional LAA shape group. The lower and upper whiskers represent first quartile and fourth quartile groups, respectively. The “x” represents the mean.

### 2.2.5 Relating LAA-ACI to CHA<sub>2</sub>DS<sub>2</sub>-VASc Score

Spearman rank correlation analysis was performed between LAA-ACI and CHA<sub>2</sub>DS<sub>2</sub>-VASc score (**Figure 2.8**). It appeared that there was a weak negative correlation between LAA-

*ACI* and  $\text{CHA}_2\text{DS}_2\text{-VASc}$  score ( $\rho = -0.1$ ,  $P = 0.26$ ; **Figure 2.8**)<sup>2</sup>, but this did not reach statistical significance.

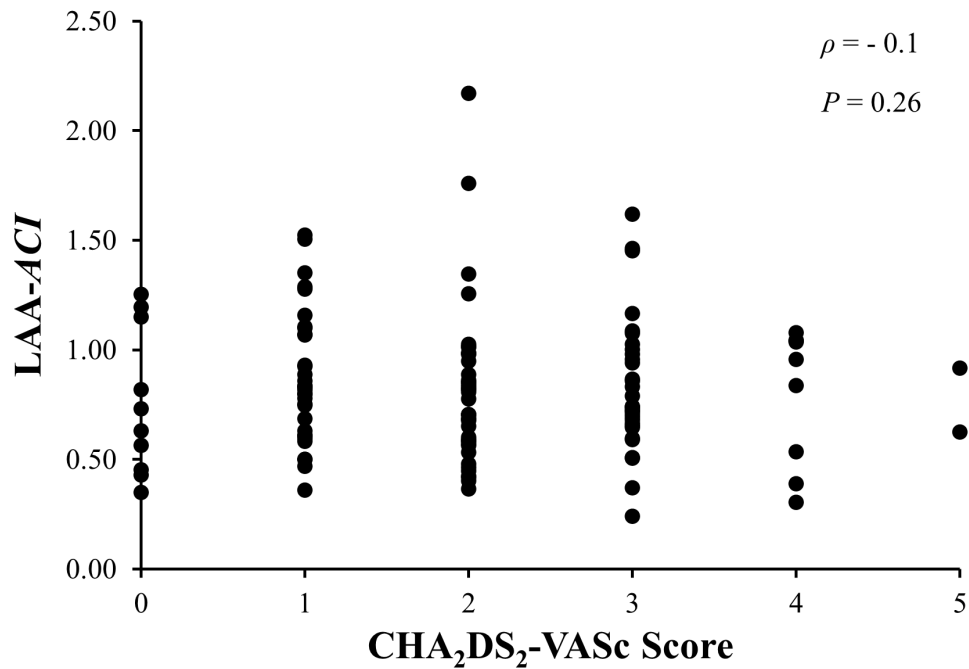


**Figure 2.8 Relationship between left atrial appendage appearance complexity index and  $\text{CHA}_2\text{DS}_2\text{-VASc}$  score**

**Relationship between left atrial appendage appearance complexity index (LAA-*ACI*) and  $\text{CHA}_2\text{DS}_2\text{-VASc}$  score, analyzed using Spearman rank correlation analysis, showing a weak and insignificant correlation.**

### 2.3 Discussion

The idea that the complexity of LAA geometry plays an important role in stroke risk stratification in AF subjects is not new. As discussed in the Introduction Chapter, many indices have been examined in this context, e.g., LAA orifice diameter; number of branches and twigs;

---

<sup>2</sup> Correlation coefficient has been shown by  $\rho$  in italics throughout the document.

degree of coverage with fine structure; LAA volume, depth, and number of lobes; and existence of a bend in LAA (Beinart et al., 2011, Di Biase et al., 2012, Ernst et al., 1995, Khurram et al., 2013, Nedijs et al., 2014). While these are isolated features of the complex LAA geometry, our LAA-*ACI* utilizes the entire 3D dataset, and we believe that this integrated index incorporates the information provided by isolated measures.

In a PCA-based study using a subcohort of 16 patients, we showed that the zero<sup>th</sup> eigenmode (i.e., first PC) of LAA appearance, which explains the highest variances in LAA appearance in the study cohort, had a strong resemblance to the ChickenWing LAA shape, which is reported to have the lowest stroke risk (Di Biase et al., 2012) (**Figure 2.2**). These results lead to a hypothesis that LAA geometries that are known to be associated with a high stroke risk (e.g., Cauliflower and Cactus LAA) require stronger contribution of higher-order PCs in order to reconstruct their respective complex appearance as opposed to LAA variants associated with clinically lower stroke risk (i.e., ChickenWing and Windsock) (**Figure 2.3**). We observed that LAA shapes that are typically associated with low stroke risk could be reconstructed using a low number of PCs (up to 4), while high stroke risk shapes required up to 12 PCs for their reconstruction (**Figure 2.4**). This subcohort study showed the feasibility of quantifying LAA appearance (shape) using PC weights and this PCA-based analysis (i.e., LAA-*ACI*) has the potential to discriminate between high and low stroke risk LAA shapes.

Considering the LAA-*ACI* values for three representative subjects illustrated in **Figure 2.5**, the LAA-*ACI* for subject #1 is the lowest, indicating that this subject has the simplest appearance. Subject #1 has a smoother wall and its total length (length of the LAA centerline from the ostium to the tip) is shorter compared with the other two. The appearance of subject #3 is the most complex, having several lobes (circled regions in **Figure 2.5B**). Furthermore, subject #3 has the

longest length with a bend along its centerline. Although the LAA of subject #2 is smooth, its *ACI* falls in between the other two subjects because of the large bend along its centerline. Thus, our *LAA-ACI* is an objective and quantitative metric that characterizes the complexity of LAA appearance in a holistic way. The next question is whether this integrated index is superior from the perspective of improving the stroke risk stratification. We begin to address this question using a retrospective dataset (**Chapter 5**), but a prospective longitudinal study is necessary to address this question in a definite manner.

Other studies have used the LAA morphology classification paradigm of Di Biase (Di Biase et al., 2012) to characterize LAA shape. As mentioned before, this is a very subjective approach and even experienced cardiologists do not always agree when classifying a given LAA into specific shape categories. In addition, there is a large variability in stroke occurrence within a given LAA shape category (Khurram et al., 2013, Nedioš et al., 2014, Sanatkhani and Menon, 2017, Yaghi et al., 2018). This is consistent with the large variability *LAA-ACI* (**Figure 2.7**) within each shape category. The intercategory *LAA-ACI* variability may explain the differences in the stroke risk seen among subjects with similar overall LAA geometry. This variability underscores the importance of considering subject-specific LA and LAA morphologies in constructing a metric for stroke risk stratification in AF based on hemodynamics.

We found an insignificant negative correlation between the *LAA-ACI* and  $CHA_2DS_2$ -VASc score (**Figure 2.8**), indicating that these two indices are not conveying the same information. There is a large variability of appearance complexity index for a given  $CHA_2DS_2$ -VASc score. This underscores the possibility that *LAA-ACI* has a potential to add information independent of the  $CHA_2DS_2$ -VASc score and consequently, improving the current stroke risk stratification protocol that is solely based on the  $CHA_2DS_2$ -VASc score.

Due to the nature of calculation of LAA complexity, the LAA-*ACI* of a specific patient's LAA cannot be calculated standalone and it requires a cohort of LAA images. The LAA-*ACI* calculated for a specific LAA depends on the cohort that was used to generate the eigen shapes (i.e., principal components) and then calculate the LAA-*ACI* (**Sections 2.1.3 and 2.1.4**). However, the rank order of a group of 25 patient's LAA-*ACI* did not change when we calculated their LAA-*ACI* using larger cohorts (**Figure 2.8**). This suggests that even though LAA-*ACI* of a specific patient varies depending on the cohort that has been used, LAA-*ACI* still can quantify the complexity of LAA images with respect to each other. Undeniably, a larger cohort would provide a better resolution and higher variation between the complexity of different LAAs, but to standardize the LAA-*ACI* values, a fixed reference cohort of LAA images where it includes a vast variety of different LAA morphologies is needed. Then, LAA-*ACI* of each new patient will be calculated using the reference cohort plus the new patient. The cohort 128 patients used in this study was comprised of variety of LAA morphologies and is a good candidate as the reference cohort.

### **2.3.1 Limitations**

We cropped and reoriented all the LAAs in a similar manner. Further, we normalized and centered the contrast of all the images. However, the CCTs were not all acquired at a same condition (i.e., magnification, resolution, contrast, etc.). Calculation of LAA-*ACI* which is based on PCA requires standardized inputs (i.e., LAA images) that have identical properties. A cohort of LAA images where images have identical properties (i.e., magnification, resolution, contrast, etc.) will be needed to improve the results.

Although complexity index was generally high for complex morphologies, in few cases where the morphology was consisted of a long narrow bend, the calculated index was high. This was due to the rarity of these morphologies and an increase in the size of cohort will solve this issue.

### **3.0 Specific Aim 2: Develop a Quantitative Index of LAA Residence Time of Blood-Borne Particles Using a Systems Approach**

It is reasonable to expect that LA and LAA hemodynamics, especially the manner in which blood-borne particles are transported, is an important determinant of thrombi formation and consequently, of the stroke risk. However, the current clinically used stroke risk stratification metric in AF patients, CHA<sub>2</sub>DS<sub>2</sub>-VASc score, does not consider LA and LAA hemodynamics. A computational model to predict blood flow patterns and the transport of blood-borne particles within LAA, the primary site for the origin of most thrombi, can help with objective evaluation of regional stasis (and consequently, cardioembolic stroke) risk. Such a model, in turn, may help with anticoagulant-related therapeutic decision making in AF patients (Di Biase et al., 2012). To develop such a hemodynamics-based tool, we employ computational fluid dynamics (CFD) to calculate mean residence time of blood-borne particles in the LAA ( $t_m$ ), an index of LAA blood stasis, using 3D LA and LAA geometries and LA inlet blood flow (i.e., pulmonary vein flow) data. While subject-specific 3D geometry can be obtained readily, it is not easy to measure all LA inlet blood flow waveforms *in vivo*. Therefore, a sensitivity study of LAA  $t_m$  to the inlet blood flow waveform characteristics (shape and magnitude) has been carried out. In addition, we investigate whether the modeling process should include the non-Newtonian behavior of blood and patient specific hematocrit levels.

## 3.1 Methodology

### 3.1.1 Study Subject Characteristics

A total of 128 patients with symptomatic AF (111 paroxysmal, 17 persistent) were studied (11 males). Patients included in this study were part of another study which goal is to establish a clinical database of patients undergoing evaluation and treatment of AF, including medical management and procedural based treatments (i.e., ablation, device-based therapies with pacemakers/defibrillators, and LAA closure devices) within the Heart and Vascular institute of UPMC hospitals. CCT was performed according to the procedure described in **Section 2.1.1**. University of Pittsburgh Medical Center (UPMC, Pittsburgh, PA, USA). The average age, heart rate, and cardiac output were  $63.6 \pm 9.0$  years (range: 35–79 years), 66 bpm (range: 40–132 bpm), and  $4.0 \text{ L min}^{-1}$  (range 1.5–8.7  $\text{L min}^{-1}$ ), respectively. The range of CHA<sub>2</sub>DS<sub>2</sub>-VASc scores was 0 to 5 (mean =  $2.0 \pm 1.1$ ).

### 3.1.2 Imaging and Segmentation

Contrast-enhanced CCT DICOM images of 128 AF patients having unique LAA morphologies were acquired as explained in **Section 2.1.2**. Images were segmented in 3D to extract the LA surface, including LAA and pulmonary venous inlets, until the mitral valve plane (excluding valvular structures), using marching cube method (iso-contouring), in ParaView, followed by surface preparation steps, including regional smoothing and definition of flat inlets and outlet planes in Geomagic Studio, in order to result in surface models suitable for computational flow studies. The workflow of segmentation process is illustrated in **Figure 3.1**.

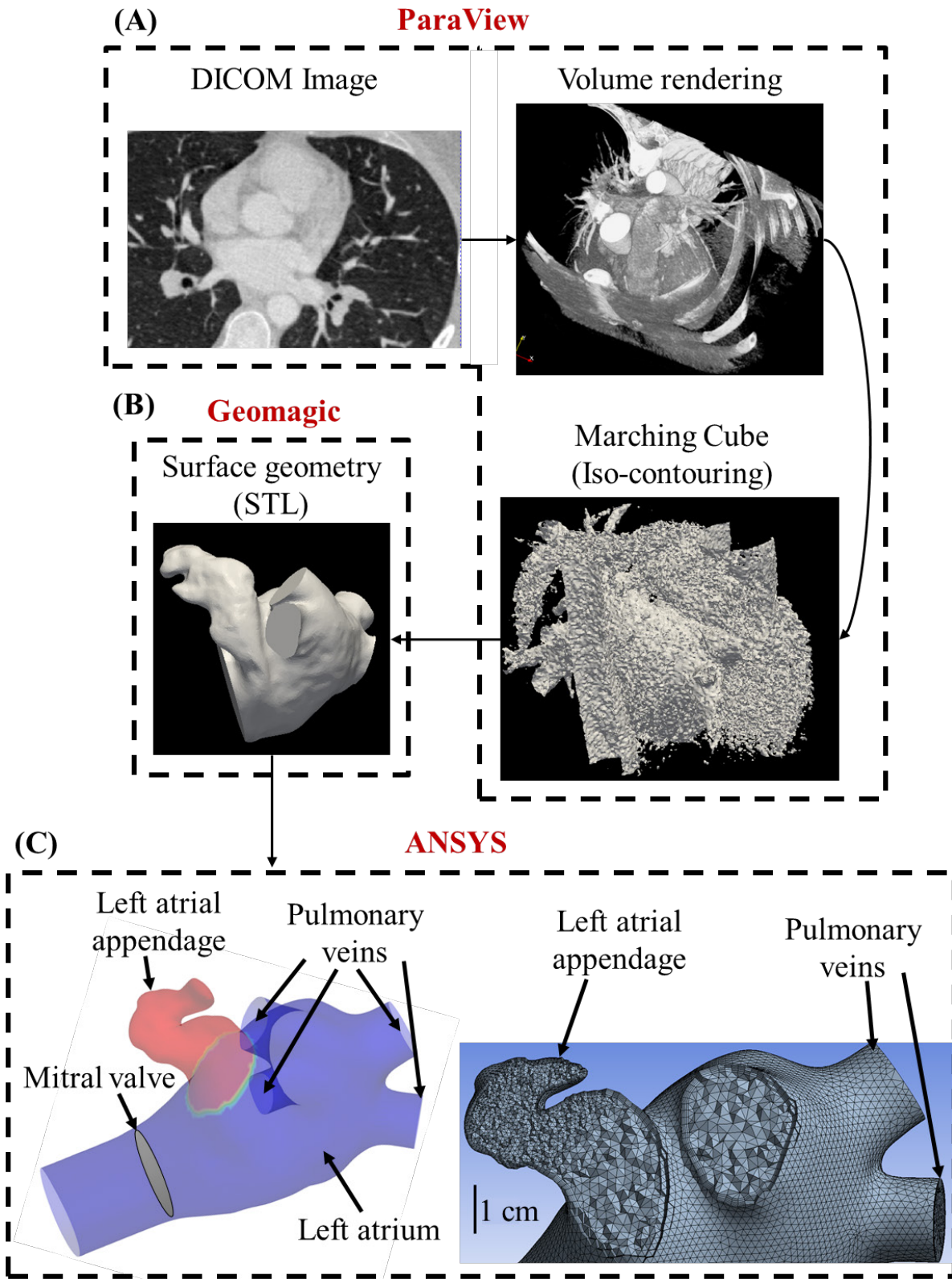


Figure 3.1 LA and LAA segmentation and meshing workflow

DICOM: digital imaging and communications in medicine; STL: stereolithography.

### 3.1.3 Particle image velocimetry

To visualize spatially distributed flow patterns and particle stasis in LAA (Tanne et al., 2008), 2D particle image velocimetry (PIV) was conducted in a representative patient-specific, half-scaled (to reduce the printing costs) physical model of LA and LAA. This patient-specific, physical LA/LAA model consisted of a hollowed block of transparent VeroClear material that was 3D printed using a Stratasys 3D printer (Stratasys Ltd. ©, MN, USA) (**Figure 3.2A**). The physical model was integrated in a mock circulatory loop that circulated  $2.0 \text{ L min}^{-1}$  (to retain the dynamic similarity between the half-scaled model and full-size LA/LAA, the typical AF pulmonary flow,  $\sim 4 \text{ L min}^{-1}$ , was divided by 2) of steady flow water seeded with Thermo Scientific Fluoro-Max red aqueous fluorescent particles (Thermo Fisher Scientific Inc., Waltham, MA USA). The  $0.1 \mu\text{m}$  particles had a density identical to water which made them buoyant. Further, due to their small size, their effect on the flow was negligible. Therefore, they were a good candidate to represent the blood-borne particles. Hoffman clamps were used to distribute the total LA inflow equally among the four pulmonary veins of the LA physical model. An illuminated laser volume within the LAA was used (instead of illuminated sheet) to capture a projection of 3D particle flows in the volume of the LAA (Scarano, 2012). The PIV apparatus used a double-pulse Nd:YAG laser (**Figure 3.2B**), each with energy of 50 mJ per pulse at 532 nm and operated at a repetition rate of 7 Hz and a single charge-coupled device (CCD) camera (model Imager Pro SX 5M, LaVision GmbH, Göttingen, Germany. **Figure 3.2C**). The camera was fitted with a high-pass filter to block laser light (i.e., green, 532 nm) and to transmit the emitted fluorescence of the seeded particles in the flow (i.e., red,  $>590 \text{ nm}$ ). The raw PIV images were preprocessed by subtracting the sliding minimum over a specified time to eliminate background noise followed by a Gaussian smoothing filter to reduce pixel-to-pixel noise and finally particle intensity normalization to reduce high

intensity fluctuations of particles in the flow domain, prior to vector computation, using the LaVision DaVis software (LaVision GmbH, Göttingen, Germany. **Figure 3.2D**).

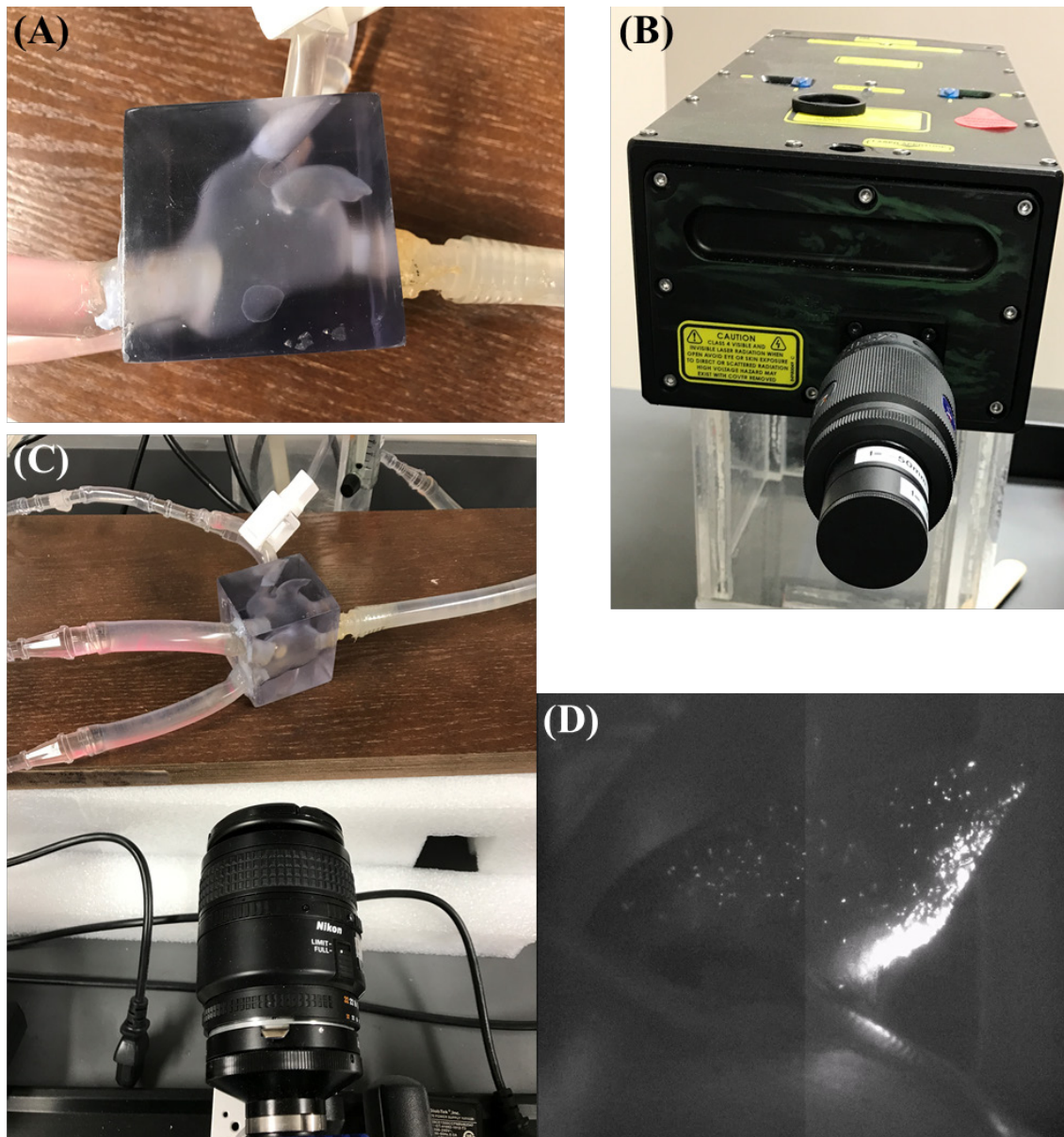


**Figure 3.2 Particle Image Velocimetry (PIV) setup**

**(A)** Hollowed 3D printed block using transparent VeroClear material on a Stratasys 3D printer. **(B)** Double-pulse Nd:YAG laser with 50 mJ per pulse at 532 nm and repetition rate of 7 Hz. **(C)** Single CCD (charge-coupled device) camera (model Imager Pro SX 5M, LaVision) facing the model connected to the circulatory loop. **(D)** Instantaneous screenshot of fluorescence particles inside the left atrial appendage. Reprinted with permission from (Sanatkhani and Menon, 2017)

### 3.1.4 Meshing

The prepared geometries were meshed in ANSYS Meshing. The maximum length for the tetrahedron edge was considered 3.5 mm for the whole geometry (including LA and LAA). Then, mesh was refined based on surface curvature to capture the topology. For instance, mesh at the tip of the LAA is finer than at the center of LA. Five prismatic layers at wall boundaries were used to resolve the boundary layer flow (**Figure 3.1C**). We used these settings for our course mesh. Next, we incrementally increased the number of elements until the changes in asymptotic concentration (see **Section 3.1.8**) in LAA were less than 5%. The number of mesh elements was chosen based on our mesh independency study. Based on the size and tortuosity of each subject, the number of mesh elements varied between 500,000 and 2,000,000 tetrahedrons with the average of ~800,000 tetrahedrons, which was considered acceptable according to the literature (Aguado et al., 2019, Otani et al., 2016).

### 3.1.5 Governing Equations

In this section the governing equations needed to be solved to simulate the flow and blood-borne particles inside the LA and LAA are presented. Using conservation of momentum, the equation of motion (Cauchy's equation of motion) is:

$$\rho \frac{Du_i}{Dt} = \frac{\partial \tau_{ij}}{\partial x_j} \quad \text{Eq. 3.1}$$

<sup>3</sup> where  $D/Dt$  is material derivative,  $t$  is time,  $x$  is coordinate direction,  $\rho$  is density,  $\tau$  is stress tensor, and  $u$  is velocity. Considering blood as a Newtonian fluid, equation of motion can be written in the form of general Navier-Stokes equation (Kundu et al., 2012):

$$\rho \frac{Du_i}{Dt} = -\frac{\partial p}{\partial x_i} + \frac{\partial}{\partial x_j} \left[ 2\mu e_{ij} - \frac{2}{3}\mu(\nabla \cdot \mathbf{u})\delta_{ij} \right] \quad \text{Eq. 3.2}$$

where  $p$  is pressure,  $\delta$  is Kronecker delta,  $\mu$  is viscosity, and  $e_{ij}$  is the strain rate tensor. Using the fact that blood is an incompressible fluid (continuity:  $\nabla \cdot \mathbf{u} = 0$ ) and using vector notation **Eq. 3.2** shrinks to:

$$\rho \frac{D\mathbf{u}}{Dt} = -\nabla p + \mu \nabla^2 \mathbf{u} \quad \text{Eq. 3.3}$$

The blood-borne particles inside the LA and LAA have been simulated by tracer concentration using Eulerian approach. The simplified governing equation to model the transport of tracer concentration is (Kundu et al., 2012):

$$\frac{DC}{Dt} = D_C \nabla^2 C \quad \text{Eq. 3.4}$$

where  $C$  is the tracer concentration and  $D_C$  is diffusion coefficient. In case of pure advection (i.e.,

Peclet number:  $Pe_L = \frac{L \cdot u}{D_C} = \frac{\text{Advection}}{\text{Diffusion}} = \infty$ ;  $D_C = 0$ ) **Eq. 3.4** reduces to:

$$\frac{\partial C}{\partial t} + \mathbf{u} \cdot \nabla C = \frac{\partial C}{\partial t} + \nabla \cdot (\mathbf{u}C) = 0 \quad \text{Eq. 3.5}$$

Blood density was considered  $\rho = 1,060 \text{ kg m}^{-3}$  and in case of Newtonian fluid assumption, the dynamic viscosity was considered  $\mu = 0.00371 \text{ Pa s}$  (Formaggia et al., 2010). The aforementioned governing equations **Eq. 3.3** and **Eq. 3.5** have been discretized using spatial and temporal discretization schemes in OpenFOAM (version 8, The OpenFOAM Foundation Ltd, Inc., UK. See **Section 3.1.8**).

---

<sup>3</sup> In this chapter, vectors are shown in bold and other variables are shown in italics.

### 3.1.6 Quemada Viscosity Model

Due to the focus of this study around the stasis region (very low shear strain rate) inside the LAA, it is important to consider the effects of the shear thinning behavior of whole blood. Further, it has been shown that blood viscosity is very sensitive to hematocrit (Formaggia et al., 2010). To include blood viscosity properties in our model we used generalized Newtonian fluid assumption where viscosity depends on the shear rate. Based on this assumption the constitutive equation for an incompressible fluid using Stokes assumption can be written as follows (Kundu et al., 2012):

$$\tau_{ij} = -\left(p + \frac{2}{3}\mu\nabla \cdot \mathbf{u}\right) \delta_{ij} + 2\mu e_{ij} \quad \text{Eq. 3.6}$$

Eq. 3.6 can be substituted into Eq. 3.1 and by following the procedure in Section 3.1.5, the Navier-Stokes equations and subsequently the governing equations of our problem can be derived. The strain rate tensor in Eq. 3.6 is given by:

$$e_{ij} = \frac{1}{2}\left(\frac{\partial u_i}{\partial x_j} + \frac{\partial u_j}{\partial x_i}\right) \quad \text{Eq. 3.7}$$

Due to the small mesh size, especially inside the LAA, we assumed that a single value of shear strain rate will apply in all directions. With the assumption of generalized Newtonian fluid, we calculated the magnitude of strain rate,  $\dot{\gamma}$ , as follows (Formaggia et al., 2010):

$$\dot{\gamma} = \sqrt{2(e_{ij}e_{ij})} \quad \text{Eq. 3.8}$$

Based on the calculated strain rate,  $\dot{\gamma}$ , at each time-step and each mesh cell the viscosity model was updated to calculate the appropriate apparent viscosity for each cell (Formaggia et al., 2010). The Quemada viscosity model (Cokelet et al., 2005, Hund et al., 2017, Quemada, 1978) has been chosen as a reliable approach to approximate the non-Newtonian behavior of blood especially in

the LAA where strain rate is low. Based on the Quemada model the blood apparent viscosity,  $\mu_a$ , can be calculated as:

$$\mu_a = \mu_p(1 - 0.5kHct)^{-2} \quad \text{Eq. 3.9}$$

where  $\mu_p = 0.00123 \text{ Pa s}$  is plasma viscosity and  $Hct$  is hematocrit level. Coefficient  $k$  and its other related coefficients are calculated using the relations in **Table 3.1**.

**Table 3.1 Quemada viscosity model coefficients**

**H: hematocrit;  $\dot{\gamma}$ : shear strain rate; k: intrinsic viscosity;  $\dot{\gamma}_c$ ,  $k_0$ ,  $k_\infty$ : Quemada coefficients**

---


$$k = \frac{k_0 + k_\infty \sqrt{\dot{\gamma}/\dot{\gamma}_c}}{1 + \sqrt{\dot{\gamma}/\dot{\gamma}_c}}$$

$$k_0 = \exp(3.874 - 10.41Hct + 13.8Hct^2 - 6.738Hct^3)$$

$$k_\infty = \exp(1.3435 - 2.803Hct + 2.711Hct^2 - 0.6479Hct^3)$$

$$\dot{\gamma}_c = \exp(-6.1508 + 27.923Hct - 25.6Hct^2 + 3.697Hct^3)$$


---

For detail information regarding the implementation of governing equation into OpenFOAM code please see **Appendix B.1**.

### 3.1.7 Boundary Conditions

LA and LAA walls were assumed to be rigid, impermeable, and with no-slip boundary conditions where pressure gradient is zero. Furthermore, for simplicity and lowering the computational costs, the mitral valve was assumed to be open throughout the simulation with a Neumann boundary condition where both gauge pressure and velocity gradient set to zero. To prevent outlet backflow divergence, we extended the outlet in our geometries (**Figure 3.1C**) to

develop a uniform flow with zero velocity gradient and zero pressure gradient at the outlets. Inlets were set with a Dirichlet boundary condition where a blood velocity profile was prescribed at PV inlets based on PV flow waveform (**Figure 3.4**). Details regarding the implementation of patient-specific PV inlet boundary conditions are presented in **Appendix B.2**.

### 3.1.8 OpenFOAM Solvers

Our preliminary study indicated that the Reynolds number was highest at the outlet (i.e., at the mitral valve) and this value was in the laminar flow range. Therefore, we solved the governing equations using a laminar solver developed from nonNewtonianIcoFoam solver in OpenFOAM by implementing the Quemada viscosity model into the nonNewtonianIcoFoam solver. We modified the ScalarTransportFoam solver for implementing the tracer transport simulations and conducted the tracer transport-related simulations only after a hemodynamic steady state was reached.

We used the asymptotic tracer concentration inside LAA (**Section 3.1.9**) as our convergence criteria to choose time step for our simulations. A time step of 500  $\mu\text{s}$  was chosen based on a time-step independence study started with a 2 ms time step and decreased this value until the convergence criteria was met. The first-order implicit method was used for time discretization and second-order least-square scheme was used for pressure and velocity gradient discretization. First-order and second-order upwind schemes were used to discretize the divergence terms in the scalar transport equation and the convection term in Navier–Stokes equations, respectively. Pressure, velocity, and concentration tolerances were set to be  $10^{-7}$  Pa,  $10^{-8}$  m/s, and  $10^{-8}$ , respectively. For these simulations, 24 threads of dual 12 core Intel Xeon Gold 6126 CPU with 2.6 GHz clock speed and minimum of 8 GB of RAM were used at the University

of Pittsburgh Computing Research Center. The average execution time for each case in a steady flow using non-Newtonian model was  $\sim 7$  days to simulate 10,000 s of tracer concentration advection through LA/LAA.

### 3.1.9 LAA Residence Time of Blood-Borne Particles

We first ran the fluid dynamics simulations until a hemodynamic steady-state was reached (after  $\sim 25$  cardiac cycles), as defined by the steady state of wall shear stress averaged over the LAA surface area of each subject. Thereafter, we performed simulations to analyze the transport of virtual tracer (i.e., passive scalar, representative of blood-borne particles (cells) that are neutrally buoyant in plasma) out of LAA. These tracer transport-related simulations were initialized with the LAA filled with the tracer concentration,  $C(t)$ , of unity (representing an impulse filling of LAA with the tracer) (**Figure 3.9A**). Tracer advection was simulated using fluid dynamic analysis where the tracer concentration of each cell was calculated in the transport equation coupled with the momentum equations. The volumetric average of tracer concentration inside the LAA,  $C(t)$ , was calculated for 10,000 s. Based on the decay characteristics of  $C(t)$ , we fitted a triple exponential model to  $C(t)$  that included an asymptotic term,  $C_\infty$  (**Eq. A1, Appendix C**).

The dynamics of the tracer clearance from LAA was quantified in terms of the residence time distribution (RTD) function,  $E(t)$  (Fogler, 2016):

$$E(t) = \frac{M(t)}{M_{total}} \quad \text{Eq. 3.10}$$

where  $M(t)$  is the outflow of tracer material (amount of tracer material per unit time) from LAA at the LAA ostium and  $M_{total}$  is the total amount of tracer that leaves LAA over the period 0 to infinity. Thus,  $E(t)$ , with the unit per second, represents the normalized outflow of tracer material from

LAA at time  $t$ . As shown in the **Appendix C**, we can rewrite **Eq. 3.10** in terms of the LAA tracer concentration,  $C(t)$ , as follows:

$$E(t) = \frac{[C(t)-C(t+\Delta t)]}{\Delta t(1-C_\infty)} \quad \text{Eq. 3.11}$$

where  $\Delta t$  and  $C_\infty$  are the time increment used in the finite difference-based estimation of  $M(t)$  (**Eq. A3, Appendix C**) and the asymptotic LAA concentration remaining in the LAA (**Eq. A1, Appendix C**), respectively. Two measures of the propensity of particles to stay within the LAA were calculated: mean residence time,  $t_m$ , which is the first moment of  $E(t)$  (**Eq. A6, Appendix C**), and  $C_\infty$  [ $C_\infty = C(t \rightarrow \infty)$ , **Eq. A1, Appendix C**]. A larger value for either of these two indices is expected to increase the clot formation risk.

## 3.2 Results

### 3.2.1 CFD Validation

A PIV study on a sample LA/LAA geometry was performed to assess the validity of our CFD simulations. A series of CFD simulations on the same LA/LAA geometry was performed using similar flow conditions as in the experimental PIV setup wherein tracer concentration (representative of blood cells/florescent particles) was injected at pulmonary vein inlets of a LA/LAA geometry. It should be noted that this florescent particle injection protocol in the PIV study was different from the one used in the CFD simulations for calculating LAA  $t_m$  and  $C_\infty$ : the tracer material was injected directly in LAA in an impulse-like fashion in case of the CFD simulations for calculating LAA  $t_m$  and  $C_\infty$ .

Assuming diffusivity for tracer transport (i.e., diffusion coefficient,  $D > 0 \text{ m}^2 \text{ s}^{-1}$ ) increases the rate of tracer concentration washout significantly and consequently reduces the computational time to calculate the residence time significantly. To investigate the feasibility of using diffusion term in our transport equation for our final simulations, the tracer transport in the sample LA/LAA geometry was simulated using three different diffusivities,  $D$ , in three separate CFD simulations: 1)  $D = 0 \text{ m}^2 \text{ s}^{-1}$  (pure advection transport), 2)  $D = 1 \text{ m}^2 \text{ s}^{-1}$  (pure diffusion transport), and 3)  $D = 0.01 \text{ m}^2 \text{ s}^{-1}$  (transport with equally important advection and diffusion processes. i.e., Peclet number,  $Pe_L = \frac{L \cdot u}{D} = \frac{\text{Advection}}{\text{Diffusion}} = 1$ ). Results of the CFD simulations were compared with the experimental data obtained in the PIV study.

Two recirculation zones in the LAA were observed in both the CFD simulation (**Figure 3.3C**) and the PIV experiment (**Figure 3.3B**), one with low velocity (i.e., blue colored) at the distal tip of the appendage and the other with high velocity close to the LAA ostium. The experimental results revealed that neutrally buoyant fluorescent particles deposit and remain stagnant within the appendage around the upper wall and towards the tip of LAA (**Figure 3.3B**). Accumulation of tracer concentration observed in the CFD simulation using pure advection transport condition ( $D = 0 \text{ m}^2 \text{ s}^{-1}$ ) was in the same regions as in the PIV experimental study (**Figure 3.3D** vs. **Figure 3.3B**). In contrast, the CFD results based on  $D > 0 \text{ m}^2 \text{ s}^{-1}$  condition depicted the tip of LAA as the only region with high tracer concentration, which does not match with the experimental result.

The matching flow pattern and regions of particle accumulation in PIV experiment and CFD simulation with pure advection transport ( $D = 0 \text{ m}^2 \text{ s}^{-1}$ ) provides a reasonable validation of our CFD-based analysis. Therefore, we assumed that the diffusion term in the transport of tracer material plays a very small role in our CFD simulations (Kim et al., 2004).

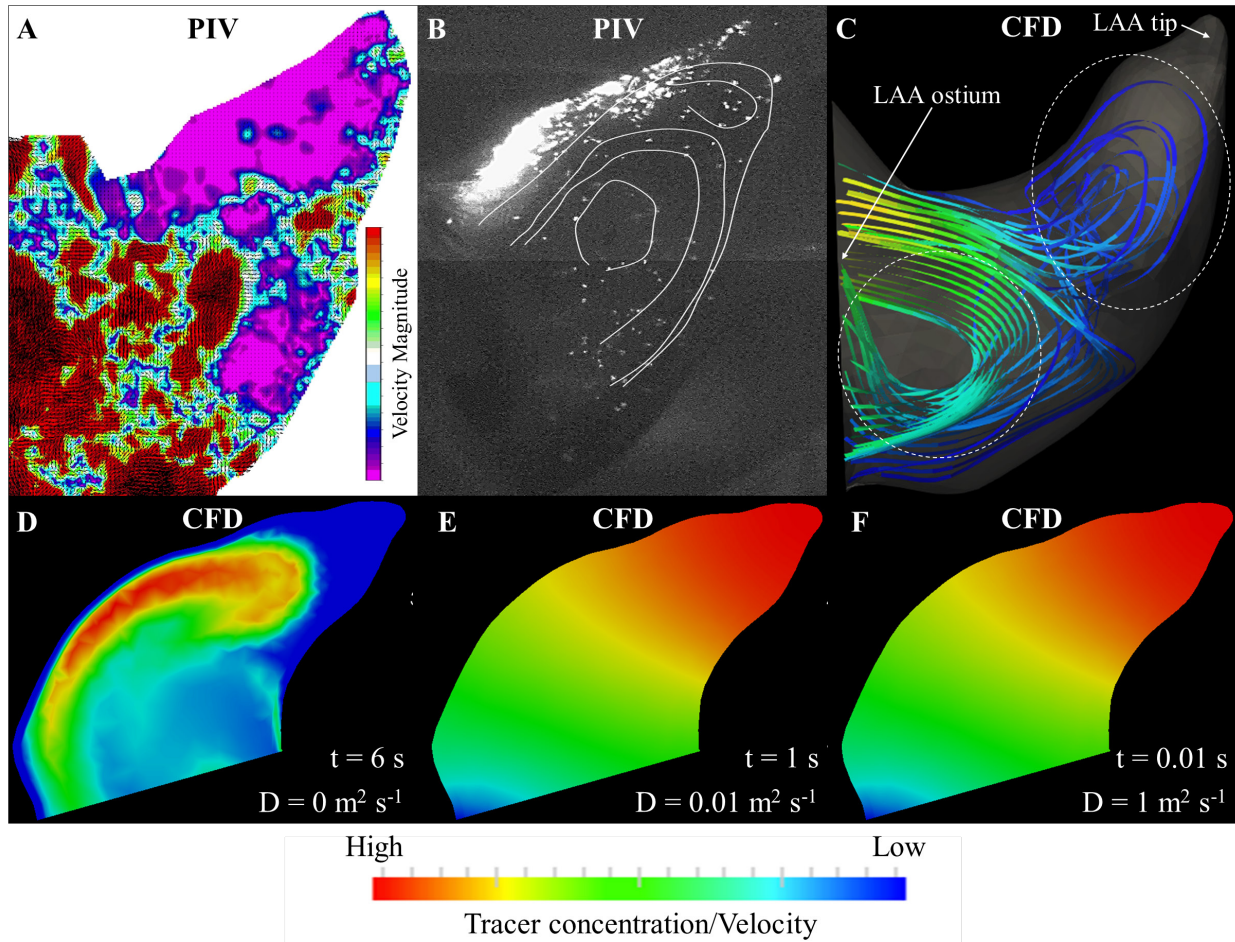


Figure 3.3 CFD assessment using particle image velocimetry

A) particle image velocimetry (PIV) vector computation result colored with flow velocity magnitude, normalized from minimum (blue for stasis i.e.,  $|V| = 0$  m/s) to maximum (red), for particles seen in a projection of the illuminated left atrial appendage (LAA) volume. Stasis region is observed at the upper edge of the LAA. B) Approximate path-lines of the particles (manually traced as white lines) in the appendage, superimposed on an instantaneous screenshot of the same projection plane. The fluorescent particles are accumulated at the upper edge of the LAA, corresponding with blue regions of stasis seen in (A). C) CFD generated streamlines of flow in the LAA, colored by velocity magnitude, normalized by minimum to maximum, from blue to red. The recirculation regions (shown with dotted circles) seen in (C) matches with the recirculation areas seen in (B). There are two recirculation regions seen in (C) and (B), one with low velocity (i.e., blue colored) at the distal tip of the appendage and the other with high velocity close to the LAA ostium. Further, blue stasis regions in (C) matches with the blue stasis regions in the experimental results (A).

**(D-F) Contours of tracer concentrations in a plane inside the LAA based on three separate CFD simulations using three different diffusivity condition for tracer transport (i.e.,  $D = 0, 0.01, \text{ and } 1 \text{ m}^2 \text{ s}^{-1}$ ). Due to different tracer washout rate in each simulation, different timepoints have been used to show the tracer transport (D-F). The high tracer concentration region in pure advection model (D) matches with the experimental results (B), however, this pattern is different in (E) and (F). In both (B) and (D) particles and tracer have high concentration along the top edge of the LAA towards the tip. Reprinted with permission from (Sanatkhani and Menon, 2017)**

### **3.2.2 Confounding Variables**

There are various confounding variables that can affect regarding the CFD-based modeling of hemodynamics and particle transport and consequently, the calculation of LAA residence time. In this section we present the results of our subcohort studies carried out to examine the effects of each of the confounding variables. These results helped us optimize the CFD-based simulation protocol.

#### **3.2.2.1 Pulsatility**

Patient-Specific 3D geometry can be obtained readily, however, it is not easy to measure all PV inlet blood flow waveforms *in vivo*. A sensitivity study of LAA residence time to the inlet blood flow waveform characteristics (shape and magnitude) is needed to examine whether the nature of the inlet flow (steady vs. pulsatile) affects LAA residence time. To investigate the effects of PV blood flow waveform, various PV blood flow waveforms were generated by modifying a template normal waveform (**Figure 3.4A**). In a subcohort of 25 patients, each subject was simulated using 9 settings of PV inlet blood flow characteristics: three levels of mean PV blood flow (i.e., cardiac output of 3.3, 4.4, and 5.5 L min<sup>-1</sup>) and three types of PV flow waveform

(pulsatile waveform seen in a typical normal subject, pulsatile waveform seen in a typical AF subject, and steady with no pulsatility; **Figure 3.4A-C**) for each level of cardiac output. The mean residence time of blood-borne particles in LAA, LAA  $t_m$ , and asymptotic concentration inside LAA,  $C_\infty$ , were quantified in each simulation. Both LAA  $t_m$  and  $C_\infty$  decreased significantly as cardiac output was increased, regardless of PV waveform type (**Figure 3.4D**).

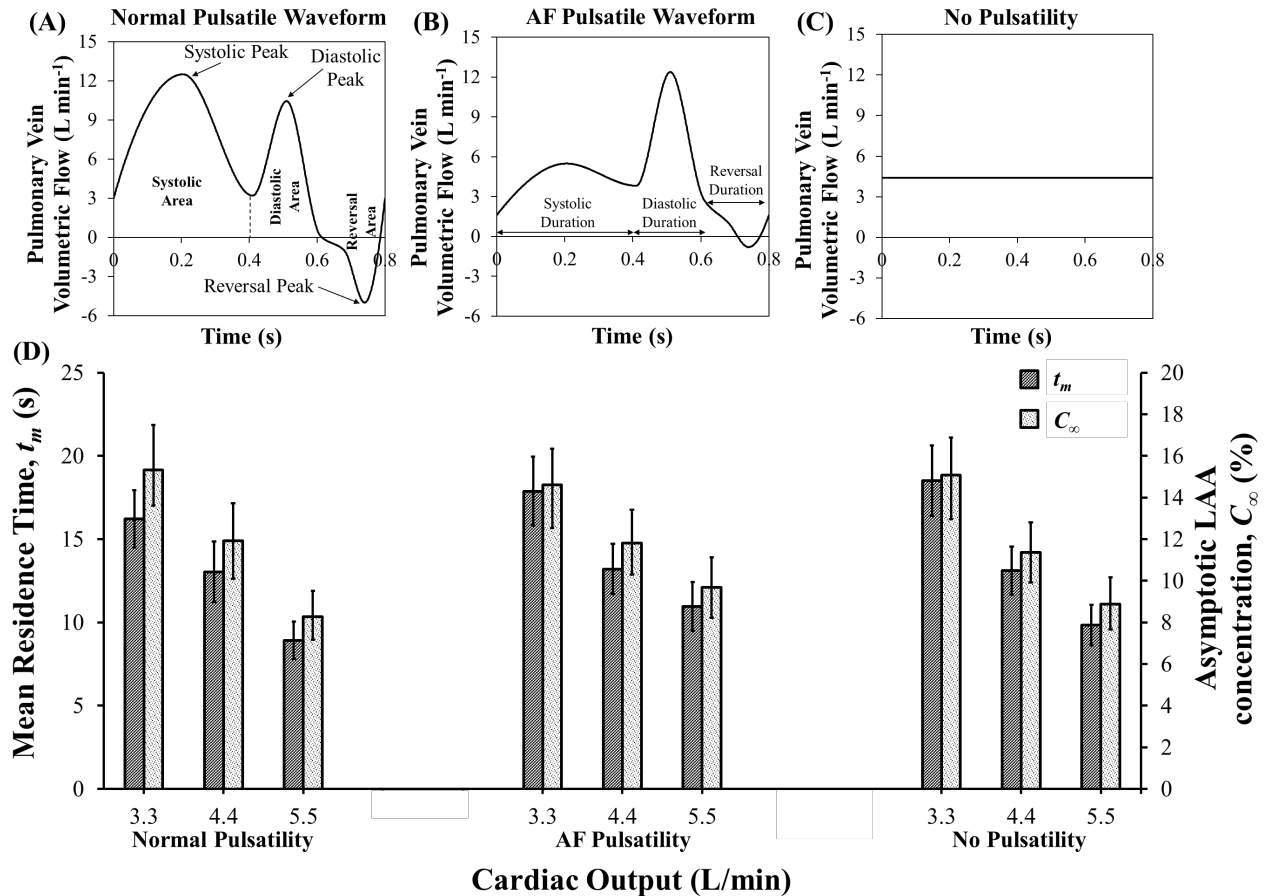


**Figure 3.4** Three pulmonary vein flow waveform types and their relation with the hemodynamic indices (A) Normal pulsatile pulmonary vein (PV) flow waveform. Systolic, diastolic, and reversal areas in during one cardiac cycle are shown. Further, the peak of each period is pointed out. (B) Pulsatile PV flow waveform that is seen in a typical atrial fibrillation patient. Systolic, diastolic, and reversal durations are marked. (C) PV flow waveform with no pulsatility. (D) Mean residence time and asymptotic concentration in left atrial appendage corresponding to different PV flow waveforms and cardiac outputs for a cohort of 25 patients.

**Data:** Mean  $\pm$  SEM.

To investigate the effects of pulsatility of PV blood flow waveforms, we characterized PV blood flow waveform pulsatility in terms of several parameters (**Table 3.2**). Next, we performed four series of multiple linear regression analyses to investigate the effects of cardiac output (3 levels) and the PV waveform pulsatility using the defined parameters (each time using one method of waveform characteristics parameters in **Table 3.2**). We used 24 dummy variables to account for the inter-subject variability:

$$D_i = \begin{cases} 1, & \text{Subject } i \\ 0, & \text{Otherwise} \\ -1, & \text{Subject 25} \end{cases} \quad \text{Eq. 3.12}$$

The raw data used in this analysis are presented in **Appendix D**. These analyses revealed that only cardiac output was a significant independent variable ( $P < 0.0001$ ). Based on this study, an increase of  $1 \text{ L min}^{-1}$  in cardiac output decreases the LAA  $t_m$  by  $3.5 \text{ s}$  ( $\pm 0.8 \text{ s}$ ;  $adj-R^2 = 0.7$ ;  $P < 0.0001$ ) and  $C_\infty$  by  $2.8\%$  ( $\pm 0.5 \text{ s}$ ;  $adj-R^2 = 0.8$ ;  $P < 0.0001$ ).

**Table 3.2 PV Blood flow waveform pulsatility indices**

Pulmonary vein flow waveform characteristics parameters definitions are presented. Further, their value corresponding to each waveform type (pulsatile waveform seen in a typical normal subject, pulsatile waveform seen in a typical atrial fibrillation (AF) patient, and steady with no pulsatility; Figure 3.4A-C) and cardiac output are shown. Systolic/diastolic/reversal area and systolic/diastolic/reversal peak are shown in Figure 3.4A and B.

Methods	Waveform Characteristics Parameter	Normal Pulsatile Waveform	AF Pulsatile Waveform	No Pulsatility
	Cardiac Output (L min <sup>-1</sup> )	3.3 4.4 5.5	3.3 4.4 5.5	3.3 4.4 5.5
1	Normalized Systolic Duration = $\frac{\text{Systolic Area}}{\text{Systolic Duration} \times \text{Cardiac Output}}$	1.5 1.49 1.52	1.11 0.95 1.08	1 1 1
	Normalized Diastolic Duration = $\frac{\text{Diastolic Area}}{\text{Diastolic Duration} \times \text{Cardiac Output}}$	0.78 0.58 0.55	1.24 0.9 0.72	1 1 1
	Normalized Reversal Duration = $\frac{\text{Reversal Area}}{\text{Reversal Duration} \times \text{Cardiac Output}}$	0.32 0.44 0.39	0.39 0.12 0.14	1 1 1
2	Normalized Systolic Peak = $\frac{\text{Systolic Peak}}{\text{Cardiac Output}}$	2.25 2.18 2.27	1.55 1.25 1.54	1 1 1
	Normalized Diastolic Peak = $\frac{\text{Diastolic Peak}}{\text{Cardiac Output}}$	1.54 1.81 1.9	2.4 2.82 2.37	1 1 1
	Normalized Reversal Peak = $\frac{ \text{Reversal Peak} }{\text{Cardiac Output}}$	0.64 0.91 0.91	0.61 0.18 0.21	1 1 1
3	Systolic-Diastolic Ratio = $\frac{\text{Systolic Peak}}{\text{Diastolic Peak}}$	1.46 1.21 1.2	0.64 0.44 0.65	1 1 1
4	Pulsatility Index = $\frac{\text{Max Peak} +  \text{Min Valley} }{\text{Cardiac Output}}$	2.88 3.09 3.18	2.16 1.43 1.75	0 0 0

We next investigated whether the pulsatile nature of the inlet flow waveform affect the rank ordering of patients. The Spearman rank correlation analysis was performed using calculated LAA  $t_m$  values for the normal pulsatile waveform and the waveform with no pulsatility at all three level of cardiac output. A similar analysis was performed using calculated LAA  $t_m$  values for the AF pulsatile waveform and the waveform with no pulsatility. All Spearman rank order correlation coefficients were found to be significant (**Table 3.3**).

**Table 3.3 Spearman rank correlation coefficient for left atrial appendage mean residence time (LAA  $t_m$ ) obtained with pulmonary vein waveform with no pulsatility and two other waveform types**

**Normal Pulsatility:** pulsatile waveform seen in a typical normal subject; **AF Pulsatility:** pulsatile waveform seen in a typical atrial fibrillation (AF) patient; **No Pulsatility:** steady with no pulsatility.

		No Pulsatility		
		3.3	4.4	5.5
Normal Pulsatility	Cardiac Output (L min <sup>-1</sup> )			
	3.3	$\rho = 0.67$ $P = 0.0003$		
	4.4		$\rho = 0.76$ $P < 0.0001$	
	5.5			$\rho = 0.72$ $P < 0.0001$
AF Pulsatility	3.3	$\rho = 0.77$ $P < 0.0001$		
	4.4		$\rho = 0.83$ $P < 0.0001$	
	5.5			$\rho = 0.73$ $P < 0.0001$

According to these results LAA blood stasis risk, as quantified by LAA  $t_m$  and  $C_\infty$ , is significantly affected by the mean value of inlet flow (i.e., cardiac output), but not by temporal pattern of the inlet flow. Therefore, the patient-specific LAA blood stasis risk can be reliably estimated using patient-specific LA and LAA 3D geometries and patient-specific cardiac output, without any need for patient-specific PV blood flow waveform.

### 3.2.2.2 Hematocrit and Non-Newtonian Fluid

A subcohort consisting of 25 patients was chosen to investigate the effects of hematocrit level and non-Newtonian behavior of blood on the calculated indices (LAA  $t_m$  and  $C_\infty$ ). The non-Newtonian behavior of blood was simulated for three different hematocrit levels ( $Hct = 27.4\%$ ,

45.5%, and 60.4%) using the Quemada viscosity model. Further, the equivalent Newtonian viscosity of each hematocrit level was calculated based on **Figure 3.5** ( $\eta = 2.4 \times 10^{-6}$ ,  $3.5 \times 10^{-6}$ , and  $5.1 \times 10^{-6} \text{ m}^2 \text{ s}$  for  $Hct = 27.4\%$ ,  $45.5\%$ , and  $60.4\%$ , respectively). Six CFD-based simulations were conducted for each subject: non-Newtonian and Newtonian behavior of blood for each of the 3 levels of hematocrit. A pulmonary vein flow waveform with no pulsatility with cardiac output of  $4.4 \text{ L min}^{-1}$  was used in these simulations.

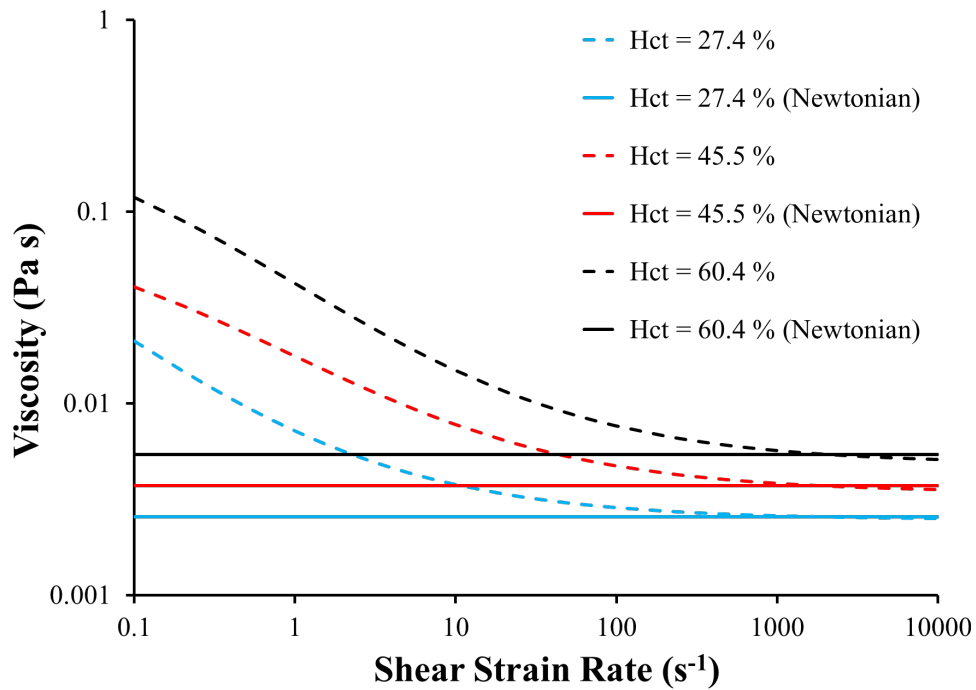


**Figure 3.5 Blood viscosity as a function of shear strain rate and hematocrit using Quemada viscosity model and Newtonian fluid model**

The equivalent Newtonian viscosity of each hematocrit level was calculated based on the corresponding viscosity calculated using Quemada model at  $\dot{\gamma} = 2000 \text{ s}^{-1}$ . Hct: hematocrit.

Both LAA  $t_m$  and  $C_\infty$  were lower for a hematocrit level using the Newtonian model compared with their corresponding values in the non-Newtonian model. In both Newtonian and non-Newtonian models, both LAA  $t_m$  and  $C_\infty$  increased with increasing hematocrit level (**Figure 3.6**). A multiple linear regression analysis was performed using CFD simulation results with the

non-Newtonian fluid characterization (Quemada viscosity model). A variable for hematocrit ( $Hct = 27.4\%$ ,  $45.5\%$ ,  $60.4\%$ ) and 24 dummy variables (to account for inter-subject variability similar to **Section 3.2.2.1**) were used in the regression equation. Hematocrit level was found to be a significant independent variable for both LAA  $t_m$  ( $\beta = 1.02 \pm 0.15$ ;  $adj-R^2 = 0.58$ ;  $P < 0.0001$ ) and  $C_\infty$  ( $\beta = 0.66 \pm 0.05$ ;  $adj-R^2 = 0.84$ ;  $P < 0.0001$ ); both LAA  $t_m$  and  $C_\infty$  increase with an increase in the hematocrit level.

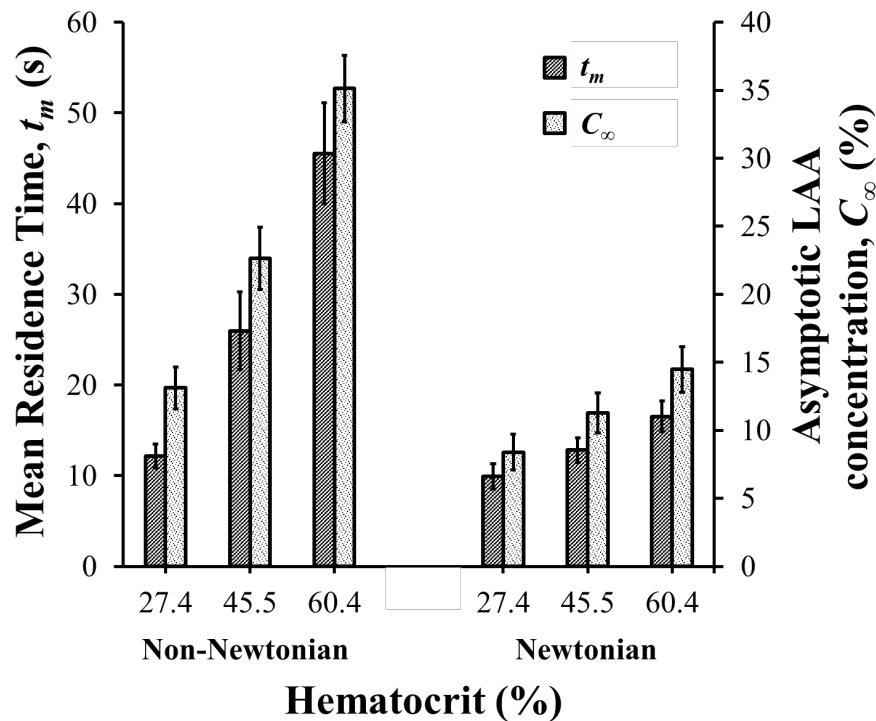


**Figure 3.6 Mean residence time and asymptotic concentration inside left atrial appendage as a function of hematocrit using Newtonian and non-Newtonian models.**

**Left atrial appendage mean residence time, LAA  $t_m$ , LAA asymptotic concentration,  $C_\infty$ , increased as a function of cardiac output. Data: Mean  $\pm$  SEM.**

To examine whether the fluid characterization (Newtonian vs. non-Newtonian) affects the rank ordering of patients, we performed the Spearman rank correlation analysis of results obtained using the Newtonian model and the non-Newtonian model (i.e., Quemada model). Based on 150 simulations (75 Newtonian and 75 non-Newtonian), LAA  $t_m$  and  $C_\infty$  from the non-Newtonian

model and the Newtonian model were highly correlated ( $\rho = 0.75$ ,  $P < 0.0001$  for LAA  $t_m$  and  $\rho = 0.82$ ,  $P < 0.0001$  for LAA  $C_\infty$ ).

In conclusion, we have to use patient-specific hematocrit as one of our inputs for our CFD simulations. Although absolute values of LAA  $t_m$  and  $C_\infty$  are affected by the fluid characterization (Newtonian vs. non-Newtonian), the rank ordering of patients using the two characterizations are highly correlated. This suggests that the non-Newtonian model of blood may not be necessary. However, the increase in computational cost when using a non-Newtonian model was insignificant. Therefore, patient-specific hematocrit with a non-Newtonian behavior of blood based on the Quemada viscosity model were used in the final simulations.

### 3.2.2.3 Length of Simulation

In theory, one needs to continue the CFD-based simulation of tracer transport to infinite time for calculating the mean residence time; this is not possible. Therefore, simulations have to be truncated at some point and predicted values based on a decay function are used to calculate LAA  $t_m$  and  $C_\infty$ . Depending on the wellness of the fitting function and truncation time, calculated LAA  $t_m$  and  $C_\infty$  values will differ from their theoretical values that can be only calculated at infinite time (Curl and McMillan, 1966). Based on our study, the temporal pattern of the LAA tracer concentration decay following an impulse injection of tracer is complex – it is certainly not a single exponential decay. We chose a triple exponential decay function (capable of fitting to a period of fast tracer washout at the beginning of simulation, moderate washout rate in the middle, and slow washout rate at the end of the simulation) (**Appendix C.1**) as a compromise between over fitting and accuracy. It is important to know what minimum length of simulation is necessary for a reliable calculation of the mean residence time.

To examine the adequacy of simulation length, we used a subcohort of 25 patients and calculated LAA  $t_m$  and  $C_\infty$  after running the CFD-based simulation for a long time—30,000 s. It was expected that the calculated LAA  $t_m$  and  $C_\infty$  values would reach an asymptotic steady state at the end of this lengthy simulation. Next, LAA  $t_m$  and  $C_\infty$  data were calculated using shorter simulation times and compared with the result the 30,000 s simulation results. as a function of simulation length, the mean of LAA  $t_m$  and  $C_\infty$  increased and decreased, respectively (**Figure 3.7**). Although some individual subjects reach steady-state after 30,000 s of simulation, it does not appear that the mean LAA  $t_m$  and  $C_\infty$  for the subcohort of 25 patients reach steady-state values.

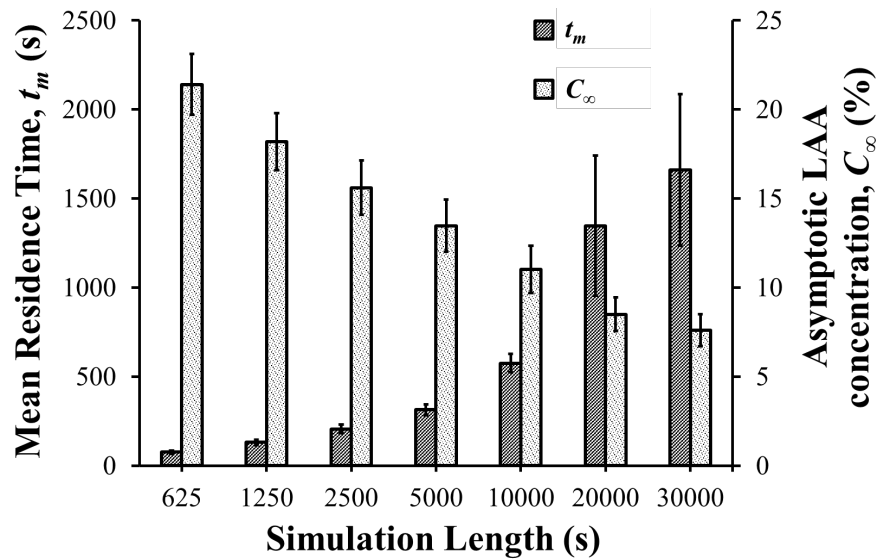


**Figure 3.7** Left atrial appendage mean residence time, LAA  $t_m$ , and asymptotic concentration,  $C_\infty$  as a function of simulation length

**LAA  $t_m$  and  $C_\infty$  did not reach a steady state even after 30,000 s of simulation. Data: Mean  $\pm$  SEM.**

Although reaching a steady state is ideal, the consistency of the rank order of patients is more important. Spearman rank order correlation analyses between LAA  $t_m$  and  $C_\infty$  values calculated using 30,000 s simulation and results based on shorter simulation lengths were performed. Based on these results, 10,000 s found to be a sufficient length to calculate LAA  $t_m$  ( $\rho$

= 0.73,  $P < 0.0001$ ; **Figure 3.8A**) and  $C_\infty$  ( $\rho = 0.95$ ,  $P < 0.0001$ ; **Figure 3.8B**); this simulation duration was used in the final simulations.

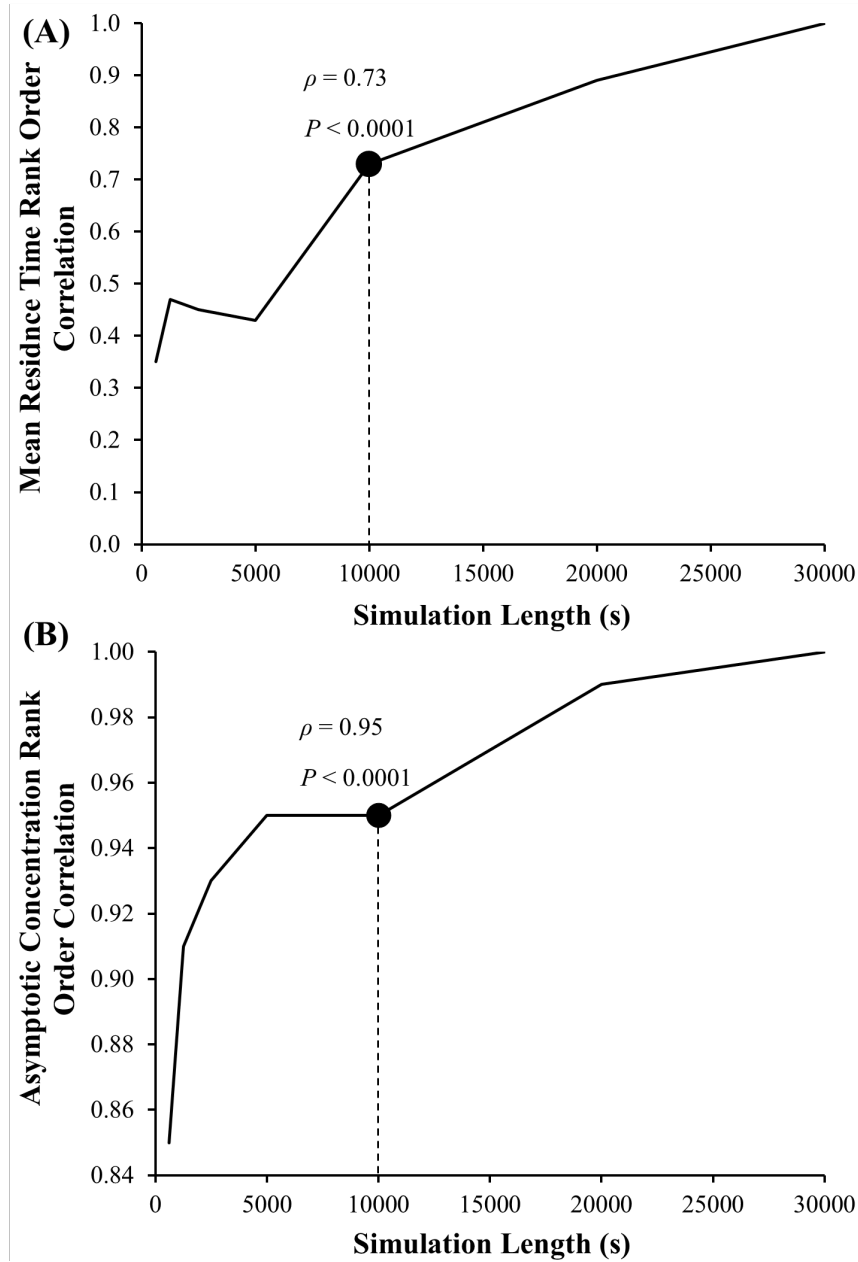


**Figure 3.8 Left atrial appendage mean residence time, LAA  $t_m$ , and asymptotic concentration,  $C_\infty$  rank order correlation coefficient as a function of the length of simulation**

The Spearman rank order correlation coefficient,  $\rho$ , between the LAA  $t_m$  and  $C_\infty$  for the reference group using 30,000 s of simulation ( $\rho = 1$ , by definition) and LAA  $t_m$  and  $C_\infty$  calculated using smaller simulation

lengths.

### 3.2.3 Relating LAA RTD Function to Traditional LAA Shape Classification

The  $C(t)$  curve for a representative subject is shown in **Figure 3.9A**. The tracer washed out from the regions close to the LAA ostium after 2–10 s and tracer concentration continued to be high at the tip of the LAA even at the end of the simulation ( $t = 10,000$  s).

The RTD function,  $E(t)$ , for three representative subjects (same as those in **Figure 2.5**) is illustrated in **Figure 3.9B**, starting with  $t = 1000$  s until the end of simulation ( $t = 10,000$  s) to better focus on the tail area of the  $E(t)$  curve. Subject #2 started with lower initial normalized rate of tracer washout,  $E(t)$ , across the LAA ostium, however, the rate of washout in subject #1 and #3 decayed faster compared to subject #2 as time progressed. Based on these  $E(t)$  curves and associated  $t_m$  values, the tracer exited from the LAA of subject #3 the fastest, followed by subjects #1 and subject #2 in that order.

The LAA morphology for each of the 128 subjects in the present study was classified into one of four groups based on the study by Di Biase et al. (2012). Group data for LAA  $t_m$  (**Figure 3.9C**) indicated that LAA  $t_m$  had a large variability within each group, resulting in a significant overlap of this index of RTD function among the four LAA shape groups.

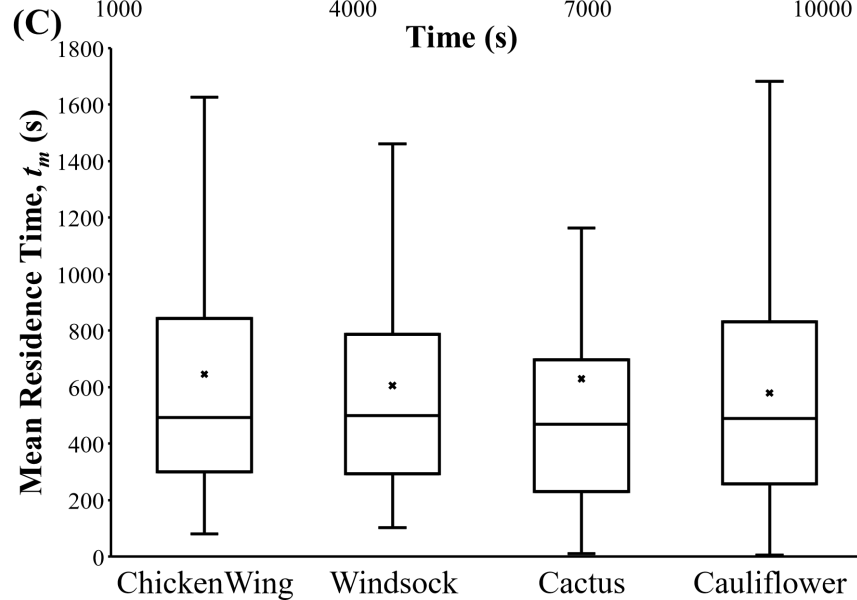
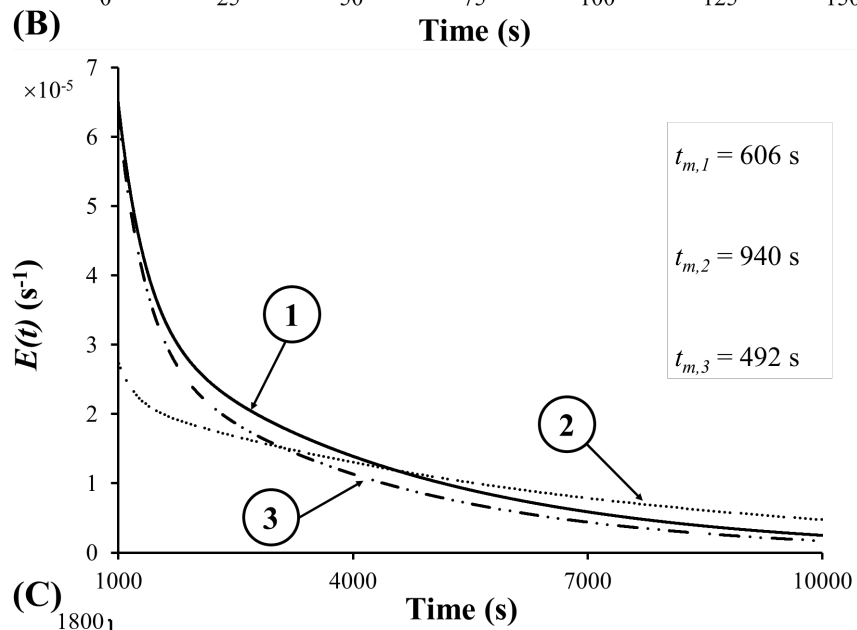
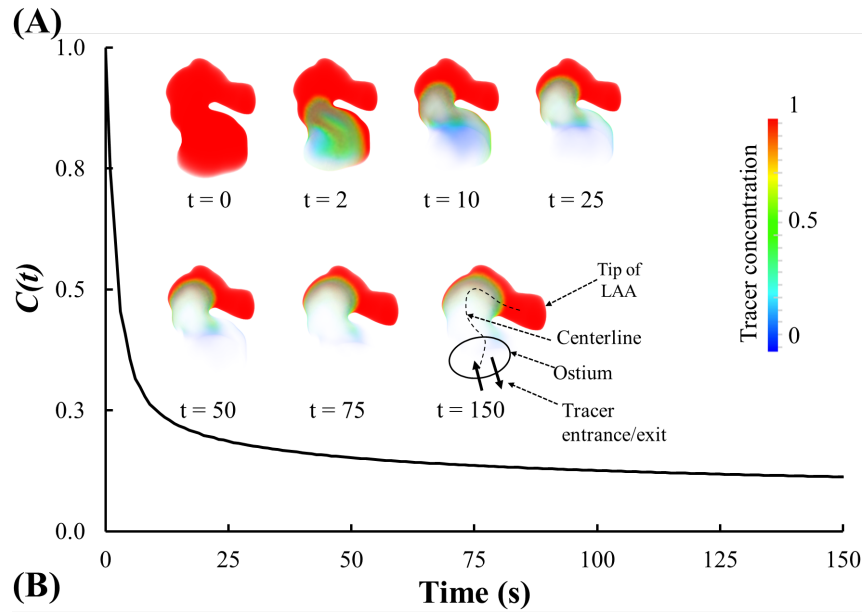


**Figure 3.9 Tracer concentration washout, residence time function, and mean residence time intercategory variability**

(A) Spatially averaged LAA tracer concentration,  $C(t)$ , plotted as a function of time for a representative LAA. Inset: Tracer concentration contours for selected time, illustrating the tracer washout from most of the LAA, except for the tip of the LAA. (B) the residence time distribution function,  $E(t)$ , quantifying the normalized rate of tracer washout across the LAA ostium, as a function of time for three representative subjects. Data for the first 100 s are shown to highlight the early washout. (C) Box plots showing the mean residence time,  $t_m$ , for each of the four traditional LAA shape groups. First and third quartiles are shown via error bars. There is large variability in  $t_m$  within each traditional LAA shape group.

### 3.2.4 Relating LAA Mean Residence Time to LAA Asymptotic Tracer Concentration

The propensity of particles to stay within the LAA was characterized in terms of two indices: LAA mean residence time,  $t_m$ , and LAA asymptotic tracer concentration,  $C_\infty$ . Spearman rank correlation analysis showed that there was a significant positive correlation between these two indices ( $\rho = 0.69$ ,  $P < 0.0001$ ; **Figure 3.10**), suggesting that only one of these indices may be sufficient to characterize the propensity of particles to stay within LAA.

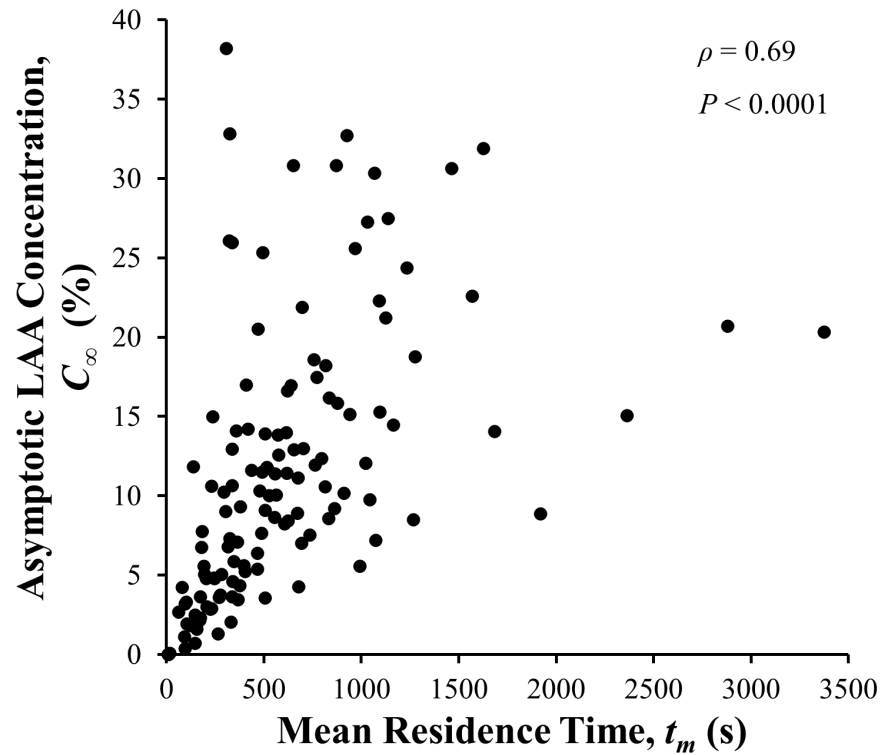


**Figure 3.10 Relationship between the two indices of left atrial appendage (LAA) residence time distribution (RTD) function: mean residence time,  $t_m$ , and asymptotic LAA concentration,  $C_\infty$ .**

The Spearman rank correlation analysis indicates that LAA  $t_m$  and  $C_\infty$  are highly correlated, suggesting that only one of these indices is sufficient to characterize the LAA RTD function. The three representative subjects shown in Figure 2.5 are identified.

### 3.2.5 Relating LAA Mean Residence Time to LAA Appearance Complexity

Given that the calculation of LAA  $t_m$  is computationally expensive, we wanted to examine whether LAA appearance complexity, which is easier to calculate, can provide the same information as that provided by LAA  $t_m$ . The Spearman rank correlation analysis indicated that LAA  $t_m$  and LAA- $ACI$  are not correlated ( $\rho = 0.04$ ,  $P = 0.61$ ; **Figure 3.11**).

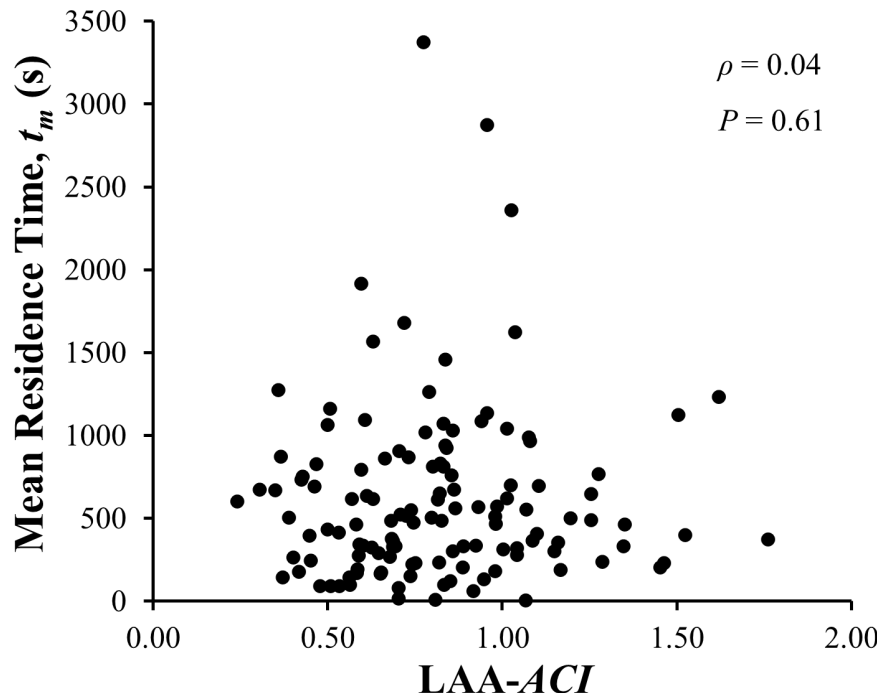


**Figure 3.11** Relationship between left atrial appendage (LAA) appearance complexity index (LAA-ACI) and LAA  $t_m$ .

The Spearman rank correlation analysis indicates a weak (although statistically significant) correlation, suggesting that these two variables do not provide the same information.

### 3.2.6 Relating LAA Mean Residence Time to CHA<sub>2</sub>DS<sub>2</sub>-VASc Score

Spearman rank correlation analysis was performed between LAA  $t_m$  and CHA<sub>2</sub>DS<sub>2</sub>-VASc score (**Figure 3.12**). LAA  $t_m$  was not correlated with CHA<sub>2</sub>DS<sub>2</sub>-VASc score ( $\rho = -0.09$ ,  $P = 0.33$ ; **Figure 3.12**).

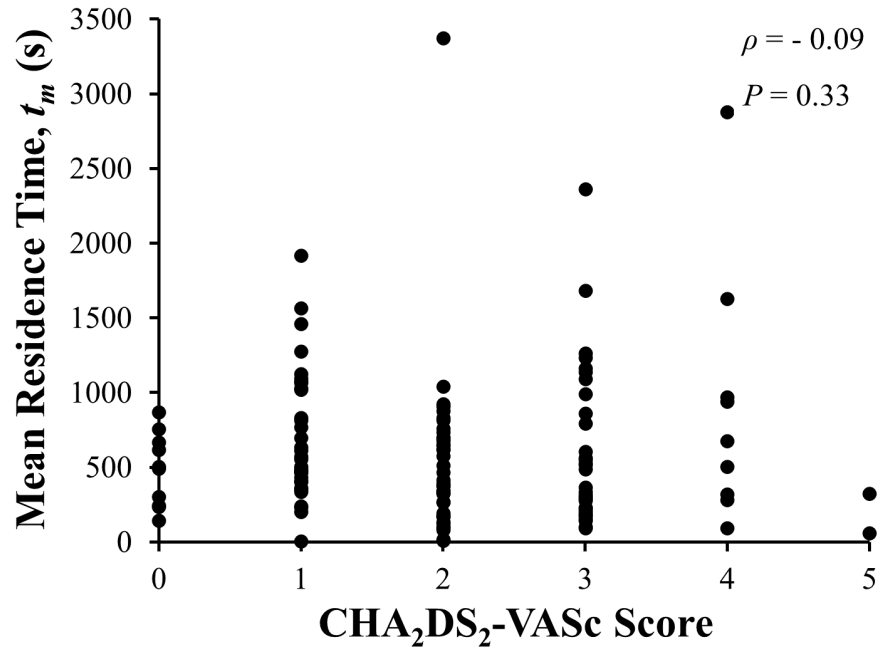


Figure 3.12 Relationship between left atrial appendage mean residence time, LAA  $t_m$ , and CHA<sub>2</sub>DS<sub>2</sub>-VASc score.

A weak and insignificant correlation was found between LAA  $t_m$ , and CHA<sub>2</sub>DS<sub>2</sub>-VASc score based on Spearman rank correlation analysis.

### 3.3 Discussion

Lingering of blood cells inside the LAA could result in an elevated risk of thrombus formation and, consequently, stroke. In the present study, we quantify the propensity of blood cell lingering within the LAA in terms of the RTD function,  $E(t)$ , and associated calculated variables (mean residence time of blood-borne particles in LAA, LAA  $t_m$ , and asymptotic concentration remaining inside LAA,  $C_\infty$ ). Both LAA and LA morphological features and spatially distributed hemodynamic milieu determine the LAA  $t_m$  and  $C_\infty$ . The key contributions of this chapter are as follows: 1) the development of a Eulerian and systems-based approach for quantifying the LAA

RTD function and associated calculated variable (LAA  $t_m$ ); 2) the validation of CFD simulation of a sample LA-LAA geometry using particle image velocimetry; 3) the Investigation of the confounding variables corresponding to LAA  $t_m$  and  $C_{\infty}$ ; 4) the observation that LAA- $ACI$  does not fully capture the information contained in LAA  $t_m$ ; and 5) the observation that the LAA  $t_m$  can add independent information to the CHA<sub>2</sub>DS<sub>2</sub>-VASc score and thereby potentially enhance its ability to stratify stroke risk in AF patients.

Several surrogates of thrombus-promoting flow patterns exist where they relate blood flow in LA and LAA to the probability of clot formation. These indices are mostly a direct derivation from flow velocity field (e.g., wall shear stress, time-averaged wall shear stress, oscillatory shear index, time-averaged velocity, local relative residence time, vortex structure, flow kinetic energy, and ECAP), whereas LAA RTD incorporates the transport of blood-borne particles, and it measures the propensity of blood cell lingering within the LAA by definition. Although the velocity field-based indices require only a short simulation time, we believe that LAA RTD has the capability to better simulate the transport and lingering of blood cells in LAA.

A systems-based approach was used to calculate  $E(t)$  in that it is the tracer washout response to an impulse injection of tracer in LAA. LAA  $E(t)$  curves are depicted in **Figure 3.9** for the same three subjects as in **Figure 2.5**. Subject #1 and subject #2 had higher starting point (i.e., value at  $t = 0$ ) compared to subject #3. However, the washout rate in subjects #1 and #2 decays in a faster pace than subject #3. The values in subjects #1 and #2 becomes lower only after ~20 s. These lower values are a consequence of the flow entering the LAA ostium that does not go all the way up to the LAA tip, resulting in a stagnant region at the tip. These data would predict that subject #2 has the highest risk of clot formation and subject #3 has the lowest risk.

We used the classification paradigm of Di Biase et al. (2012) to characterize LAA shape. This is a very subjective approach and even experienced cardiologists may not always agree when classifying a LAA into specific shape categories. In addition, there is a large variability in stroke occurrence within a given LAA shape category (Khurram et al., 2013, Nedios et al., 2014, Sanatkhani and Menon, 2017, Yaghi et al., 2018). This is consistent with the large variability of  $t_m$  (**Figure 3.9C**) and LAA- $ACI$  (**Figure 2.7**) within each shape category and in LAA values that exist even within a given LAA shape category (**Figure 3.9C**). The intercategory  $t_m$  (and LAA- $ACI$ ) variability may explain the differences in the stroke risk seen among subjects with similar overall LAA geometry. This variability underscores the importance of considering patient-specific LA and LAA morphologies in constructing a metric for stroke risk stratification in AF based on hemodynamics.

It has been suggested that under the AF flow condition, where the systolic and end-diastolic atrial reversal wave are diminished (Feng et al., 2021), the hemodynamic indices predict higher chance of thrombus formation compared to the healthy PV flow condition (Bosi et al., 2018). Further, several studies have shown that AF flow condition together with AF contraction patterns in LA and LAA would result in high risk of thrombus formation (Feng et al., 2021, Masci et al., 2020, Vella et al., 2021). However, Dueñas-Pamplona et al. (2021b) indicated that LA-LAA contractility is more important than PV flow and mitral boundary condition. Due to their nature, these types of investigations are heavily computationally expensive. Therefore, the aforementioned studies were done using an exceedingly small cohort. Further, the sensitivity of LAA  $t_m$  and  $C_\infty$  to PV flow waveform characteristics was not yet been examined. In the present study, using a cohort of 25 patient-specific LA-LAA geometries, the LAA blood stasis risk, as quantified by LAA  $t_m$  and  $C_\infty$ , was significantly affected by the mean value of inlet flow (i.e.,

cardiac output), but not by temporal pattern of the inlet flow. Therefore, the patient-specific LAA blood stasis risk can be reliably estimated using patient-specific LA and LAA 3D geometries and patient-specific cardiac output, without any need for patient-specific PV blood flow waveform.

Newtonian fluid assumption is a reasonable for modeling the blood flow inside the LA (Bosi et al., 2018, Dueñas-Pamplona et al., 2021a, Vella et al., 2021, Zhang and Gay, 2008), however, due to the existence stasis regions inside the LAA and significance reduction in shear strain rate, blood rheology might be an indicating factor in calculating LAA  $t_m$  and  $C_\infty$ . LAA  $t_m$  and  $C_\infty$  were affected significantly by hematocrit level and blood rheology (Newtonian vs. non-Newtonian) significantly in our study cohort. Even though LAA  $t_m$  and  $C_\infty$  varied as a function of blood rheology, choice of blood rheology model did not affect patients' LAA  $t_m$  and  $C_\infty$  rank order. Therefore, one might quantify the LAA  $t_m$  and  $C_\infty$  in a study cohort using Newtonian fluid model with viscosity corresponding to the hematocrit level. The computational cost of using a non-Newtonian blood rheology model (i.e., Quemada model) was negligible. Therefore, we will consider non-Newtonian model for our future simulation.

Based on our investigation on length of simulation as a confounding variable in quantifying LAA  $t_m$  and  $C_\infty$ , we believe that it is necessary to perform the fluid dynamics simulation for at least 10,000 s. As a result, simulations would take  $\sim 7$  days to complete (24 threads of dual 12 core Intel Xeon Gold 6126 CPU with 2.6 GHz clock speed and minimum of 8 GB of RAM). Further improvements of this model such as one-way and two-way fluid-wall interactions and multiscale analysis of biochemical coagulation cascade would significantly increase the computational cost. A method to reconstruct RTD has been introduced by Sierra-Pallares et al. (2017) that might be able to reduce the computational cost of LAA  $t_m$  and  $C_\infty$ , however, its accuracy has not been tested in LA-LAA geometries. In recent studies, deep neural network has been implemented to predict

CFD simulation results in LA-LAA geometries (Morales et al., 2020). This approach would decrease the computational cost significantly. However, a large number of CFD simulations are still needed to develop the ground truth for LAA  $t_m$  and  $C_\infty$  (and any other indices developed in the future).

We have shown that the LAA  $t_m$  and LAA- $ACI$  are weakly correlated (**Figure 3.11**). This suggests that LAA  $t_m$ , representing a holistic measure of subject-specific LA-LAA geometry features and hemodynamics, and LAA- $ACI$  have a potential to contribute independent information.

We found a weak and insignificant correlation between the LAA  $t_m$  and CHA<sub>2</sub>DS<sub>2</sub>-VASc score (**Figure 3.12**). In addition, LAA  $t_m$  varied significantly for a given CHA<sub>2</sub>DS<sub>2</sub>-VASc score (**Figure 3.12**). The mean residence time for patients with low CHA<sub>2</sub>DS<sub>2</sub>-VASc score of 0 and 1 ranges between 144–755 s and 6–1917 s, respectively (**Figure 3.12**). This would suggest that a patient with a low CHA<sub>2</sub>DS<sub>2</sub>-VASc score (= 0, 1) could still have a high risk of stroke. In contrast, patients with high CHA<sub>2</sub>DS<sub>2</sub>-VASc score of 5 in our cohort had relatively low values of LAA  $t_m$  (**Figure 3.12**); we would suggest that these subjects have a very low risk of stroke despite their high CHA<sub>2</sub>DS<sub>2</sub>-VASc scores. These observations suggest that the hemodynamics-based index (i.e., LAA  $t_m$ ) and appearance indices (i.e., LAA- $ACI$ ) can add independent information to the CHA<sub>2</sub>DS<sub>2</sub>-VASc score.

### 3.3.1 Limitations

For LA outlet boundary condition, the mitral valve was assumed to be open throughout the simulation, with both gauge pressure and velocity gradient set to zero. A better representation of LA outlet boundary condition would be in terms of left ventricular nonlinear diastolic compliance and patient-specific left ventricular end-diastolic or end-systolic volume. These left ventricular

diastolic compliance and volume data were not available for our cohort. A future study should be planned to conduct parametric studies to examine how left ventricular compliance and end-diastolic (or end-systolic) volume affect the calculated index, LAA  $t_m$ .

We used the assumption of rigid LA and LAA walls. It has been shown that LA-LAA wall contractility pattern in AF increases the risk of thrombus formation predicted by fluid dynamics indices and rigid wall simulation is inadequate in modeling such effects (Dueñas-Pamplona et al., 2021a, Dueñas-Pamplona et al., 2021b, Feng et al., 2021, García-Villalba et al., 2021, Masci et al., 2019, Otani et al., 2016, Qureshi et al., 2020, Vella et al., 2021, Zhang and Gay, 2008). To perform such analyses, for a simple model, 4D CT or 4D magnetic resonance imaging (MRI) of the study cohort is needed in order to impose the LA-LAA wall motion through the cardiac cycles. For a more sophisticated fluid-structure interaction models, myocardium muscle modelling and LA-LAA physiological wall properties are needed (Feng et al., 2021, Zhang and Gay, 2008). Parametric studies to examine the effects of LA-LAA wall properties and contraction patterns on LAA  $t_m$  and  $C_\infty$  in larger cohorts are needed.

Further, the effects of left ventricle were not considered in this study. The association of mitral regurgitation (MR) in AF to stroke is still controversial (Bisson et al., 2019). Modeling left ventricle attached to the LA will provide us the opportunity to study the effect of mitral valve function as well as MR on LAA  $t_m$  and  $C_\infty$  (Feng et al., 2021).

Finally, thrombus formation pathways or biochemical coagulation cascades were not coupled with our CFD model in this study. The findings of biological studies regarding thrombus formation pathways and mechanisms should be included in the CFD-based simulations. This will require multiscale simulations or could be done via simplifications within the macroscale CFD

simulations by defining some other combined hemodynamics- and thrombosis-related indices. Eventually, the embolus transport model to the brain would provide us the ultimate prediction.

#### **4.0 Specific Aim 3: Improve CHA<sub>2</sub>DS<sub>2</sub>-VASc-Based Stroke Risk Stratification Using LAA Appearance and LAA Residence Time Indices**

Our ultimate aim in this study was to determine whether LAA residence time and LAA appearance indices are able to independently improve stroke stratification in AF patients and consequently enhance clinical decision making. In this chapter we use the indices that were calculated in the previous chapters (i.e., LAA-*ACI*, LAA *t<sub>m</sub>*, and LAA *C<sub>∞</sub>*) to stratify the stroke risk.

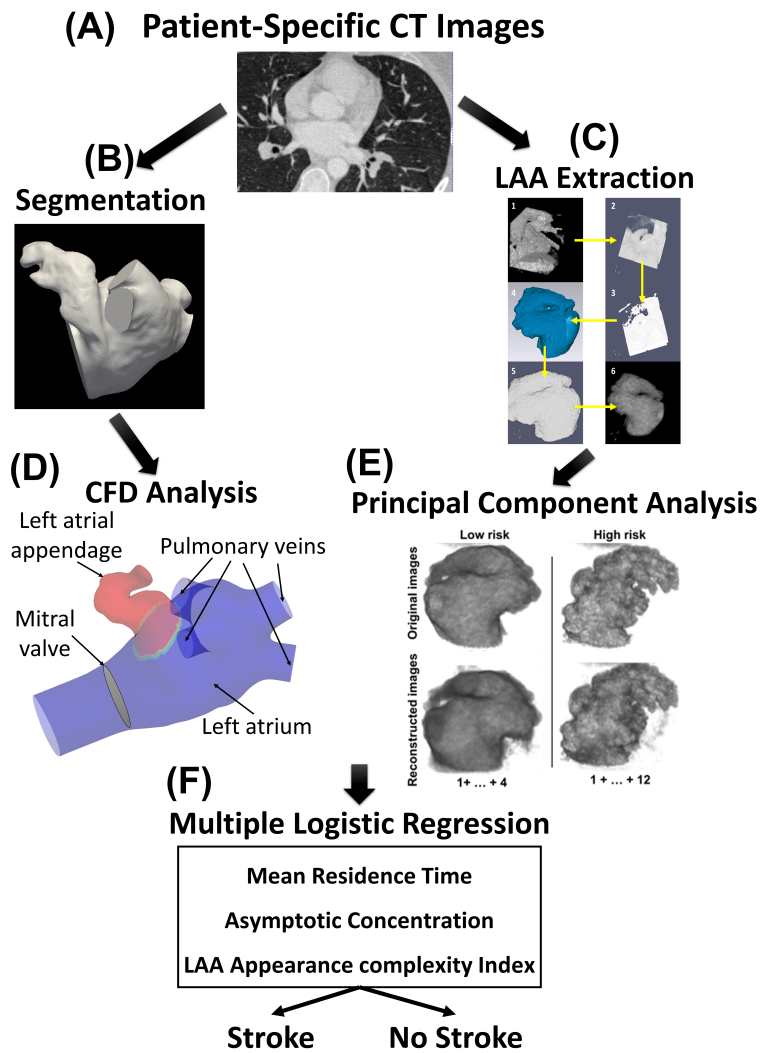


Figure 4.1 Schematic workflow of the overall study.

A) 128 Patient-Specific cardiac CT were used. B) Each patient-specific left atrium and left atrial appendage (LA-LAA) geometry was segmented and and prepared for CFD analysis. C) Library of patient-specific LAA images were created. D) CFD analysis were performed to calculated mean residence time and asymptotic concentration inside the LAA for each patient. E) Principal component analysis was performed using the library of LAA images to calculated LAA appearance complexity index of each LAA morphology. F) Indices generated in (D) and (E) were used as covariates of a multiple logistic regression model to predict stroke risk.

## 4.1 Methodology

The schematic workflow of this study is shown in **Figure 4.1**.

### 4.1.1 Study Design

This is a retrospective, matched case-control study. 50 AF patients who had prior history of stroke were enrolled, and patients without history of stroke were matched 2:1 according to left atrium (LA) size (within 0.1–0.2 cm), CHA<sub>2</sub>DS<sub>2</sub>-VASc score - 2, and AF type (i.e., persistent vs. paroxysmal). Patients included in this study were part of another study which goal is to establish a clinical database of patients undergoing evaluation and treatment of AF, including medical management and procedural based treatments (i.e., ablation, device-based therapies with pacemakers/defibrillators, and LAA closure devices) within the Heart and Vascular institute of University of Pittsburgh Medical Center (UPMC, Pittsburgh, PA, USA) hospitals.

### 4.1.2 Data Acquisition

Clinical data were provided in the registry data format. Cardiac-computed tomography (CCT) was performed in subjects prior to an AF catheter ablation procedure with the objective of delineating the anatomy of the left atrium and the pulmonary veins (PV) as well as ruling out the presence of a clot in the LAA. CCT images were obtained using a multi-slice 256 detector rows helical CT scanner (Revolution Apex, General Electric Medical System, LLC., Chicago, IL, USA). Scanning was performed gated to the cardiac cycle in cranio-caudal direction from the aortic arch towards the diaphragm. The imaging parameters were: 70–120–140 kV, 850 mA s, 0.6 mm beam

collimation, 0.625–1.25 mm thickness, and 20–30 cm field-of-view. Contrast medium was used to opacify LA-LAA structures as well as the PVs.

### 4.1.3 Statistical Analysis

Continuous variables are expressed as mean  $\pm$  standard deviation. Correlations between variables were determined by Spearman rank correlation. All statistical analyses were performed in SPSS software (IBM Corp. Released 2021. IBM SPSS Statistics for Windows, Version 28.0. Armonk, NY: IBM Corp).

Multiple logistic regression was performed to stratify the stroke risk. Our dependent variable was history of prior stroke (1 = yes; 0 = no). The probability of occurrence of stroke was related to 3 independent variables (i.e., LAA- $ACI$ , LAA  $t_m$ , and LAA  $C_\infty$ ) and their two-way interactions via **Eq. 4.1**:

$$\text{Probability}(\text{Stroke} = \text{Yes}|\mathbf{X}) = \frac{e^{(\beta_0 + \sum_i \beta_i X_i)}}{1 + e^{(\beta_0 + \sum_i \beta_i X_i)}} \quad \text{Eq. 4.1}$$

where  $\mathbf{X}$  is consisted of LAA- $ACI$ , LAA  $t_m$ , LAA  $C_\infty$ , and their two-way interactions. The coefficients,  $\beta_i$ , of the regression model were predicted by maximizing the log-likelihood for the 128 observations in SPSS.

## 4.2 Results

### 4.2.1 Patients Characteristics

Patients were kept in the study if the structure of LAA had sufficient visibility. A total of 128 patients with symptomatic AF (111 paroxysmal, 17 persistent) were studied (78 males) where 39 patients had history of prior stroke and 89 did not have prior stroke. The average age, heart rate, cardiac output, hematocrit level, and LA size were  $63.6 \pm 9.0$  years (range: 35–79 years), 66 bpm (range: 40–132 bpm),  $4.0 \text{ L min}^{-1}$  (range 1.5–8.7  $\text{L min}^{-1}$ ), 41.6% (range: 30.4%–53.6%), and 4.0 cm (range: 2.6–5.4 cm), respectively. The range of CHA<sub>2</sub>DS<sub>2</sub>-VASc scores was 0 to 5 (mean =  $2.0 \pm 1.1$ ).

### 4.2.2 Multiple Logistic Regression

We performed multiple logistic regression to develop a stroke risk prediction model using the three calculated hemodynamic and appearance indices (i.e., LAA-*ACI*, LAA *t<sub>m</sub>*, and LAA *C<sub>∞</sub>*), and their two-way interactions. Three separate multiple logistic regression analyses using three sets of covariates were performed: 1) Only LAA *t<sub>m</sub>*; 2) Only LAA-*ACI*; 3) All three calculated indices and their two-way interactions. Coefficients, significance values, and odds ratios for the model 4 parameters are presented in **Table 4.1**. Based on the Wald  $t^2$  value, *ACI*, *ACI*×*t<sub>m</sub>*, and *C<sub>∞</sub>*×*t<sub>m</sub>* individually contributed to the prediction the most.

**Table 4.1 Variables in the multiple logistic regression equation**

Covariates and their interactions used in logistic regression are presented with their coefficients ( $\beta_i$ ), standard error, Wald  $t^2$  value,  $P$  value, odds ratio, and confidence interval, respectively. None of the covariates were found significant.

	$\beta_i$	Standard Error	Wald $t^2$	$P$	$e^{\beta_i}$ (OR)	95% C.I. for $e^{\beta_i}$
$t_m$	-0.001	0.002	0.69	0.407	0.999	[0.995,1.002]
$C_\infty$	0.017	0.088	0.036	0.85	1.017	[0.855,1.209]
$ACI$	-3.368	1.553	4.703	0.03	0.034	[0.002,0.723]
$C_\infty \times t_m$	0	0	1.027	0.311	1	[1,1]
$ACI \times t_m$	0.003	0.002	2.414	0.12	1.003	[0.999,1.007]
$ACI \times C_\infty$	0.03	0.082	0.132	0.716	1.03	[0.878,1.209]
<b>Constant</b>	1.165	1.165	0.999	0.318	3.205	

Area under the curve (AUC) of receiver operating characteristic (ROC) curve of each model's prediction was calculated (**Figure 4.2**). Area under the ROC curve increased modestly by using either hemodynamic or appearance parameters (AUC (model 1) = 0.56; ACU (model 2) = 0.57) compared to the reference (i.e., random prediction). Further, adding the interactions between covariates further improved the prediction performance modestly (AUC (model 3) = 0.61). However, none of our results reached statistical significance. The sensitivity of prediction using model 3 was only 7.7%, and its specificity was 100% at a cutoff of 0.5 for probability of stroke. The model was able to only explain 8% (Nagelkerke  $R^2$ ) of the variance in occurrence of stroke and the overall model was not statistically significant ( $P = 0.31$ ).

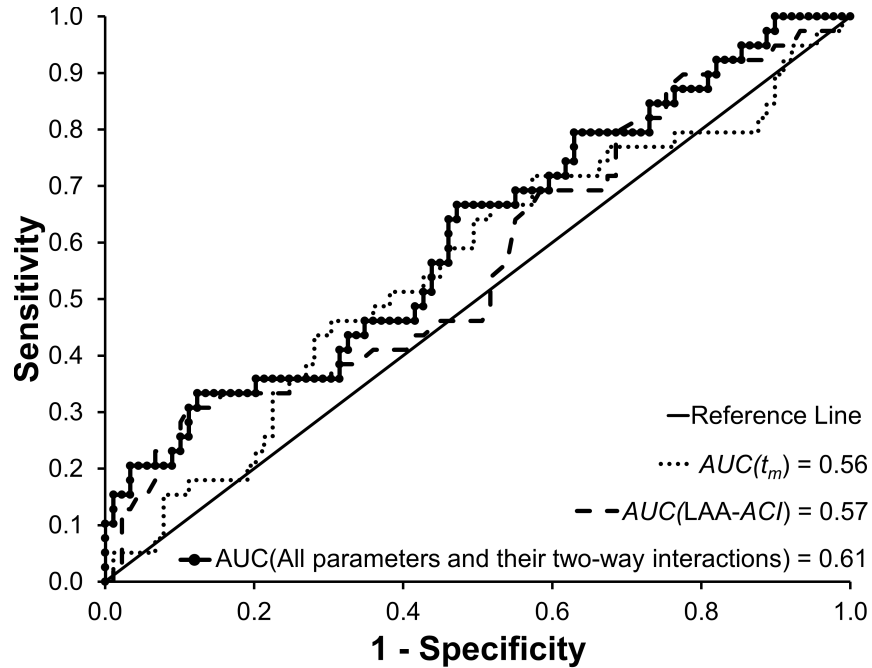


Figure 4.2 Receiver operating characteristic (ROC) curve for prediction of stroke

ROC curve for prediction of stroke based on three models is shown: 1) Only LAA  $t_m$ ; 2) Only LAA-ACI; 3) All three calculated indices and their two-way interactions. Area under the ROC curve (AUC) increased by adding hemodynamic and appearance parameters with respect to the random prediction. Further, adding the interactions between parameters improved the prediction performance (model 3).

### 4.3 Discussion

Extended linger of blood cells in the LAA (i.e., increased LAA  $t_m$ ), perpetually trapped blood cells within the LAA (i.e., increased  $C_\infty$ ), increased complexity of LAA morphology (i.e., increased LAA-ACI), and patient's clinical status (i.e., higher CHA<sub>2</sub>DS<sub>2</sub>-VASc score) can contribute to the elevated risk of stroke occurrence. Among these variables, CHA<sub>2</sub>DS<sub>2</sub>-VASc score is currently being used as a thromboembolism risk predictor, however, there is a large variability in CHA<sub>2</sub>DS<sub>2</sub>-VASc score among the patients with prior history of stroke and those without a prior

stroke, making it not ideal for stratifying stroke. CHA<sub>2</sub>DS<sub>2</sub>-VASc score is solely based on clinical variables and the patient-specific LA/LAA hemodynamics and morphology are not included in its calculation. In this study we hypothesized that patient-specific LA/LAA hemodynamics and morphology may add value to CHA<sub>2</sub>DS<sub>2</sub>-VASc score and therefore enhance the stroke prediction in AF. The LAA morphology was quantified via LAA-*ACI* in **Chapter 2** and the LA/LAA hemodynamics was quantified via LAA *t<sub>m</sub>* and *C<sub>∞</sub>* in **Chapter 3**. The focus of the present chapter is on examining whether LAA morphology and hemodynamics-based indices (i.e., *ACI*, *t<sub>m</sub>*, and *C<sub>∞</sub>*) can enhance stroke risk prediction in AF patients.

As discussed in the **Chapter 2**, many indices have been examined in this context of predicting stroke risk in AF patients, e.g., LAA orifice diameter; number of branches and twigs; degree of coverage with fine structure; LAA volume, depth, and number of lobes; and existence of a bend in LAA (Beinart et al., 2011, Di Biase et al., 2012, Ernst et al., 1995, Khurram et al., 2013, Nedioš et al., 2014). However, these are isolated features of the complex LAA geometry, and they do not represent the whole LAA morphology. A more insightful quantification of LAA morphology introduced by Wang et al. (2010), where they classified the LAA morphologies into four groups (i.e., ChickenWing, Windsock, Cauliflower, and Cactus). This quantification of LAA morphology was still based on measurements of isolated features. Further, this is a very subjective approach and even experienced cardiologists may not always agree when classifying a LAA into specific shape categories. In addition, there is a large variability in stroke occurrence within a given LAA shape category (Khurram et al., 2013, Nedioš et al., 2014, Yaghi et al., 2018). More recently, Bieging et al. (2021) assessed the LAA shape using PCA. They found three shape parameters to be predictive of stroke. Although, their quantitatively method showed a promising result in stratifying stroke risk, this method was based on reconstructed LAA surface geometry and

information regarding the channels inside the LAA was not considered. Further, due to the smoothing during surface reconstruction procedure, some detailed and complex features of LAA morphology was lost. In this study, the morphology of 128 patient's LAA were quantified using a novel index (i.e., *LAA-ACI*) in **Chapter 2**. *LAA-ACI* utilizes the entire 3D dataset, and we believe that this integrated index incorporates the information provided by all possible isolated measures and their interactions. However, the *LAA-ACI* only quantifies the LAA alone and does not incorporate the effect of LA morphology, the location of LAA with respect to LA, and the mechanics of blood flow inside the LA/LAA.

To factor in the missing aforementioned effects (i.e., location of LAA with respect to LA, and the mechanics of blood flow inside the LA/LAA), we simulated the 128 patient-specific LA/LAA geometries using patient-specific cardiac output and hematocrit and quantified their hemodynamics using residence time distribution function (**Chapter 3**). There are several studies in the literatures where various hemodynamic measures (i.e., wall shear stress, shear strain rate, time-averaged wall shear stress, oscillatory shear index (Koizumi et al., 2015), time-averaged velocity, mean resident time (Rayz et al., 2010), local residence time (Esmaily-Moghadam et al., 2013), residual virtual contrast agent (Bosi et al., 2018, Otani et al., 2016), and vortex structure) were used to quantify the LA/LAA hemodynamics. However, none of the studies were designed to actually stratify the stroke risk in AF patients (Boyle et al., 2021, García-Villalba et al., 2021, Masci et al., 2019, Masci et al., 2020, Morales et al., 2020, Morales et al., 2021, Otani et al., 2016, Zhang and Gay, 2008). We showed that both the hemodynamic indices (i.e.,  $t_m$ ,  $C_\infty$ ) and the morphology-based index (i.e., *LAA-ACI*) have the potential to add information to the CHA<sub>2</sub>DS<sub>2</sub>-VASc score.

Using multiple logistic regression, we observed that  $ACI$ ,  $t_m$ ,  $C_\infty$ , and their two-way interactions modestly predict stroke (AUC of the ROC curve = 0.58–0.66; **Figure 4.2**), suggesting that LAA morphology and hemodynamics-based indices modestly stratify stroke risk, independent of CHA<sub>2</sub>DS<sub>2</sub>-VASc score.

The insignificant results from the multiple logistic regression might be due to the temporal dissociation between the covariates and occurrence of stroke. We believe that changes in the covariates (i.e., LAA- $ACI$ , LAA  $t_m$ , or LAA  $C_\infty$ ) precede the actual stroke event. Therefore, it is possible that there are patients currently in the No Stroke group whose covariates have already changed; these subjects are highly likely to have the stroke event in the future. Only a longitudinal study can address this issue definitively. However, to get some preliminary insight, the first (bottom 25%) and third (top 25%) quartile of each covariate alone or two covariates together were examined closely with respect the stroke status (**Table 4.2**). For each covariate and combination of covariates, percentages (absolute numbers) of patients in the Stroke and No Stroke groups corresponding to top 25% and bottom 25% are presented in **Table 4.2**. The overall stroke status in our population was as follows: ~30% patients with stroke and ~70% without stroke. We expect that percentage of the stroke patients should be higher than 30% in top 25% group and it should be lower than 30% in the bottom 25% group. Although LAA  $t_m$  showed this expected pattern of change in the percentage of stroke patients, this was a modest change (7%) (**Table 4.2**). In contrast, when the top 25% and bottom 25% separation was done based on both hemodynamic indices (i.e., LAA  $t_m$  and LAA  $C_\infty$ ), there was a stronger evidence in support of the expected change (**Table 4.2**): the top 25% group had 70% patients with stroke (OR = 2.7; CI = [0.5,14.5]). However, this result did not reach statistical significance because of the low numbers of patients in the bottom and top 25% group (**Table 4.2**). We strongly believe that a longitudinal study of AF subjects in

the top 25% of LAA  $t_m$  and LAA  $C_\infty$  is needed to definitely address whether these two changes are predictive of future stroke.

**Table 4.2 Population and percentage of top 25% and bottom 25% of each variable with respect to the history of prior stroke**

Population of each group is shown in parentheses. Each row presents two sets of information. The column for Top 25% represents the subjects that their corresponding variable is among the top 25%. The percentage (or population) of those subjects that had prior stroke (or did not have stroke) are presented in the specified sub-columns. The column of Bottom 25% represents the same information but for the subjects whom their corresponding variable is among the bottom 25%. The last four rows include the subjects which two of their variables are among the top 25% (or bottom 25 %) at the same time. Odds ratio (exposure: top 25%, no exposure: bottom 25%) and its corresponding confidence interval are presented in last two columns for each variable.

Variables	Top 25%		Bottom 25%		OR	CI
	Stroke	No Stroke	Stroke	No Stroke		
$t_m$	37% (12)	63% (20)	28% (9)	72% (23)	1.5	[0.5,4.4]
$ACI$	22% (7)	78% (25)	41% (13)	59% (19)	0.4	[0.1,1.2]
$C_\infty$	31% (10)	69% (22)	28% (9)	72% (23)	1.2	[0.4,3.4]
$t_m$ & $C_\infty$	70% (7)	30% (3)	47% (7)	53% (8)	2.7	[0.5,14.5]
$t_m$ & $ACI$	67% (2)	33% (1)	83% (5)	17% (1)	0.4	[0.0,10.0]
$C_\infty$ & $ACI$	25% (3)	75% (9)	45% (5)	55% (6)	0.4	[0.1,2.3]

### 4.3.1 Limitations

Limitations specific to LAA appearance quantification and LA/LAA hemodynamic quantification are presented in **Chapter 2** and **Chapter 3**, respectively. Our results regarding the

stroke risk prediction in AF patients using our predictive model were negative. There maybe two underlying reasons:

First, although our results indicate that LAA  $t_m$ ,  $C_\infty$ , and  $ACI$  improve stroke risk stratification power of CHA<sub>2</sub>DS<sub>2</sub>-VASc score, results were not statistically significance. A longitudinal study with a larger number of subjects will be needed to examine whether these indices can indeed enhance stroke prediction independent of CHA<sub>2</sub>DS<sub>2</sub>-VASc score. Further, the CCT imaging used for the stroke group of this study were acquired after the occurrence of stroke. Collecting the clinical data and imaging data prior to occurrence of stroke would eliminate the possibility of clinical, geometrical parameter changes after a stroke.

Second, in this study we quantified the LA-LAA hemodynamics using scalar concentration residence time distribution. Scalar concentration used in this study was representative of neutrally buoyant blood cell moving though LA and LAA. Coupling a biological simulation (Ye et al., 2020, Zheng et al., 2020), specifically designed for LAA wherein thrombus formation pathways are considered, with the current methodology would enhance the hemodynamic quantification of LA-LAA and consequently improve the stroke risk stratification model.

## 5.0 Summary and Future Directions

### 5.1 Summary

AF is the most common arrhythmia and is a major cause of mortality and morbidity. The most dangerous complication is thromboembolic stroke for which AF is an independent risk factor. Every AF patient is initially evaluated for thromboembolic risk (**Section 1.4**), with a re-evaluation performed at each stage of management. Anticoagulation therapy is one of the most important parts of clinical management in AF. Stroke risk stratification is essential when making decisions about anticoagulation therapy or LAA closure. Accurate stroke stratification is critical to improve the patient selection decision for LAA exclusion/occlusion and increase the effectiveness of anticoagulant management while lowering the side effects. The most commonly used and validated risk stratification scheme for making clinical decisions regarding the anticoagulant or antiplatelet therapy for the management of AF patients is CHA<sub>2</sub>DS<sub>2</sub>-VASc scheme where everyone has a score with range of 0 to 9 (**Table 1.1**). According to the CHA<sub>2</sub>DS<sub>2</sub>-VASc scheme, a score of 0 is considered insignificant risk, a score of 1 is considered moderate, and  $\geq 2$  is considered elevated risk. It is recommended that patients who receive score of  $\geq 2$  to be treated with anticoagulation therapy. However, while 91% and 50% of thrombi in nonvalvular AF and valvular AF, respectively, are found in LAA (Al-Saady et al., 1999, Holmes et al., 2009, Reddy et al., 2013) CHA<sub>2</sub>DS<sub>2</sub>-VASc does not incorporate the role of LA/LAA geometry or local hemodynamics in the thromboembolic risk assessment. Presently, we are very limited in predicting who will have a stroke in the context of AF and quantification of LA/LAA hemodynamics and morphology could add value to CHA<sub>2</sub>DS<sub>2</sub>-VASc scheme and consequently enhance stroke risk stratification.

In the present study, we quantified LAA morphology in terms of the LAA appearance complexity index (LAA-*ACI*) that was calculated using the PCA. In addition, we quantified LA/LAA hemodynamics via fluid dynamics simulations by calculating scalar concentration mean residence time, LAA  $t_m$ , and asymptotic concentration,  $C_\infty$ , inside the LAA. The ultimate goal was **to determine whether LAA residence time and LAA appearance indices are able to significantly improve stroke stratification in AF patients and consequently enhance clinical decision making.**

Patient-specific LAA CCT images were quantified using a PCA-based analysis where LAA morphology complexity was represented by LAA-*ACI*. We found an insignificant negative correlation between the LAA-*ACI* and CHA<sub>2</sub>DS<sub>2</sub>-VASc score (**Figure 2.8**), indicating that these two indices are not conveying the same information. There is a large variability of appearance complexity index for a given CHA<sub>2</sub>DS<sub>2</sub>-VASc score. This underscores the possibility that LAA-*ACI* has a potential to add information independent of the CHA<sub>2</sub>DS<sub>2</sub>-VASc score and consequently, improving the current stroke risk stratification protocol that is solely based on the CHA<sub>2</sub>DS<sub>2</sub>-VASc score.

Next, we employed CFD to calculate mean residence time of blood-borne particles in the LAA ( $t_m$ ), an index of LAA blood stasis, using 3D LA and LAA geometries and LA inlet blood flow (i.e., pulmonary vein flow) data. Effects of confounding variables including pulsatility of PV flow waveform, hematocrit level and non-Newtonian fluid model, and length of simulation were investigated. According to our investigations, LAA blood stasis risk, as quantified by LAA  $t_m$  and  $C_\infty$ , is significantly affected by the mean value of inlet flow (i.e., cardiac output), but not by temporal pattern of the inlet flow. Therefore, the patient-specific LAA blood stasis risk can be reliably estimated using patient-specific LA and LAA 3D geometries and patient-specific cardiac

output, without any need for patient-specific PV blood flow waveform. We showed that patient-specific hematocrit is also an important factor and should be considered as one of the input variables in our simulations. Further, we concluded that at least 10,000 s of tracer concentration transport simulation is needed to calculate LAA  $t_m$  reliably and consistently. Results of our investigations regarding the confounding variables were used to adjust our CFD -based simulation methodology for calculating LAA  $t_m$  and  $C_\infty$ . Patient-specific LA/LAA CCT images from 128 AF patients were reconstructed to generate surface bodies and prepared for CFD simulation. Patient-specific cardiac outputs and hematocrit levels were used to simulate tracer concentration washout from LAA where blood was modeled as a non-Newtonian fluid based on Quemada model. LAA  $t_m$  and  $C_\infty$  were calculated based on 10,000 s of simulation for each patient. We found a weak and insignificant correlation between the LAA  $t_m$  and CHA<sub>2</sub>DS<sub>2</sub>-VASc score (**Figure 3.12**) suggesting that hemodynamics-based indices (i.e., LAA  $t_m$  and  $C_\infty$ ) could add independent information to the CHA<sub>2</sub>DS<sub>2</sub>-VASc score.

Using multiple logistic regression, we demonstrated that LA/LAA hemodynamics and LAA appearance quantifications could modestly enhance the prediction of stroke occurrence. Specifically,  $ACI$ ,  $t_m$  and  $C_\infty$  increased the area under the ROC curve compared to the reference line (random prediction), indicating that the shape and hemodynamics quantification adds positive value to stroke stratification independent of CHA<sub>2</sub>DS<sub>2</sub>-VASc score, LA size, and AF type. However, our results did not reach statistical significance. There may be three underlying reasons for the negative result (i.e., statistically insignificant enhancement of the stroke risk prediction in AF patients). First, we believe that adverse changes in LAA shape and hemodynamics-based indices precede the actual stroke event. Clearly, this temporal dissociation can contribute to the negative result; a longitudinal study is necessary to address this issue. Second, we have not

incorporated the biology of thrombus formation in our CFD model-based simulations. It is possible that a multiscale model that combines CFD-based hemodynamics simulation and biology-based thrombus formation can yield indices that can better stratify stroke risk in AF patients. Third, given that the differences in AF management, including the anticoagulation treatment, can affect the biological end point (stroke), future studies should include this as a confounding variable.

## **5.2 Future Directions**

Future efforts should be directed in two directions: 1) improving the current CFD-based predictive model, and 2) improving the study design.

### **5.2.1 Improving the Current CFD-Based Predictive Model**

The current CFD-based predictive model can be improved in several ways: (1) patient-specific compliant LA/LAA walls, (2) incorporation of blood thrombosis biology, and (3) machine learning to accelerate the CFD-based simulations.

#### **5.2.1.1 Patient-Specific Compliant LA/LAA Walls**

Due to significant complexity and computational costs of modeling patient-specific compliant LA/LAA wall for 10,000 s, we considered this to be out of scope of this dissertation. However, studies have shown that emptying velocity of LAA is associated with risk of clot formation inside the LAA (Petersen et al., 2014). Emptying velocity is highly correlated with movement and contraction of LAA, therefore, it is beneficial to include the LA/LAA wall

movement in future studies. Further, we are currently using a simple boundary condition at the outlet (i.e., mitral valve) where a constant gauge pressure of zero is set (representative of atrial systole). A compliant LA wall enables us to consider more sophisticated boundary condition to represent opening and closing of mitral valve.

### **5.2.1.2 Incorporation of Blood Thrombosis Biology**

Several clinical factors are known to increase the risk of thromboembolic events. However, the mechanisms of thrombus formation in AF are still not fully known. Studies have suggested that AF confers a hypercoagulable state, resulting in increase in risk of thromboembolism and stroke (Feng et al., 2001, Lip, 1997). Several factors have been indicated to be associated with left atrial thromboembolism such as LAA velocity, von Willebrand factor, and beta-thromboglobulin (Heppell et al., 1997). There are multiple mechanisms that lead to thrombus formation in AF. These mechanisms are complex and closely interact with each other which adds up to the complications in these studies. However, for an ideal predictive model to stratify stroke risk in AF, the fundamental mechanisms must be known and included in the hemodynamic model.

To develop an ideal stroke prediction model in AF, the findings of biological studies regarding thrombus formation pathways and mechanisms should be included in the CFD-based simulations. This will require multiscale simulations or could be done via simplifications within the macroscale CFD simulations by defining some other combined hemodynamics- and thrombosis-related indices.

### **5.2.1.3 Machine Learning to Accelerate the CFD-Based Simulations**

In recent studies, deep neural network has been implemented to predict CFD simulation results in LA/LAA geometries (Morales et al., 2020, Morales et al., 2021). This approach would

decrease the computational cost significantly. However, a large number of CFD simulations are still needed to develop the ground truth for LAA  $t_m$ , and  $C_\infty$  (and any other indices developed in the future).

### 5.2.2 Improving the Study Design

We strongly believe that there is a temporal dissociation between the changes in the covariates and the occurrence of stroke – covariate changes precede the actual stroke event. Thus, we hypothesize that this temporal dissociation is a confounding variable for the analysis of data obtained in a cross-sectional study. A longitudinal study of AF subjects is necessary to test our hypothesis and evaluate the performance of our CFD-based simulations to stratify stroke risk. Such a study would require several years of data collection. Contrast enhanced CCT images must be acquired from each AF subject prior to any occurrence of stroke to eliminate the possibility of geometrical changes due to stroke.

Unlike, the LAA morphology that remains relatively unchanged throughout the life, LA-LAA hemodynamics of a patient can change significantly over time, which, in turn, can affect the calculated indices (i.e., LAA  $t_m$ , and  $C_\infty$ ). Our CFD simulations for calculating LAA  $t_m$ , and  $C_\infty$  utilized patient-specific hemodynamic measurements obtained at one time point. It is probably better to obtain longitudinal hemodynamics measurements and calculate corresponding LAA  $t_m$ , and  $C_\infty$  values. This temporal pattern of changes in LAA  $t_m$ , and  $C_\infty$  may be more predictive of the stroke risk than the prediction based on a single time point.

Furthermore, in the present study, we focused on predicting the stroke. Changing the prediction goal to an earlier and local event, such as the existence of a clot inside the LAA, could improve our prediction performance.

## Appendix A LAA-ACI Calculation

As explained in **Section 2.1.2**, a MATLAB code is used to separate LAA from the rest of LA using a mask volume surrounding the LAA (**Appendix A.1**). This program takes two inputs: 1) A volume image in VTK (Visualization Toolkit) format enclosing LAA and the vasculature around it, 2) A volume image tightly enclosing the LAA morphology where all voxels have intensity of 10. The output is LAA 3D image with original intensities and surrounding vasculatures removed. Next, a MATLAB code was used to reshape 3D LAA images into a 1D vector (**Appendix A.2**). Finally, a MATLAB code (**Appendix A.3**) was used to perform PCA (**Section 2.1.3**). The input for this program is a matrix of  $1,000,000 \times 128$  consisting of 1D vectors of 128 LAA images generated in Appendix A.2. The output of this program is the calculated total sum of squares, *TSS*, and residual sum of squares root, *RSSR* (**Section 2.1.4**).

### Appendix A.1 Masking

```
close all;
clear;
clc;

ID = '%% Patient ID %%';

InputVTKfile = strcat(ID, '_1_LAA.vtk');
MaskVTKfile = strcat(ID, '_2_Mask.vtk');
MaskedVTKfile = strcat(ID, '_3_Masked.vtk');

MaskedVTK = vtk_mask_volume(InputVTKfile, MaskVTKfile);
MaskedVTK.Origin = [0 0 0];
disp('Writing VTK volume ...');
```

```

write_vtk_Volume(MaskedVTK.array, MaskedVTK.Spacing,
MaskedVTK.Origin, MaskedVTKfile);

disp('Done!');

function MaskedVTK = vtk_mask_volume(InputVTKfile, MaskVTKfile)
    disp('Reading original VTK header ...');
    InputVTKinfo = vtk_read_header(InputVTKfile);
    disp('Reading original volume ...');
    InputVTK = vtk_read_volume(InputVTKinfo);

    disp('Reading mask VTK header ...');
    MaskVTKinfo = vtk_read_header(MaskVTKfile);
    disp('Reading mask volume ...');
    MaskVTK = vtk_read_volume(MaskVTKinfo);

    disp('Reading done!');

    Xc =
InputVTKinfo.Origin(1):InputVTKinfo.PixelDimensions(1):InputVTKi
nfo.Origin(1)+InputVTKinfo.PixelDimensions(1)*InputVTKinfo.Dimen
sions(1)-InputVTKinfo.PixelDimensions(1);
    Yc =
InputVTKinfo.Origin(2):InputVTKinfo.PixelDimensions(2):InputVTKi
nfo.Origin(2)+InputVTKinfo.PixelDimensions(2)*InputVTKinfo.Dimen
sions(2)-InputVTKinfo.PixelDimensions(2);
    Zc =
InputVTKinfo.Origin(3):InputVTKinfo.PixelDimensions(3):InputVTKi
nfo.Origin(3)+InputVTKinfo.PixelDimensions(3)*InputVTKinfo.Dimen
sions(3)-InputVTKinfo.PixelDimensions(3);

    [Xcr,Ycr,Zcr] = ndgrid(Xc,Yc,Zc);
    S_CroppedVTK = single(InputVTK);
    CroppedMesh = S_CroppedVTK;

    Xv =
MaskVTKinfo.Origin(1):MaskVTKinfo.PixelDimensions(1):MaskVTKinfo
.Origin(1)+MaskVTKinfo.PixelDimensions(1)*MaskVTKinfo.Dimensions
(1)-MaskVTKinfo.PixelDimensions(1);
    Yv =
MaskVTKinfo.Origin(2):MaskVTKinfo.PixelDimensions(2):MaskVTKinfo
.Origin(2)+MaskVTKinfo.PixelDimensions(2)*MaskVTKinfo.Dimensions
(2)-MaskVTKinfo.PixelDimensions(2);
    Zv =
MaskVTKinfo.Origin(3):MaskVTKinfo.PixelDimensions(3):MaskVTKinfo
.Origin(3)+MaskVTKinfo.PixelDimensions(3)*MaskVTKinfo.Dimensions
(3)-MaskVTKinfo.PixelDimensions(3);

```

```

[Xvo, Yvo, Zvo] = ndgrid(Xv, Yv, Zv);
MaskMesh =
interp(Xvo, Yvo, Zvo, MaskVTK, Xcr, Ycr, Zcr, 'cubic', 0);

disp('Matrix Multiplication ...');
MaskedVTK.array = (MaskMesh.*CroppedMesh)./10;
MaskedVTK.Spacing = [InputVTKinfo.PixelDimensions(1)
InputVTKinfo.PixelDimensions(2)
InputVTKinfo.PixelDimensions(3)];
MaskedVTK.Origin = [InputVTKinfo.Origin(1)
InputVTKinfo.Origin(2) InputVTKinfo.Origin(3)];
end

%%%%%%%%%%%%%%%%%%%%%%%%%%%%%%%%%%%%%%%%%%%%%%%%%%%%%%%%%%%%%%%%%%%%%%%%
function info = vtk_read_header(filename)
% Function for reading the header of a Visualization Toolkit
% (VTK)
%
% info = vtk_read_header(filename);
%
% examples:
% 1, info=vtk_read_header()
% 2, info=vtk_read_header('volume.vtk');

if(exist('filename', 'var')==0)
    [filename, pathname] = uigetfile('*.vtk', 'Read vtk-file');
    filename = [pathname filename];
end

fid=fopen(filename, 'rb');
if(fid<0)
    fprintf('could not open file %s\n', filename);
    return
end

str = fgetl(fid);
info.FileName=filename;
info.Format=str(3:5); % Must be VTK
info.Version=str(end-2:end);
info.Header = fgetl(fid);
info.DatasetFormat= lower(fgetl(fid));
str = lower(fgetl(fid));
info.DatasetType = str(9:end);

readscalars=false;

```

```

while(~readscalars)
    str=fgetl(fid);
    s=find(str==' ',1,'first');
    if(~isempty(s))
        type=str(1:s-1); data=str(s+1:end);
    else
        type=''; data=str;
    end

    switch(lower(type))
        case 'dimensions'
            info.Dimensions=sscanf(data, '%d')';
        case 'point_data'
            info.NumberOfComponents = sscanf(data, '%d');
        case 'spacing'
            info.PixelDimensions=sscanf(data, '%lf')';
        case 'origin'
            info.Origin=sscanf(data, '%lf')';
        case 'color_scalars'
            readscalars=true;
            s=find(data==' ',1,'first');
            info.DataName=data(1:s-1);
            info.NumberOfComponents=sscanf(data(s+1:end), '%d');
            if ( info.NumberOfComponents == 1)
                info.PixelType='scalar';
            else
                info.PixelType='vector';
            end
            if(info.DatasetFormat(1)=='a')
                info.DataType='float';
            else
                info.DataType='uchar';
            end
        case 'scalars'
            readscalars=true;
            s=find(data==' ');
            info.DataName=data(1:s(1)-1);

            if ( length(s) > 1)
                info.DataType=data(s(1)+1:s(2)-1);

            info.NumberOfComponents=sscanf(data(s(2)+1:end), '%d');
            else
                info.DataType=data(s(1)+1:end);
            end
    end
end
end

```

```

switch(info.DataType)
    case 'char', info.BitDepth=8;
    case 'uchar', info.BitDepth=8;
    case 'short', info.BitDepth=16;
    case 'ushort', info.BitDepth=16;
    case 'int', info.BitDepth=32;
    case 'uint', info.BitDepth=32;
    case 'float', info.BitDepth=32;
    case 'double', info.BitDepth=64;
    otherwise, info.BitDepth=0;
end

b=ftell(fid);
str=fgetl(fid);
s=find(str==' ',1,'first');
type=str(1:s-1); data=str(s+1:end);
switch(lower(type))
    case 'lookup_table'
        info.TableName=data;
    otherwise
        fseek(fid,b,'bof');
end
info.HeaderSize=ftell(fid);
fclose(fid);
end

%%%%%%%%%%%%%%%%%%%%%%%%%%%%%%%%%%%%%%%%%%%%%%%%%%%%%%%%%%%%%%%%%%%%%%%%%%%%%%
%%%%%%%%%%%%%%%%%%%%%%%%%%%%%%%%%%%%%%%%%%%%%%%%%%%%%%%%%%%%%%%%%%%%%%%%%%%%%%
function V = vtk_read_volume(info)
if(~isstruct(info)), info=vtk_read_header(info); end
% Open file
fid=fopen(info.Filename,'rb','ieee-be');
% Skip header
fseek(fid,info.HeaderSize,'bof');

datasize=prod(info.Dimensions)*info.BitDepth/8;
% datasize=prod(info.Dimensions)*16;
% V= uint16(fread(fid,datasize,'ushort'));
% V = single(fread(fid,datasize,'float'));
% Read the Data
switch(lower(info.DatasetFormat(1)))
    case 'b'
        switch(info.DataType)
            case 'char'
                V = int8(fread(fid,datasize,'char'));

```

```

        case 'uchar'
            V = uint8(fread(fid,datasize,'uchar'));
        case 'short'
            V = int16(fread(fid,datasize,'short'));
        case 'ushort'
            V = uint16(fread(fid,datasize,'ushort'));
        case 'int'
            V = int32(fread(fid,datasize,'int'));
        case 'uint'
            V = uint32(fread(fid,datasize,'uint'));
        case 'float'
            V = single(fread(fid,datasize,'float'));
        case 'double'
            V = double(fread(fid,datasize,'double'));
    end
case 'a'
    t=prod(info.Dimensions);
    switch(info.DataType)
        case 'char', type='int8';
        case 'uchar', type='uint8';
        case 'short', type='int16';
        case 'ushort', type='uint16';
        case 'int', type='int32';
        case 'uint', type='uint32';
        case 'float', type='single';
        case 'double', type='double';
        otherwise, type='double';
    end
    V=zeros([1 t],type);
    for i=1:t, V(i)=str2double(fgetl(fid)); end
end

disp(info.Dimensions);
disp(length(V));
fclose(fid);
V = reshape(V,info.Dimensions);
end
function write_vtk_Volume(array, Spacing, Origin, filename)
    [nx, ny, nz] = size(array);
    fid = fopen(filename, 'wt');
    fprintf(fid, '# vtk DataFile Version 2.0\n');
    fprintf(fid, 'Comment goes here\n');
    fprintf(fid, 'ASCII\n');
    fprintf(fid, '\n');
    fprintf(fid, 'DATASET STRUCTURED_POINTS\n');
    fprintf(fid, 'DIMENSIONS      %d      %d      %d\n', nx, ny, nz);
    fprintf(fid, '\n');

```

```

    fprintf(fid, 'ORIGIN    %d    %d    %d\n', Origin(1),
Origin(2), Origin(3));
    fprintf(fid, 'SPACING    %d    %d    %d \n',
Spacing(1), Spacing(2), Spacing(3));
    fprintf(fid, '\n');
    fprintf(fid, 'POINT_DATA    %d\n', nx*ny*nz);
    fprintf(fid, 'SCALARS scalars double\n');
    fprintf(fid, 'LOOKUP_TABLE default\n');
    fprintf(fid, '\n');
    for a=1:nz
        for b=1:ny
            for c=1:nx
                fprintf(fid, '%d ', array(c,b,a));
            end
            fprintf(fid, '\n');
        end
    end
    fclose(fid);
return
end

```

## Appendix A.2 Reshaping 3D Images into Vectors

```

close all;
clc;
clear;

folders = ls;
VTK2DMatrix = zeros(10000,100,128);
VTKVector = zeros(1000000,128);
count = 0;

for i = 3:1:130
    [CaseNo] = strread(folders(i,:), '%s', 'emptyvalue', NaN);
    PatientsList(i-2,1) = str2num(strtrim(CaseNo (Abecasis et
al., 2009)));
    fprintf('%d\n', PatientsList(i-2,1));
    count = count + 1;

    VTKfile = sprintf('%d%s', PatientsList(i-2,1), '.vtk');
    info = vtk_read_header(sprintf('%s%d%s%s', '%% Directory
Path %%%', PatientsList(i-2,1), '\', VTKfile));

```

```

VTK3DMatrix = vtk_read_volume(info);

for ii = 1:1:100
    for jj = 1:1:100
        for kk = 1:1:100
            VTKVector(((ii-1).*10000)+((jj-
1).*100)+kk,count) = VTK3DMatrix(kk,jj,ii);
        end
    end
end
end
LAA_vectorized = VTKVector;

```

### Appendix A.3 Principal Component Analysis

```

close all;
clear;
clc;
load LAA_vectorized.mat;

Obs = 1;          %Case ID
p = 1000000;     %Total number of parameters (total number of
voxels)
p_k = 128;       %Number of parameters to keep (total = n)
n = 128;         %Number of cases
LAA = LAA_vectorized';
TS = zeros(n,1);

faces_normalized = zeros(n,p);
faces_centered = zeros(n,p);
for i = 1:n
    faces_normalized(i,:) = (LAA(i,:) -
min(LAA(i,:)))/(max(LAA(i,:))-min(LAA(i,:)));
    faces_centered(i,:) = faces_normalized(i,:) -
mean(faces_normalized(i,:));
    for ii = 1:p
        TS(i,1) = TS(i,1) + faces_centered(i,p).^2;
    end
end
end

D_eu = zeros(p_k,n);

```

```

for Obs = 1:n
    Obs
    for k = 1:p_k
        COEFF =
pca(faces_centered', 'Economy', false, 'Centered', false, 'Algorithm'
, 'eig');
        RowFeatureVector = COEFF(:,1:k)';
        RowDataAdjust = faces_centered;
        FinalData = RowFeatureVector*RowDataAdjust;

        RowFeatureVectorT = RowFeatureVector';
        NewRowDataAdjust = RowFeatureVectorT*FinalData;

        for i = 1:p
            D_eu(k,Obs) = D_eu(k,Obs) + (NewRowDataAdjust(Obs,i)
- faces_centered(Obs,i)).^2;
        end

        D_eu(k,Obs) = sqrt(D_eu(k,Obs));
    end
end
RSSR = D_eu';

```

## Appendix B OpenFOAM

Several OpenFOAM solvers and boundary conditions were developed for this dissertation based on original OpenFOAM codes. To investigate the effects of patient-specific PV flow waveform, we developed the *ScalarAdvection* solver which is based on original *icoFoam* solver of OpenFOAM. In this solver transport equation is coupled with the momentum equations (**Appendix B.1**). To investigate the effects of patient-specific hematocrit levels and non-Newtonian vs. Newtonian fluid modeling, we developed *nonNewtonianDistVel* (**Appendix B.2**), *icoFoamDistVel* (**Appendix B.3**), and *passiveScalarAdvection* (**Appendix B.4**) solvers which are based on original *nonNewtonianIcoFoam*, *icoFoam*, and *ScalarTransportFoam* solvers of OpenFOAM, respectively. In our final simulations, *nonNewtonianDistVel* and *passiveScalarAdvection* solvers were used.

### Appendix B.1 ScalarAdvection

This solver is consisted of a main function defined in *ScalarAdvection.C* and a boundary condition for PV inlets, *DistributedVelocityInlet*. Continuity equation, momentum equations and transport equations are solved in *ScalarAdvection.C*. A PISO loop is being used to solve momentum equations. Transport equation is being solved at each time step after pressure and velocity calculation in PISO loop. Further, PV flow is read from a CSV file at each time step and velocity at PV inlets is calculated based on the total surface area of PV inlets. *ScalarAdvection.C* is presented below:

```

////////////////////////////////////
// * * * * * ScalarAdvection.C * * * * * //
////////////////////////////////////
#include "fvCFD.H"
#include "pisoControl.H"
#include "scalarIOList.H"
#include "DistributedVelocityInlet.C"
#include "DistributedVelocityInletFvPatchVectorField.H"

////////// For CSV Reader //////////
#include <fstream>
#include <iostream>
#include <sstream>
#include <string>
#include <vector>

// * * * * * //

int main(int argc, char *argv[])
{
    #include "setRootCaseLists.H"
    #include "createTime.H"
    #include "createMesh.H"

    pisoControl piso(mesh);

    #include "createVelocityInlet.H"
    #include "createFields.H"
    #include "initContinuityErrs.H"

    //////////////////////////////////////
    std::vector<std::vector<std::vector<double>>> FlowRate;
    for (int i = 0; i<1; i++)
    {
        std::ifstream in(TotalFlowRateFile);
        std::vector<std::vector<double>> FlowRate2;
        if (in)
        {
            std::string line;
            while (getline(in, line))
            {
                std::stringstream sep(line);
                std::string flowrate;
                FlowRate2.push_back(std::vector<double>());
                while (getline(sep, flowrate, ','))
                {

```

```

FlowRate2.back().push_back(stod(flowrate));
}
}
}
FlowRate.push_back(FlowRate2);
}

Calculate_TotalArea(mesh);

////////////////////////////////////

Info<< "\nStarting time loop\n" << endl;

int d = int(round(1000*runTime.value())) % FlowRate[0].size();

UniformVelocity[0] = (FlowRate[0][d][1]/60000)/TotalArea;

while (runTime.loop())
{
    Info<< "Time = " << runTime.timeName() << nl << endl;

    #include "CourantNo.H"

    // Momentum predictor

    fvVectorMatrix UEqn
    (
        fvm::ddt(U)
        + fvm::div(phi, U)
        - fvm::laplacian(nu, U)
    );

    if (piso.momentumPredictor())
    {
        solve(UEqn == -fvc::grad(p));
    }

    // --- PISO loop
    while (piso.correct())
    {
        volScalarField rAU(1.0/UEqn.A());
        volVectorField HbyA(constrainHbyA(rAU*UEqn.H(), U, p));
        surfaceScalarField phiHbyA
        (
            "phiHbyA",
            fvc::flux(HbyA)

```

```

    + fvc::interpolate(rAU)*fvc::ddtCorr(U, phi)
);

adjustPhi(phiHbyA, U, p);

// Update the pressure BCs to ensure flux consistency
constrainPressure(p, U, phiHbyA, rAU);

// Non-orthogonal pressure corrector loop
while (piso.correctNonOrthogonal())
{
    // Pressure corrector

    fvScalarMatrix pEqn
    (
        fvm::laplacian(rAU, p) == fvc::div(phiHbyA)
    );

    pEqn.setReference(pRefCell, pRefValue);

    pEqn.solve();

    if (piso.finalNonOrthogonalIter())
    {
        phi = phiHbyA - pEqn.flux();
    }

    U = HbyA - rAU*fvc::grad(p);
    U.correctBoundaryConditions();
}

solve(fvm::ddt(s) + fvm::div(phi,s));

#include "continuityErrs.H"

runTime.write();

Info<< "ExecutionTime = " << runTime.elapsedCpuTime() << " s"
    << " ClockTime = " << runTime.elapsedClockTime() << " s"
    << nl << endl;
}

Info<< "End\n" << endl;

return 0;

```





```

////////////////////////////////////
// * * * * * createVelocityInlet.H * * * * * //
////////////////////////////////////
IOdictionary VelocityInletProperties
(
    IObject
    (
        "VelocityInletProperties",
        runTime.constant(),
        mesh,
        IOobject::MUST_READ_IF_MODIFIED,
        IOobject::NO_WRITE
    )
);

const wordList titleNames(VelocityInletProperties.toc());

forAll(titleNames, item)
{
    const word& titleName = titleNames[item];
    const dictionary& subDict =
VelocityInletProperties.subDict(titleName);
}

Info<< "Reading scalar list UniformVelocity \n" << endl;
scalarIOList UniformVelocity
(
    IObject
    (
        "UniformVelocity",
        runTime.timeName(),
        mesh
    ),
    1
);
/*Initialising the storage array*/
for (int i = 0; i <1; i++)
{
    UniformVelocity[i] = 0;
}
/* Initialise the VelocityInlet Properties*/
initialiseVel(VelocityInletProperties);

// * * * * * //
////////////////////////////////////

```

The total PV inlets surface area needed for *UniformVelocity* calculation is computed in DistributedVelocityInlet.C:

```

////////////////////////////////////
// * * * * * DistributedVelocityInlet.C * * * * * //
////////////////////////////////////
double TotalArea;
std::string TotalFlowRateFile;

void initialiseVel(const dictionary& VelocityInletProperties)
{
    /* Initialising */

    const wordList titleNames(VelocityInletProperties.toc());

    forAll(titleNames, item)
    {
        const word& titleName = titleNames[item];

        const dictionary& subDict =
        VelocityInletProperties.subDict(titleName);

        TotalFlowRateFile = string(subDict.lookup("TotalFlowRateFile"));
    }
}

void Calculate_TotalArea(fvMesh & mesh)
{
    label pv1 = mesh.boundaryMesh().findPatchID("pv1");
    label pv2 = mesh.boundaryMesh().findPatchID("pv2");
    label pv3 = mesh.boundaryMesh().findPatchID("pv3");
    label pv4 = mesh.boundaryMesh().findPatchID("pv4");
    TotalArea =gSum(mesh.magSf().boundaryField()[pv1])
    +gSum(mesh.magSf().boundaryField()[pv2])
    +gSum(mesh.magSf().boundaryField()[pv3])
    +gSum(mesh.magSf().boundaryField()[pv4]);
}

// * * * * * //
////////////////////////////////////

```

Velocity vector field normal to each individual PV inlet is calculated in DistributedVelocityInletFvPatchVectorField.C:

```
////////////////////////////////////
// * * * * * DistributedVelocityInletFvPatchVectorField.C * * * * * //
////////////////////////////////////
```

```
#include "DistributedVelocityInletFvPatchVectorField.H"
#include "volFields.H"
#include "addToRunTimeSelectionTable.H"
#include "fvPatchFieldMapper.H"
#include "surfaceFields.H"
#include "mathematicalConstants.H"
#include "vectorField.H"
#include "fvc.H"
#include "scalarIOList.H"
```

```
// * * * * * Constructors * * * * * //
```

```
Foam::DistributedVelocityInletFvPatchVectorField::
DistributedVelocityInletFvPatchVectorField
(
    const fvPatch& p,
    const DimensionedField<vector, volMesh>& iF
)
:
    fixedValueFvPatchField<vector>(p, iF)
    (Abecasis et al., 2009)
```

```
Foam::DistributedVelocityInletFvPatchVectorField::
DistributedVelocityInletFvPatchVectorField
(
    const fvPatch& p,
    const DimensionedField<vector, volMesh>& iF,
    const dictionary& dict
)
:
    fixedValueFvPatchField<vector>(p, iF, dict)
{}
```

```
Foam::DistributedVelocityInletFvPatchVectorField::
DistributedVelocityInletFvPatchVectorField
(
    const DistributedVelocityInletFvPatchVectorField& ptf,
    const fvPatch& p,
    const DimensionedField<vector, volMesh>& iF,
    const fvPatchFieldMapper& mapper
)
:
```

```

        fixedValueFvPatchField<vector>(ptf, p, iF, mapper)
    {}

Foam::DistributedVelocityInletFvPatchVectorField::
DistributedVelocityInletFvPatchVectorField
(const DistributedVelocityInletFvPatchVectorField& ptf):
    fixedValueFvPatchField<vector>(ptf)
{}

Foam::DistributedVelocityInletFvPatchVectorField::
DistributedVelocityInletFvPatchVectorField
(
    const DistributedVelocityInletFvPatchVectorField& ptf,
    const DimensionedField<vector, volMesh>& iF
)
:
    fixedValueFvPatchField<vector>(ptf, iF)
{}
// * * * * * ** * * * Member Functions * * * * * * * * * * * * * * //

void Foam::DistributedVelocityInletFvPatchVectorField::updateCoeffs()
{
    if (updated())
    {
        return;
    }
    /* Accessing the variables stored in mesh */
    const fvMesh& mesh = patch().boundaryMesh().mesh();
    const scalarIOList& UniformVelocity =
mesh.lookupObject<scalarIOList>("UniformVelocity");

    const scalar U = UniformVelocity[0];
operator==(-U*patch().nf());

    fixedValueFvPatchField<vector>::updateCoeffs();
}

void Foam::DistributedVelocityInletFvPatchVectorField::write(Ostream&
os) const
{
    fvPatchVectorField::write(os);
    writeEntry(os, "value", *this);
}
namespace Foam
{
    makePatchTypeField

```



```

// flowRateInletVelocityFvPatchVectorField
// onto a new patch
DistributedVelocityInletFvPatchVectorField
(
    const DistributedVelocityInletFvPatchVectorField&,
    const fvPatch&,
    const DimensionedField<vector, volMesh>&,
    const fvPatchFieldMapper&
);

//- Construct as copy
DistributedVelocityInletFvPatchVectorField
(
    const DistributedVelocityInletFvPatchVectorField&
);

//- Construct and return a clone
virtual tmp<fvPatchVectorField> clone() const
{
    return tmp<fvPatchVectorField>
    (
        new DistributedVelocityInletFvPatchVectorField(*this)
    );
}

//- Construct as copy setting internal field reference
DistributedVelocityInletFvPatchVectorField
(
    const DistributedVelocityInletFvPatchVectorField&,
    const DimensionedField<vector, volMesh>&
);

//- Construct and return a clone setting internal field
reference
virtual tmp<fvPatchVectorField> clone
(
    const DimensionedField<vector, volMesh>& iF
) const
{
    return tmp<fvPatchVectorField>
    (
        new DistributedVelocityInletFvPatchVectorField(*this,
iF)
    );
}
// Member functions

```

```

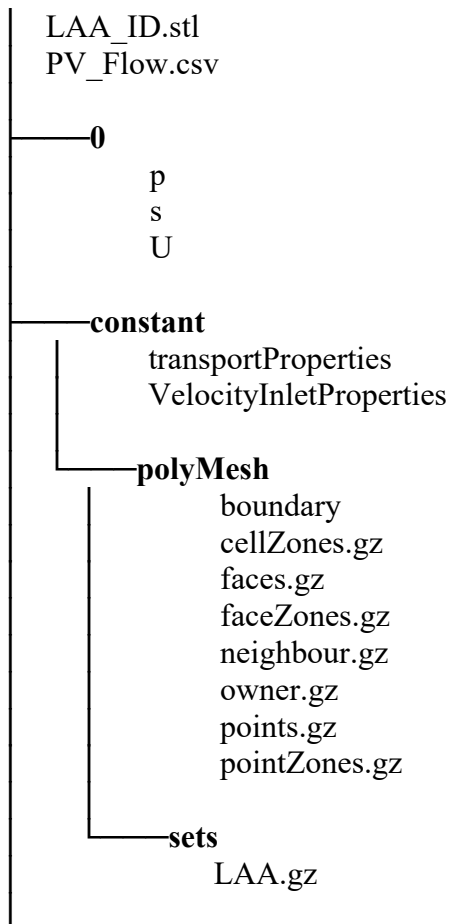
        //- Update the coefficients associated with the patch field
        virtual void updateCoeffs();

        //- Write
        virtual void write(Ostream&) const;
};
} // End namespace Foam
#endif
// * * * * *
////////////////////////////////////

```

### Appendix B.1.1 Sample Simulation Setup Using *ScalarAdvection* Solver

Directory structure for setup of a sample subject simulation using *ScalarAdvection* is presented below:









using *passiveScalarAdvection* solver. The simulation setup for *nonNewtonianDistVel* solver is similar to *ScalarAdvection* solver. However, transport equation is not solved in this solver. Therefore, all associated parts to transport equation are omitted. Instead, the hematocrit levels, plasma viscosity, and maximum allows viscosity for blood need to be set in transportProperties file. *nonNewtonianDistVel* solver is consisted of createFields.H, createVelocityInlet.H, DistributedVelocityInlet.C, DistributedVelocityInletFvPatchVectorField.C, DistributedVelocityInletFvPatchVectorField.H, nonNewtonianDistVel.C, Quemada.C, and Quemada.H.

```

////////////////////////////////////
// * * * * * createFields.H * * * * * //
////////////////////////////////////
Info<< "Reading field p\n" << endl;
volScalarField p
(
    IOobject
    (
        "p",
        runtime.timeName(),
        mesh,
        IOobject::MUST_READ,
        IOobject::AUTO_WRITE
    ),
    mesh
);

Info<< "Reading field U\n" << endl;
volVectorField U
(
    IOobject
    (
        "U",
        runtime.timeName(),
        mesh,
        IOobject::MUST_READ,
        IOobject::AUTO_WRITE
    ),
    mesh
);

```



```

fluid.correct();

// Momentum predictor

fvVectorMatrix UEqn
(
    fvm::ddt(U)
  + fvm::div(phi, U)
  - fvm::laplacian(fluid.nu(), U)
  - (fvc::grad(U) & fvc::grad(fluid.nu()))
);

if (piso.momentumPredictor())
{
    solve(UEqn == -fvc::grad(p));
}

// --- PISO loop
while (piso.correct())
{
    volScalarField rAU(1.0/UEqn.A());
    volVectorField HbyA(constrainHbyA(rAU*UEqn.H(), U, p));
    surfaceScalarField phiHbyA
    (
        "phiHbyA",
        fvc::flux(HbyA)
      + fvc::interpolate(rAU)*fvc::ddtCorr(U, phi)
    );

    adjustPhi(phiHbyA, U, p);

    // Update the pressure BCs to ensure flux consistency
    constrainPressure(p, U, phiHbyA, rAU);

    // Non-orthogonal pressure corrector loop
    while (piso.correctNonOrthogonal())
    {
        // Pressure corrector

        fvScalarMatrix pEqn
        (
            fvm::laplacian(rAU, p) == fvc::div(phiHbyA)
        );

        pEqn.setReference(pRefCell, pRefValue);
    }
}

```



```

        dictionary
    );
}
}
// * * * * * Private Member Functions * * * * * //
Foam::tmp<Foam::volScalarField>
Foam::viscosityModels::Quemada::calcNu() const
{
return min(
nuMax_,
nuP_*pow(1.0-0.5*
((exp(3.874 - 10.41*H_ + 13.8*H_*H_ - 6.738*H_*H_*H_)
+exp(1.3435 - 2.803*H_ + 2.711*H_*H_ - 0.6479*H_*H_*H_)
*sqrt((dimensionedScalar(dimTime, 1.0)*strainRate())/exp(-6.1508 +
27.923*H_ - 25.6*H_*H_ + 3.697*H_*H_*H_)))
/(1.0+sqrt((dimensionedScalar(dimTime, 1.0)*strainRate())/exp(-6.1508
+ 27.923*H_ - 25.6*H_*H_ + 3.697*H_*H_*H_))))
*H_
,-2));
}
// * * * * * Constructors * * * * * //
Foam::viscosityModels::Quemada::Quemada
(
    const word& name,
    const dictionary& viscosityProperties,
    const volVectorField& U,
    const surfaceScalarField& phi
)
:
    viscosityModel(name, viscosityProperties, U, phi),
    QuemadaCoeffs_
    (
        viscosityProperties.optionalSubDict(typeName + "Coeffs")
    ),
    nuP_("nuP", dimViscosity, QuemadaCoeffs_),
    nuMax_("nuMax", dimViscosity, QuemadaCoeffs_),
    H_("H", dimless, QuemadaCoeffs_),
    nu_
    (
        IOobject
        (
            name,
            U_.time().timeName(),
            U_.db(),
            IOobject::NO_READ,
            IOobject::AUTO_WRITE

```

```

        ),
        calcNu()
    )
}
// * * * * * Member Functions * * * * * //
bool Foam::viscosityModels::Quemada::read
(
    const dictionary& viscosityProperties
)
{
    viscosityModel::read(viscosityProperties);

    QuemadaCoeffs_ =
        viscosityProperties.optionalSubDict(typeName + "Coeffs");

    QuemadaCoeffs_.lookup("nuP") >> nuP_;
    QuemadaCoeffs_.lookup("nuMax") >> nuMax_;
    QuemadaCoeffs_.lookup("H") >> H_;

    return true;
}
// * * * * * //
////////////////////////////////////
////////////////////////////////////
////////////////////////////////////
// * * * * * Quemada.H * * * * * //
////////////////////////////////////
////////////////////////////////////
#ifndef Quemada_H
#define Quemada_H

#include "viscosityModel.H"
#include "dimensionedScalar.H"
#include "volFields.H"

// * * * * * //
* * * //

namespace Foam
{
namespace viscosityModels
{

/*-----*\
                Class Quemada Declaration
\*-----*/

class Quemada:

```

```

public viscosityModel
{
    // Private Data

    dictionary QuemadaCoeffs_;

    dimensionedScalar nuP_;
    dimensionedScalar nuMax_;
    dimensionedScalar H_;

    volScalarField nu_;

    // Private Member Functions
    //- Calculate and return the laminar viscosity
    tmp<volScalarField> calcNu() const;

public:
    //- Runtime type information
    TypeName("Quemada");

    // Constructors
    //- Construct from components
    Quemada
    (
        const word& name,
        const dictionary& viscosityProperties,
        const volVectorField& U,
        const surfaceScalarField& phi
    );
    //- Destructor
    virtual ~Quemada()
    {}

    // Member Functions
    //- Return the laminar viscosity
    virtual tmp<volScalarField> nu() const
    {
        return nu_;
    }
    //- Return the laminar viscosity for patch
    virtual tmp<scalarField> nu(const label patchi) const
    {
        return nu_.boundaryField()[patchi];
    }

    //- Correct the laminar viscosity

```









## Appendix C Curve fitting, Mean Residence Time, Asymptotic Concentration

The computational fluid dynamics model yields LAA tracer concentration,  $C(t)$ , every 1 s over the entire simulation period  $t = 0-10,000$  s (**Figure 3.9A**). The  $C(t)$  decay curve seems to have multiple time constants and a non-zero asymptotic value (**Figure 3.9A**). Accordingly, a triple exponential model with non-zero asymptote was used to characterize the  $C(t)$  curve:

$$C(t) = a_1 e^{-b_1 t} + a_2 e^{-b_2 t} + a_3 e^{-b_3 t} + C_\infty \quad \text{Eq. A1}$$

where  $a_1$ ,  $a_2$ ,  $a_3$ ,  $b_1$ ,  $b_2$ , and  $b_3$  are the parameters to be estimated by fitting the triple exponential model (**Eq. A1**) to the calculated  $C(t)$  data. Given that  $C(t = 0) = 1$ ,  $C_\infty = 1 - a_1 - a_2 - a_3$ .

The dynamics of the tracer clearance from LAA was quantified in terms of the RTD function,  $E(t)$  (Fogler, 2016):

$$\text{RTD Function: } E(t) = \frac{M(t)}{M_{total}} \quad \text{Eq. A2}$$

where  $M(t)$  is the outflow of tracer material (amount of tracer material per unit time) from LAA at the LAA ostium and  $M_{total}$  is the total amount of tracer that will leave the LAA over the period 0 to infinity.  $M(t)$  can be written in terms of  $C(t)$  using the finite difference approximation:

$$M(t) = \frac{[C(t) - C(t + \Delta t)] V_{LAA}}{\Delta t} \quad \text{Eq. A3}$$

where  $\Delta t$  and  $V_{LAA}$  are the time increment used in the finite difference-based estimation of  $M(t)$  and the LAA volume, respectively.

Given that  $C(t = 0) = 1$  and  $C(t \rightarrow \infty) = C_\infty$ ,  $M_{total}$  is given by:

$$M_{total} = (1 - C_\infty) V_{LAA} \quad \text{Eq. A4}$$

Substituting **Eq. A3** and **Eq. A4** in **Eq. A2**, we get:

$$E(t) = \frac{[C(t) - C(t + \Delta t)]}{\Delta t (1 - C_\infty)} \quad \text{Eq. A5}$$

$E(t)\Delta t$  is the fraction of fluid exiting the LAA that has spent between time  $t$  and  $t + \Delta t$  inside the LAA. Thus, the LAA mean residence time,  $t_m$ , is given by the first moment of  $E(t)$ :

$$t_m = \int_0^{\infty} tE(t)dt = \frac{1}{\Delta t(1-c_{\infty})} \int_0^{\infty} [tC(t) - tC(t + \Delta t)]dt \quad \text{Eq. A6}$$

It should be noted that since  $C(t)$  is comprised of exponentially decaying terms,  $\int_0^{\infty} tC(t)dt$  is finite and the result can be written in terms of an analytical expression. For example,  $\int_0^{\infty} te^{-at}dt = a^{-2}$ . Finally, writing the **Eq. A6** in the differential form, we get:

$$t_m = \frac{1}{1-c_{\infty}} \left( \frac{a_1}{b_1} + \frac{a_2}{b_2} + \frac{a_3}{b_3} \right) \quad \text{Eq. A7}$$

A custom program was developed in the MATLAB® (version R2020b, MathWorks, Inc., Natick, MA, USA) environment to estimate the six parameters ( $a_1$ ,  $a_2$ ,  $a_3$ ,  $b_1$ ,  $b_2$ , and  $b_3$ ) using a nonlinear iterative optimization algorithm and perform subsequent data processing to calculate LAA mean residence time,  $t_m$ .

## Appendix C.1 MATLAB Code for Curve Fitting

```
%Reading Data
clc
clear
close all
format long

numTimePoints = 10001;
lastTimepoint = 10000;
Scalar = zeros(numTimePoints,1);
fileID = fopen('volFieldValue.dat');
Data = textscan(fileID, '%f %s', 'emptyvalue', NaN,
'headerlines', 4);
fclose(fileID);
SamplingRate = 1;
for i = 1:numTimePoints
    Scalar(i,1) = str2double(Data{2}{i});
```

```

end
fileID2 = fopen('volFieldValue.dat');
Data2 = textscan(fileID2, '%s %s %s %s', 'emptyvalue', NaN,
'headerlines', 2);
fclose(fileID2);
LAA_Volume = str2double(Data2{4}{1});

% Assign time (time) and measured concentration (C) arrays and #
of points (np)
time=(0:SamplingRate:lastTimepoint).';
C = Scalar/LAA_Volume;

time = time(time<=10000);
C = C(time<=10000);
% %%%%%%%%%%%
[xData, yData] = prepareCurveData( time, C );
ft = fittype(' (a1/%%A1_norm%%)*exp(-
(b1/%%B1_norm%%)*x)+(a2/%%A2_norm%%)*exp(-
(b2/%%B2_norm%%)*x)+(a3/%%A3_norm%%)*exp(-
(b3/%%B3_norm%%)*x)+(1-(a1/%%A1_norm%%)-(a2/%%A2_norm%%)-
(a3/%%A3_norm%%))', 'independent', 'x', 'dependent', 'y');
opts = fitoptions( 'Method', 'NonlinearLeastSquares' );
opts.Algorithm = 'Trust-Region';
opts.DiffMinChange = 1e-8;
opts.DiffMaxChange = 0.1;
opts.MaxFunEvals = 600;
opts.MaxIter = 400;
opts.Robust = 'LAR';
opts.StartPoint = [%%Computed using MATLAB Curve Fitting Tool%%];
opts.Lower = [0 0 0 0 0 0];
opts.upper = [Inf Inf Inf Inf Inf Inf];

% Fit model to data.
[fitresult, gof] = fit( xData, yData, ft, opts );
CI = confint(fitresult);
a1 = (fitresult.a1)/A1_norm;
a2 = (fitresult.a2)/A2_norm;
a3 = (fitresult.a3)/A3_norm;
b1 = (fitresult.b1)/B1_norm;
b2 = (fitresult.b2)/B2_norm;
b3 = (fitresult.b3)/B3_norm;

Cinf = 1-a1-a2-a3;
tm = (a1./b1+a2./b2+a3./b3)./(1.0-Cinf);

a(1) = a1;
a(2) = a2;

```

```
a(3) = a3;
b(1) = b1;
b(2) = b2;
b(3) = b3;
[sortedb, ib] = sort([1./b1 1./b2 1./b3]);
Results = [tm Cinf.*100 1./(b(ib(1))) 1./(b(ib(2)))
1./(b(ib(3))) a(ib(1)) a(ib(2)) a(ib(3))];
fprintf("tm = %.0f\nCinf = %.1f\ntau1 = %.0f\ntau2 = %.0f\ntau3
= %.0f\na1 = %.2f\na2 = %.2f\na3 = %.2f\n",Results(:));
```

## Appendix D Raw Data

### Appendix D.1 Clinical Data

Appendix Table 2 Clinical Data

CO: Cardiac Output; HR: Heart Rate; AF Type: 1 (paroxysmal), 2 (persistent), 3 (permanent); SV: Stroke Volume; LVEDD: Left ventricle end diastolic diameter; LVESD: Left ventricle end systolic diameter.

	CO	HR	Hct	Prior Stroke	CHA <sub>2</sub> DS <sub>2</sub> -VASc	Age	Gender	AF Type	SV (ml)	LVEDD (cm)	LVESD (cm)
1	2.8	66	49.3	1	2	69	M	1	41.8	3.8	2.4
2	3.6	78	39.7	1	3	62	F	1	46.4	4.2	2.9
3	4.7	78	43.3	1	1	55	F	1	60.2	4.5	2.9
4	3.9	84	37.8	1	2	62	F	1	46.4	4.2	2.9
5	2.3	55	38.6	1	3	68	F	1	41.6	4.5	3.5
6	3.4	54	39.1	1	2	68	F	2	62.3	4.6	3.0
7	3.8	46	38.9	1	2	71	M	1	83.3	4.9	2.8
8	2.6	51	35.0	1	4	78	F	1	51.5	4.7	3.5
9	7.2	99	46.2	1	1	61	M	2	72.9	5.1	3.5
10	2.3	64	35.8	1	3	54	M	1	35.4	4.6	3.8
11	2.6	58	39.9	1	3	57	M	1	45.0	4.5	3.4
12	1.8	40	41.3	1	0	49	M	2	44.2	4.7	3.7
13	5.6	59	42.4	1	0	68	M	1	94.5	5.2	3.0
14	2.7	67	37.4	1	4	75	F	1	40.0	3.7	2.3
15	3.7	68	46.4	1	3	66	M	1	54.0	4.2	2.6
16	4.6	76	44.2	1	3	71	F	1	60.2	4.5	2.9
17	3.7	56	48.5	1	3	68	M	1	65.3	5.3	4.0
18	2.8	79	42.7	1	2	65	M	1	35.6	4.3	3.4
19	5.5	84	38.6	1	2	61	M	2	65.7	5.1	3.7
20	4.1	69	42.9	1	1	59	F	1	60.1	4.8	3.4
21	2.9	49	40.1	1	1	61	F	1	58.4	4.9	3.6
22	3.1	85	41.2	1	3	69	F	1	36.3	4.1	3.1
23	3.2	69	43.4	1	2	69	M	1	46.5	4.6	3.5
24	1.6	43	46.2	1	1	74	M	1	36.3	4.1	3.1
25	5.9	61	42.4	1	1	56	M	1	96.9	6.0	4.3
26	4.7	70	37.6	1	3	62	F	1	67.4	5.0	3.5
27	4.9	100	36.8	1	3	69	F	1	49.0	4.2	2.8
28	3.5	49	40.3	1	1	60	M	1	72.4	5.7	4.4

*Appendix Table 2 (continued)*

29	3.2	61	38.5	1	2	69	F	1	51.9	4.1	2.5
30	3.2	56	46.7	1	2	68	M	1	56.3	5.0	3.8
31	3.6	73	42.9	1	3	75	F	1	49.6	4.1	2.6
32	4.3	70	35.5	1	1	35	F	1	61.4	4.7	3.2
33	2.9	41	41.0	1	4	79	M	1	71.9	4.9	3.2
34	2.4	55	44.6	1	4	56	M	1	44.0	5.4	4.6
35	2.3	48	43.1	1	2	78	M	1	48.2	5.0	4.0
36	3.6	91	36.1	1	2	47	F	1	39.2	4.1	3.0
37	4.8	73	41.2	1	2	68	M	1	65.1	4.6	2.9
38	3.0	52	45.8	1	2	63	M	1	57.4	4.5	3.0
39	3.3	67	44.1	1	5	76	F	1	49.6	4.1	2.6
40	3.8	59	42.5	0	3	58	M	1	64.4	4.7	3.1
41	1.9	52	39.3	0	2	64	F	1	36.8	4.4	3.5
42	5.3	60	42.5	0	3	70	F	1	87.6	6.0	4.5
43	7.2	80	40.1	0	3	73	M	1	90.4	5.4	3.5
44	6.8	46	38.2	0	3	71	M	1	148.6	5.9	2.6
45	6.8	62	44.3	0	1	44	M	1	109.3	5.2	2.4
46	5.0	58	37.5	0	1	41	M	2	85.5	5.5	3.8
47	2.4	52	42.7	0	2	66	M	1	46.4	4.2	2.9
48	3.9	64	45.9	0	2	70	M	1	61.4	4.7	3.2
49	6.9	62	44.0	0	1	69	M	1	111.4	5.2	2.3
50	6.0	64	36.0	0	1	50	F	1	94.1	5.7	3.9
51	3.3	47	43.6	0	2	57	F	1	69.4	5.3	3.9
52	6.7	74	41.9	0	2	68	M	1	90.0	5.7	4.0
53	2.4	63	44.3	0	2	56	M	2	37.9	5.9	5.3
54	2.1	53	41.2	0	2	70	M	1	39.2	4.1	3.0
55	2.8	48	43.8	0	1	58	M	1	57.7	5.7	4.7
56	4.8	59	45.4	0	2	65	M	1	80.6	4.9	2.9
57	2.9	53	38.8	0	3	70	F	1	54.5	4.5	3.1
58	4.9	49	43.1	0	1	58	M	1	99.2	5.1	2.6
59	4.9	62	41.9	0	3	68	F	1	78.6	5.2	3.5
60	4.2	52	43.8	0	2	54	M	1	80.9	5.3	3.6
61	7.8	111	40.0	0	3	67	F	1	70.1	4.5	2.5
62	5.8	121	36.5	0	5	67	F	1	47.7	5.3	4.4
63	1.9	50	45.1	0	2	75	M	1	38.9	3.9	2.7
64	2.5	53	46.6	0	1	67	M	1	47.2	4.1	2.7
65	3.5	67	41.4	0	2	56	M	1	51.6	4.2	2.7
66	4.2	61	43.3	0	1	58	M	1	68.5	7.0	6.1
67	3.0	61	38.2	0	4	75	F	1	49.0	4.2	2.8
68	3.3	73	35.9	0	4	73	F	1	45.8	3.9	2.4
69	4.8	60	38.1	0	3	60	F	1	80.3	5.0	3.1
70	2.8	54	42.3	0	2	73	F	1	51.5	4.7	3.5

Appendix Table 2 (continued)

71	4.9	79	42.9	0	2	55	F	1	62.3	4.6	3.0
72	3.2	44	43.8	0	1	56	M	1	71.9	4.9	3.2
73	2.9	59	45.5	0	0	50	M	2	49.9	4.6	3.4
74	6.4	101	44.2	0	2	62	M	1	63.8	5.0	3.6
75	4.4	50	40.0	0	1	50	M	1	88.0	5.8	4.2
76	5.0	70	40.0	0	2	60	M	2	70.9	5.9	4.7
77	4.9	49	45.8	0	4	61	M	1	100.4	5.4	3.2
78	2.4	56	36.1	0	3	75	F	1	42.0	4.1	2.9
79	4.4	62	41.5	0	3	67	M	1	70.8	5.0	3.4
80	4.3	69	49.2	0	0	65	M	1	62.9	4.5	2.8
81	2.6	51	44.0	0	1	54	M	1	50.1	5.5	4.6
82	4.7	63	37.2	0	1	59	F	1	75.3	4.7	2.7
83	5.0	90	44.0	0	3	45	M	1	55.3	5.2	4.1
84	1.9	52	37.0	0	0	41	M	1	36.4	3.9	2.8
85	3.2	62	45.0	0	1	52	M	1	51.5	4.7	3.5
86	4.0	81	33.1	0	0	65	M	1	49.6	4.1	2.6
87	2.3	57	42.5	0	3	66	F	1	39.6	3.8	2.5
88	2.5	53	36.1	0	2	74	F	1	48.1	4.3	3.0
89	4.5	64	36.7	0	4	69	F	1	70.1	4.5	2.5
90	1.9	51	38.5	0	3	73	F	1	38.2	3.6	2.2
91	8.3	111	43.1	0	1	64	M	1	75.1	5.2	3.6
92	2.8	71	38.1	0	4	78	F	1	40.0	3.7	2.3
93	4.6	57	40.8	0	1	46	M	1	80.5	4.8	2.7
94	3.7	57	45.8	0	1	62	M	1	65.7	5.1	3.7
95	3.6	67	46.1	0	0	68	M	1	53.1	4.8	3.6
96	2.3	53	44.7	0	2	59	F	1	43.6	3.9	2.5
97	4.6	63	42.4	0	1	73	M	1	73.4	5.3	3.8
98	1.5	95	47.0	0	1	67	M	2	15.6	4.0	3.6
99	2.7	61	41.3	0	2	72	M	1	44.7	4.1	2.8
100	3.9	45	46.7	0	2	56	M	1	85.8	5.7	4.1
101	3.7	68	38.5	0	2	73	F	1	54.5	4.5	3.1
102	4.5	67	47.9	0	1	67	M	2	67.1	5.4	4.1
103	7.3	72	41.4	0	3	55	F	1	102.0	5.0	2.2
104	3.9	102	33.9	0	2	55	M	2	38.6	4.9	4.1
105	3.8	70	42.1	0	3	55	F	1	53.7	5.8	4.9
106	5.5	62	46.2	0	1	65	M	1	87.9	5.3	3.4
107	4.6	64	35.6	0	1	63	M	1	71.9	4.9	3.2
108	5.1	68	30.4	0	0	70	F	1	75.3	4.7	2.7
109	4.7	89	45.8	0	2	66	M	1	52.7	4.4	3.0
110	2.9	62	47.0	0	1	64	M	1	46.7	4.4	3.2
111	2.1	65	53.6	0	1	68	M	1	32.4	3.8	2.8
112	2.8	57	47.7	0	1	66	M	1	49.0	4.2	2.8

Appendix Table 2 (continued)

113	3.6	54	47.6	0	2	75	M	1	66.6	4.8	3.2
114	2.7	63	41.8	0	0	73	F	2	42.1	4.3	3.2
115	4.4	71	34.3	0	3	56	F	1	61.4	4.7	3.2
116	4.7	73	40.1	0	2	69	M	2	63.8	5.0	3.6
117	8.7	132	42.8	0	2	56	F	3	65.7	5.1	3.7
118	4.4	65	40.3	0	2	68	M	2	67.4	5.0	3.5
119	3.2	70	43.0	0	2	66	M	1	45.8	3.9	2.4
120	2.4	45	40.1	0	0	52	M	2	52.5	5.7	4.8
121	2.4	60	38.3	0	3	73	M	1	40.4	4.7	3.8
122	4.9	70	43.2	0	1	47	M	1	70.1	4.7	2.9
123	8.1	79	39.8	0	2	71	F	1	103.1	5.3	2.9
124	2.8	62	45.4	0	3	78	F	1	45.2	4.3	3.1
125	3.9	79	34.5	0	3	58	M	1	48.9	5.4	4.5
126	4.8	111	44.1	0	2	63	F	2	42.9	4.6	3.6
127	4.4	70	42.5	0	3	77	M	1	63.4	4.8	3.3
128	4.4	62	39.7	0	3	55	F	1	71.5	4.4	2.2

## Appendix D.2 Calculated Hemodynamic and Appearance Indices

Appendix Table 3 Hemodynamic and appearance indices

$t_m$ : Mean residence time;  $C_\infty$ : Asymptotic concentration;  $ACI$ : Appearance complexity index;  $\tau$ : exponential decay time constant;  $a$ : exponential decay coefficient.

	$t_m$ (s)	$C_\infty$ (%)	$\tau_1$ (s)	$\tau_2$ (s)	$\tau_3$ (s)	$a_1$	$a_2$	$a_3$	$ACI$	Traditional Category
1	702.7	13.0	64.29	329.0	2655	0.34	0.36	0.18	1.02	ChickenWing
2	518.3	11.7	12.00	280.0	4043	0.62	0.16	0.10	0.72	ChickenWing
3	465.4	5.4	4.32	231.3	3461	0.67	0.16	0.12	1.35	ChickenWing
4	179.1	6.8	2.08	205.8	2780	0.83	0.05	0.06	0.42	Windsock
5	145.3	0.7	5.23	174.0	1608	0.72	0.21	0.07	0.37	Cactus
6	761.3	12.0	3.57	268.8	8731	0.74	0.07	0.07	0.85	Windsock
7	692.9	7.0	8.10	212.2	6002	0.71	0.12	0.10	0.46	Cauliflower
8	677.0	4.3	24.29	358.7	2790	0.50	0.27	0.19	0.30	Cactus
9	813.9	10.6	1.97	107.3	4059	0.63	0.09	0.18	0.80	ChickenWing
10	1136.0	27.5	23.79	363.7	4559	0.36	0.20	0.16	0.96	Cauliflower

Appendix Table 3 (continued)

11	2362.4	15.1	47.87	445.0	8771	0.43	0.20	0.22	1.03	Windsock
12	492.3	25.3	27.08	349.1	3168	0.50	0.16	0.09	1.25	Windsock
13	245.7	4.8	1.87	340.3	3307	0.79	0.10	0.06	0.45	Cauliflower
14	505.2	9.1	4.12	255.2	3393	0.65	0.13	0.12	0.39	Cauliflower
15	153.3	1.6	3.37	257.0	2200	0.82	0.11	0.05	0.74	Cauliflower
16	1162.3	14.5	28.57	324.0	8124	0.59	0.15	0.11	0.51	Cactus
17	861.8	9.2	10.47	309.3	5344	0.60	0.17	0.14	0.66	Windsock
18	925.6	32.7	32.02	478.8	4569	0.40	0.15	0.12	0.84	ChickenWing
19	173.9	3.7	4.99	185.0	2711	0.79	0.12	0.05	0.58	Cauliflower
20	830.4	8.6	22.63	351.9	4940	0.57	0.21	0.14	0.47	Cauliflower
21	1073.9	7.2	8.01	271.2	7565	0.68	0.12	0.13	0.83	Cauliflower
22	1234.3	24.4	30.51	500.8	4239	0.40	0.16	0.20	1.62	Windsock
23	815.3	18.2	15.13	174.5	2808	0.43	0.16	0.22	0.83	ChickenWing
24	1276.5	18.8	16.78	194.3	4749	0.43	0.17	0.21	0.36	Cauliflower
25	615.2	14.0	5.68	290.8	2795	0.56	0.13	0.17	0.81	ChickenWing
26	102.5	1.9	1.42	241.3	2727	0.90	0.05	0.03	0.83	Windsock
27	91.7	1.1	11.26	171.8	2133	0.85	0.11	0.03	0.51	Cactus
28	571.0	13.8	14.25	286.2	2875	0.48	0.24	0.15	0.93	Cactus
29	416.2	14.2	6.06	301.8	3465	0.64	0.13	0.09	0.53	Windsock
30	135.4	11.8	10.69	183.9	1936	0.67	0.17	0.04	0.95	Cactus
31	366.9	3.4	7.77	265.9	3762	0.74	0.14	0.08	1.09	ChickenWing
32	362.2	7.1	7.06	282.1	2745	0.65	0.18	0.10	0.69	Cauliflower
33	321.5	26.1	12.19	222.1	2948	0.48	0.19	0.06	1.04	ChickenWing
34	2877.2	20.7	14.82	339.9	13317	0.51	0.12	0.17	0.96	ChickenWing
35	876.0	15.9	18.60	260.6	4249	0.50	0.18	0.16	0.37	Cauliflower
36	10.9	0.0	2.61	37.6	587	0.91	0.08	0.01	0.81	Cactus
37	653.4	12.9	1.91	89.8	2939	0.62	0.06	0.19	0.82	ChickenWing
38	467.9	20.5	22.52	304.4	3285	0.51	0.19	0.09	0.98	Cactus
39	324.8	7.3	9.40	350.9	3605	0.75	0.11	0.07	0.62	Cactus
40	605.6	8.3	8.08	349.5	3489	0.60	0.18	0.14	0.24	Cactus
41	575.0	12.6	19.21	309.9	3464	0.53	0.23	0.12	0.98	Windsock
42	302.7	9.0	9.30	246.4	2920	0.66	0.17	0.08	0.86	ChickenWing
43	231.1	10.6	6.37	253.3	3313	0.76	0.08	0.05	1.46	Windsock
44	292.4	10.2	1.40	252.0	3841	0.76	0.07	0.06	0.64	ChickenWing
45	402.8	5.2	4.05	160.3	3727	0.74	0.11	0.10	1.52	Cauliflower
46	407.9	17.0	12.15	317.9	3090	0.58	0.15	0.09	1.10	Windsock
47	649.0	30.8	30.54	364.2	3687	0.44	0.15	0.10	1.25	Cauliflower
48	675.4	11.1	8.07	275.7	3059	0.45	0.27	0.17	0.86	ChickenWing
49	241.1	4.8	2.04	279.4	5684	0.86	0.05	0.04	1.29	Cactus
50	6.5	0.0	1.21	16.3	211	0.83	0.15	0.01	1.07	Cauliflower
51	514.4	11.8	11.25	247.3	2724	0.46	0.28	0.14	0.98	Windsock
52	94.9	0.4	3.64	153.0	1256	0.80	0.14	0.06	0.48	Cactus

Appendix Table 3 (continued)

53	736.0	7.5	13.22	462.5	3163	0.45	0.31	0.17	0.42	Cauliflower
54	833.1	16.2	25.09	353.8	3403	0.48	0.18	0.18	0.82	Cauliflower
55	1020.3	12.1	30.87	489.5	3769	0.42	0.26	0.20	0.78	Cauliflower
56	624.1	8.4	8.81	370.7	4084	0.68	0.11	0.13	1.01	Cauliflower
57	488.7	11.5	9.29	274.2	4530	0.68	0.11	0.09	0.68	Cauliflower
58	505.7	13.9	9.81	192.7	4282	0.60	0.17	0.09	0.80	Windsock
59	991.8	5.6	3.28	150.6	6411	0.72	0.08	0.14	1.08	Cauliflower
60	100.7	3.3	1.88	219.8	2619	0.84	0.09	0.03	0.56	Cauliflower
61	794.4	12.4	10.66	350.4	5250	0.61	0.15	0.12	0.60	Cauliflower
62	61.8	2.7	1.28	211.7	1741	0.86	0.09	0.02	0.92	Cauliflower
63	3374.5	20.3	27.64	#####	10350	0.24	0.38	0.18	0.77	Cactus
64	1094.9	15.3	16.97	814.1	4535	0.44	0.25	0.16	0.61	Cactus
65	397.0	5.6	4.06	184.4	3017	0.72	0.11	0.12	0.45	Cactus
66	696.6	21.9	49.55	428.3	3479	0.45	0.21	0.12	1.10	Cactus
67	940.1	15.2	11.02	213.7	5951	0.60	0.12	0.13	0.84	ChickenWing
68	968.5	25.6	31.84	422.9	5374	0.45	0.18	0.12	1.08	Windsock
69	314.5	6.8	4.43	254.7	4072	0.77	0.09	0.07	1.00	Windsock
70	909.0	10.2	44.46	327.3	5209	0.57	0.19	0.14	0.70	Cactus
71	124.3	1.8	6.36	192.5	2185	0.83	0.11	0.04	0.85	ChickenWing
72	1567.8	22.6	42.20	#####	4798	0.34	0.24	0.20	0.63	Cauliflower
73	144.9	2.5	5.37	115.2	1872	0.78	0.13	0.07	0.56	Cauliflower
74	195.4	5.1	5.27	196.7	4389	0.81	0.10	0.04	0.59	Windsock
75	434.7	11.6	14.49	266.2	3208	0.60	0.18	0.10	0.50	Cauliflower
76	334.9	12.9	12.54	238.1	2637	0.59	0.19	0.09	1.35	Cactus
77	95.0	3.2	1.15	184.5	2689	0.88	0.05	0.03	0.53	Cactus
78	1265.1	8.5	11.74	837.5	4016	0.33	0.37	0.21	0.79	Cauliflower
79	561.4	10.1	9.87	229.9	5568	0.67	0.14	0.08	0.86	Windsock
80	504.0	3.6	3.34	136.8	4299	0.77	0.08	0.11	1.19	Cactus
81	1124.1	21.2	41.17	450.7	3917	0.37	0.22	0.20	1.50	ChickenWing
82	555.1	11.4	6.68	249.0	4718	0.62	0.18	0.09	1.07	Cauliflower
83	174.3	2.3	5.49	180.2	2532	0.79	0.13	0.06	0.65	Windsock
84	670.1	8.9	19.03	300.7	3007	0.48	0.25	0.17	0.35	Cactus
85	338.8	4.6	3.72	224.4	4210	0.75	0.13	0.07	0.92	Cauliflower
86	617.9	11.4	7.60	201.9	3070	0.60	0.12	0.17	0.63	Cactus
87	525.3	10.0	9.46	242.9	3325	0.52	0.26	0.12	0.71	Cauliflower
88	329.2	2.0	12.67	289.8	2278	0.62	0.25	0.11	0.69	Cactus
89	282.8	5.0	3.80	145.4	2688	0.77	0.08	0.09	1.04	ChickenWing
90	1682.3	14.1	6.20	79.8	3924	0.33	0.17	0.36	0.72	Cauliflower
91	478.0	10.3	3.31	328.8	3099	0.66	0.11	0.13	0.75	Windsock
92	1626.7	31.9	6.14	175.6	4759	0.33	0.13	0.23	1.04	ChickenWing
93	1030.7	27.3	21.31	413.8	4160	0.39	0.18	0.16	0.86	Cactus
94	1917.4	8.9	14.42	342.5	7025	0.56	0.11	0.24	0.59	Cactus

Appendix Table 3 (continued)

95	755.3	18.6	14.21	335.7	4832	0.53	0.17	0.11	0.43	Cauliflower
96	618.9	16.6	5.24	198.8	2634	0.56	0.09	0.19	0.57	Windsock
97	204.4	4.8	4.49	129.9	2445	0.75	0.13	0.07	0.89	ChickenWing
98	1461.5	30.6	58.22	583.2	3912	0.26	0.21	0.22	0.84	Windsock
99	264.6	1.3	8.12	214.9	2672	0.72	0.19	0.08	0.40	Cactus
100	1042.2	9.8	10.12	368.9	3984	0.50	0.18	0.22	1.01	ChickenWing
101	346.0	5.9	9.98	201.2	3157	0.68	0.17	0.09	0.59	Cauliflower
102	487.0	7.7	9.66	203.0	3187	0.64	0.16	0.13	0.83	Windsock
103	189.9	5.6	1.23	249.9	4021	0.87	0.04	0.04	1.17	ChickenWing
104	169.1	2.2	5.88	204.8	1881	0.76	0.15	0.07	0.65	Cauliflower
105	1090.1	22.3	23.11	412.1	4040	0.40	0.19	0.19	0.94	Windsock
106	355.7	14.1	6.49	263.2	4845	0.70	0.11	0.06	1.16	Windsock
107	464.9	6.4	4.73	341.1	3118	0.71	0.10	0.13	0.58	Cauliflower
108	235.6	15.0	1.79	114.1	2264	0.71	0.05	0.09	0.82	ChickenWing
109	335.2	3.6	13.16	222.6	2426	0.63	0.22	0.11	0.89	ChickenWing
110	636.7	17.0	16.40	352.5	5068	0.53	0.21	0.09	0.61	Windsock
111	770.4	17.5	53.94	422.6	3722	0.41	0.29	0.13	1.27	ChickenWing
112	1065.7	30.3	17.48	537.4	3824	0.35	0.18	0.17	0.50	ChickenWing
113	377.7	9.3	3.90	147.5	3223	0.72	0.08	0.10	0.68	Cauliflower
114	304.5	38.2	10.21	195.0	2825	0.44	0.12	0.06	1.15	ChickenWing
115	183.0	7.8	5.29	221.1	2428	0.74	0.12	0.06	0.98	Cauliflower
116	336.3	26.0	14.04	251.9	3226	0.50	0.18	0.06	0.60	Windsock
117	16.8	0.1	1.67	52.8	1114	0.93	0.06	0.01	0.70	Cauliflower
118	373.7	4.4	8.87	254.9	2665	0.66	0.19	0.11	1.76	ChickenWing
119	323.0	32.8	8.60	259.8	2622	0.50	0.10	0.07	2.17	ChickenWing
120	869.1	30.8	43.60	422.6	3329	0.33	0.21	0.15	0.73	Windsock
121	551.9	8.6	10.53	279.9	3074	0.61	0.16	0.15	0.74	Windsock
122	230.7	2.9	2.65	243.4	2839	0.79	0.11	0.07	0.75	Cactus
123	270.3	3.6	2.50	181.7	4640	0.85	0.06	0.05	0.68	Cauliflower
124	335.0	10.7	6.95	284.2	3520	0.68	0.14	0.07	0.69	Cauliflower
125	206.5	3.0	8.18	207.9	2393	0.74	0.16	0.07	1.45	Windsock
126	80.3	4.2	1.89	129.1	3847	0.89	0.05	0.02	0.70	ChickenWing
127	276.4	3.8	6.49	264.2	3717	0.80	0.10	0.06	0.59	Cauliflower
128	224.2	2.9	1.93	187.9	5012	0.87	0.06	0.04	0.74	Windsock

## Bibliography

- Abecasis, J., Dourado, R., Ferreira, A., Saraiva, C., Cavaco, D., Santos, K.R., et al. (2009). Left Atrial Volume Calculated By Multi-detector Computed Tomography May Predict Successful Pulmonary Vein Isolation in Catheter Ablation of Atrial Fibrillation. *EP Europace*. 11, 1289-94. doi: 10.1093/europace/eup198
- Aguado, A.M., Olivares, A.L., Yagüe, C., Silva, E., Nuñez-García, M., Fernandez-Quilez, Á., et al. (2019). In silico Optimization of Left Atrial Appendage Occluder Implantation Using Interactive and Modeling Tools. *Frontiers in Physiology*. 10. doi: 10.3389/fphys.2019.00237
- Al-Saady, N.M., Obel, O.A., and Camm, A.J. (1999). Left Atrial Appendage: Structure, Function, And Role in Thromboembolism. *Heart*. 82, 547-54. doi: 10.1136/hrt.82.5.547
- Amin, A., Houmsse, A., Ishola, A., Tyler, J., and Houmsse, M. (2016). The Current Approach of Atrial Fibrillation Management. *Avicenna J Med*. 6, 8-16. doi: 10.4103/2231-0770.173580
- Apostolakis, E., Papakonstantinou, N.A., Baikoussis, N.G., Koniari, I., and Papadopoulos, G. (2013). Surgical Strategies and Devices for Surgical Exclusion of the Left Atrial Appendage: A Word of Caution. *Journal of Cardiac Surgery*. 28, 199-206. doi 10.1111/jocs.12055
- Beigel, R., Wunderlich, N.C., Ho, S.Y., Arsanjani, R., and Siegel, R.J. (2014). The Left Atrial Appendage: Anatomy, Function, and Noninvasive Evaluation. *JACC: Cardiovascular Imaging*. 7, 1251-65. doi: 10.1016/j.jcmg.2014.08.009
- Beinart, R., Heist, E.K., Newell, J.B., Holmvang, G., Ruskin, J.N., and Mansour, M. (2011). Left Atrial Appendage Dimensions Predict the Risk of Stroke/TIA in Patients With Atrial Fibrillation. *Journal of Cardiovascular Electrophysiology*. 22, 10-5. doi: 10.1111/j.1540-8167.2010.01854.x
- Bernsdorf, J., Harrison, S.E., Smith, S.M., Lawford, P.V., and Hose, D.R. (2006). Numerical Simulation of Clotting Processes: A Lattice Boltzmann Application in Medical Physics. *Mathematics and Computers in Simulation*. 72, 89-92. doi: 10.1016/j.matcom.2006.05.008
- Berruezo, A., Tamborero, D., Mont, L., Benito, B., Tolosana, J.M., Sitges, M., et al. (2007). Pre-procedural Predictors of Atrial Fibrillation Recurrence After Circumferential Pulmonary Vein Ablation. *European Heart Journal*. 28, 836-41. doi: 10.1093/eurheartj/ehm027
- Bieging, E.T., Morris, A., Chang, L., Dagher, L., Marrouche, N.F., and Cates, J. (2021). Statistical Shape Analysis of the Left Atrial Appendage Predicts Stroke in Atrial Fibrillation. *The International Journal of Cardiovascular Imaging*. doi: 10.1007/s10554-021-02262-8

- Bisson, A., Bernard, A., Bodin, A., Clementy, N., Babuty, D., Lip, G.Y.H., et al. (2019). Stroke and Thromboembolism in Patients With Atrial Fibrillation and Mitral Regurgitation. *Circulation: Arrhythmia and Electrophysiology*. 12, e006990. doi: 10.1161/CIRCEP.118.006990
- Bosi, G.M., Cook, A., Rai, R., Menezes, L.J., Schievano, S., Torii, R., et al. (2018). Computational Fluid Dynamic Analysis of the Left Atrial Appendage to Predict Thrombosis Risk. *Frontiers in Cardiovascular Medicine*. 5. doi: 10.3389/fcvm.2018.00034
- Boyle, P.M., del Álamo, J.C., and Akoum, N. (2021). Fibrosis, Atrial Fibrillation and Stroke: Clinical Updates and Emerging Mechanistic Models. *Heart*. 107, 99-105. doi: 10.1136/heartjnl-2020-317455
- Calkins, H. (2012). Catheter Ablation to Maintain Sinus Rhythm. *Circulation*. 125, 1439-45. doi: 10.1161/circulationaha.111.019943
- Camm, A.J., Kirchhof, P., Lip, G.Y.H., Schotten, U., Savelieva, I., Ernst, S., et al. (2010). Guidelines for the Management of Atrial Fibrillation: the Task Force for the Management of Atrial Fibrillation of the European Society of Cardiology (Esc). *European Heart Journal*. 31, 2369-429. doi: 10.1093/eurheartj/ehq278
- Camm, A.J., Lip, G.Y.H., De Caterina, R., Savelieva, I., Atar, D., Hohnloser, S.H., et al. (2012). 2012 Focused Update of the Esc Guidelines for the Management of Atrial Fibrillation: an Update of the 2010 Esc Guidelines for the Management of Atrial Fibrillation developed With the Special Contribution of the European Heart Rhythm Association. *European Heart Journal*. 33, 2719-47. doi: 10.1093/eurheartj/ehs253
- Chen, J.-Y., Zhang, A.-D., Lu, H.-Y., Guo, J., Wang, F.-F., and Li, Z.-C. (2013). CHADS2 Versus CHA2DS2-vasc Score in Assessing the Stroke and Thromboembolism Risk Stratification in Patients With Atrial Fibrillation: a Systematic Review and Meta-analysis. *J Geriatr Cardiol*. 10, 258-66. doi: 10.3969/j.issn.1671-5411.2013.03.004
- Chen, P.-S., Chen, L.S., Fishbein, M.C., Lin, S.-F., and Nattel, S. (2014). Role of the Autonomic Nervous System in Atrial Fibrillation: Pathophysiology and Therapy. *Circulation research*. 114, 1500-15. doi: 10.1161/circresaha.114.303772
- Cokelet, G.R., Brown, J.R., Codd, S.L., and Seymour, J.D. (2005). Magnetic Resonance Microscopy Determined Velocity and Hematocrit Distributions in a Couette Viscometer. *Biorheology*. 42, 385-99.
- Curl, R.L., and McMillan, M. (1966). Accuracy in Residence Time Measurements.
- Di Biase, L., Santangeli, P., Anselmino, M., Mohanty, P., Salvetti, I., Gili, S., et al. (2012). Does the Left Atrial Appendage Morphology Correlate With the Risk of Stroke in Patients With Atrial Fibrillation?: Results From a Multicenter Study. *Journal of the American College of Cardiology*. 60, 531-8. doi: 10.1016/j.jacc.2012.04.032

- Doshi, R.N., Daoud, E.G., Fellows, C., Turk, K., Duran, A., Hamdan, M.H., et al. (2005). Left Ventricular-Based Cardiac Stimulation Post AV Nodal Ablation Evaluation (The PAVE Study). *Journal of Cardiovascular Electrophysiology*. 16, 1160-5. doi: 10.1111/j.1540-8167.2005.50062.x
- Dueñas-Pamplona, J., García, J.G., Sierra-Pallares, J., Ferrera, C., Agujetas, R., and López-Mínguez, J.R. (2021a). A Comprehensive Comparison of Various Patient-specific CFD Models of the Left Atrium for Atrial Fibrillation Patients. *Computers in Biology and Medicine*. 133, 104423. doi: 10.1016/j.compbimed.2021.104423
- Dueñas-Pamplona, J., Sierra-Pallares, J., García, J., Castro, F., and Munoz-Paniagua, J. (2021b). Boundary-Condition Analysis of an Idealized Left Atrium Model. *Annals of Biomedical Engineering*. 49, 1507-20. doi: 10.1007/s10439-020-02702-x
- Ernst, G., Stöllberger, C., Abzieher, F., Veit-Dirscherl, W., Bonner, E., Bibus, B., et al. (1995). Morphology of the Left Atrial Appendage. *The Anatomical Record*. 242, 553-61. doi: 10.1002/ar.1092420411
- Esmaily-Moghadam, M., Hsia, T.-Y., and Marsden, A.L. (2013). A Non-discrete Method for Computation of Residence Time in Fluid Mechanics Simulations. *Phys Fluids* (1994). 25, 110802-. doi: 10.1063/1.4819142
- Feng, D., D'Agostino, R.B., Silbershatz, H., Lipinska, I., Massaro, J., Levy, D., et al. (2001). Hemostatic State and Atrial Fibrillation (the Framingham Offspring Study). *The American Journal of Cardiology*. 87, 168-71. doi: 10.1016/S0002-9149(00)01310-2
- Feng, L., Gao, H., Qi, N., Danton, M., Hill, N.A., and Luo, X. (2021). Fluid–Structure Interaction in a Fully Coupled Three-Dimensional Mitral–Atrium–Pulmonary Model. *Biomechanics and Modeling in Mechanobiology*. 20, 1267-95. doi: 10.1007/s10237-021-01444-6
- Fogler, H.S. (2016). "Residence Time Distributions of Chemical Reactors," in *Elements of chemical reaction engineering*, ed. H.S. Fogler (Boston, Massachusetts, USA: Prentice Hall), 767-806. <https://learning.oreilly.com/library/view/elements-of-chemical/9780135486252/>
- Formaggia, L., Quarteroni, A., and Veneziani, A. (2010). *Cardiovascular Mathematics: Modeling and simulation of the circulatory system*, ed. Springer Science & Business Media).
- García-Villalba, M., Rossini, L., Gonzalo, A., Vigneault, D., Martinez-Legazpi, P., Durán, E., et al. (2021). Demonstration of Patient-Specific Simulations to Assess Left Atrial Appendage Thrombogenesis Risk. *Frontiers in Physiology*. 12. doi: 10.3389/fphys.2021.596596
- Gloekler, S., Saw, J., Koskinas, K.C., Kleinecke, C., Jung, W., Nietlispach, F., et al. (2017). Left Atrial Appendage Closure for Prevention of Death, Stroke, and Bleeding in Patients With Nonvalvular Atrial Fibrillation. *International Journal of Cardiology*. 249, 234-46. doi: 10.1016/j.ijcard.2017.08.049

- Goff, R.P., Spencer, J.H., and Iaizzo, P.A. (2016). MRI Reconstructions of Human Phrenic Nerve Anatomy and Computational Modeling of Cryoballoon Ablative Therapy. *Annals of Biomedical Engineering*. 44, 1097-106. doi: 10.1007/s10439-015-1379-3
- Heppell, R.M., Berkin, K.E., McLenachan, J.M., and Davies, J.A. (1997). Haemostatic and Haemodynamic Abnormalities Associated With Left Atrial Thrombosis in Non-rheumatic Atrial Fibrillation. *Heart (British Cardiac Society)*. 77, 407-11. doi: 10.1136/hrt.77.5.407
- Holmes, D.R., Reddy, V.Y., Turi, Z.G., Doshi, S.K., Sievert, H., Buchbinder, M., et al. (2009). Percutaneous Closure of the Left Atrial Appendage Versus Warfarin Therapy for Prevention of Stroke in Patients With Atrial Fibrillation: a Randomised Non-inferiority Trial. *The Lancet*. 374, 534-42. doi: 10.1016/s0140-6736(09)61343-x
- Hughes, M., Lip, G.Y.H., primary, o.b.o.t.G.D.G.f.t.N.n.c.g.f.m.o.a.f.i., and care, s. (2007). Risk Factors for Anticoagulation-related Bleeding Complications in Patients With Atrial Fibrillation: a Systematic Review. *QJM: An International Journal of Medicine*. 100, 599-607. doi: 10.1093/qjmed/hcm076
- Hund, S.J., Kameneva, M.V., and Antaki, J.F. (2017). A Quasi-Mechanistic Mathematical Representation for Blood Viscosity. *Fluids*. 2, 10. doi: 10.3390/fluids2010010
- Izenman, A.J. (2008). "Linear Dimensionality Reduction," in *Modern Multivariate Statistical Techniques: Regression, Classification, and Manifold Learning*, ed. (New York, NY: Springer New York), 195-236. doi: 10.1007/978-0-387-78189-1\_7
- January, C.T., Wann, L.S., Alpert, J.S., Calkins, H., Cigarroa, J.E., Cleveland, J.C., et al. (2014). 2014 AHA/ACC/HRS Guideline for the Management of Patients With Atrial Fibrillation: Executive Summary. *Circulation*. 130, 2071-104. doi: 10.1161/cir.0000000000000040
- January, C.T., Wann, L.S., Calkins, H., Chen, L.Y., Cigarroa, J.E., Cleveland, J.C., et al. (2019). 2019 AHA/ACC/HRS Focused Update of the 2014 AHA/ACC/HRS Guideline for the Management of Patients With Atrial Fibrillation: A Report of the American College of Cardiology/American Heart Association Task Force on Clinical Practice Guidelines and the Heart Rhythm Society in Collaboration With the Society of Thoracic Surgeons. *Circulation*. 140, e125-e51. doi: 10.1161/cir.0000000000000665
- Jongnarangsin, K., Chugh, A., Good, E., Mukerji, S., Dey, S., Crawford, T., et al. (2008). Body Mass Index, Obstructive Sleep Apnea, and Outcomes of Catheter Ablation of Atrial Fibrillation. *Journal of Cardiovascular Electrophysiology*. 19, 668-72. doi: 10.1111/j.1540-8167.2008.01118.x
- Kakar, P., Boos, C.J., and Lip, G.Y.H. (2007). Management of Atrial Fibrillation. *Vasc Health Risk Manag*. 3, 109-16. <https://www.ncbi.nlm.nih.gov/pmc/articles/PMC1994040/>
- Kamel, H., Okin, P.M., Elkind, M.S.V., and Iadecola, C. (2016). Atrial Fibrillation and Mechanisms of Stroke. *Stroke*. 47, 895-900. doi: 10.1161/strokeaha.115.012004

- Khurram, I.M., Dewire, J., Mager, M., Maqbool, F., Zimmerman, S.L., Zipunnikov, V., et al. (2013). Relationship Between Left Atrial Appendage Morphology and Stroke in Patients With Atrial Fibrillation. *Heart Rhythm*. 10, 1843-9. doi: 10.1016/j.hrthm.2013.09.065
- Kim, T., Cheer, A.Y., and Dwyer, H.A. (2004). A Simulated Dye Method for Flow Visualization With a Computational Model for Blood Flow. *Journal of Biomechanics*. 37, 1125-36. doi: 10.1016/j.jbiomech.2003.12.028
- Koizumi, R., Funamoto, K., Hayase, T., Kanke, Y., Shibata, M., Shiraishi, Y., et al. (2015). Numerical Analysis of Hemodynamic Changes in the Left Atrium Due to Atrial Fibrillation. *Journal of Biomechanics*. 48, 472-8. doi: 10.1016/j.jbiomech.2014.12.025
- Kundu, P.K., Cohen, I.M., and Dowling, D.R. (2012). "Chapter 4 - Conservation Laws," in *Fluid Mechanics (Fifth Edition)*, ed. P.K. Kundu, I.M. Cohen, D.R. Dowling (Boston: Academic Press), 95-169. doi: 10.1016/b978-0-12-382100-3.10004-6
- Lip, G.Y. (1997). Hypercoagulability and Haemodynamic Abnormalities in Atrial Fibrillation. *Heart (British Cardiac Society)*. 77, 395-6. doi: 10.1136/hrt.77.5.395
- Lip, G.Y.H., and Boos, C.J. (2008). Antithrombotic Treatment in Atrial Fibrillation. *Postgraduate Medical Journal*. 84, 252-8. doi: 10.1136/hrt.2005.066944
- Lip, G.Y.H., Nieuwlaat, R., Pisters, R., Lane, D.A., and Crijns, H.J.G.M. (2010). Refining Clinical Risk Stratification for Predicting Stroke and Thromboembolism in Atrial Fibrillation Using a Novel Risk Factor-Based Approach: The Euro Heart Survey on Atrial Fibrillation. *Chest*. 137, 263-72. doi: 10.1378/chest.09-1584
- Masci, A., Barone, L., Dedè, L., Fedele, M., Tomasi, C., Quarteroni, A., et al. (2019). The Impact of Left Atrium Appendage Morphology on Stroke Risk Assessment in Atrial Fibrillation: A Computational Fluid Dynamics Study. *Frontiers in Physiology*. 9. doi: 10.3389/fphys.2018.01938
- Masci, A., Alessandrini, M., Forti, D., Menghini, F., Dedé, L., Tomasi, C., et al. (2020). A Proof of Concept for Computational Fluid Dynamic Analysis of the Left Atrium in Atrial Fibrillation on a Patient-Specific Basis. *Journal of Biomechanical Engineering*. 142. doi: 10.1115/1.4044583
- Morales, X., Mill, J., Juhl, K.A., Olivares, A., Jimenez-Perez, G., Paulsen, R.R., et al. (2020). Deep Learning Surrogate of Computational Fluid Dynamics for Thrombus Formation Risk in the Left Atrial Appendage. *Cham. Springer International Publishing*. 157-66.
- Morales, X., Mill, J., Simeon, G., Juhl, K.A., De Backer, O., Paulsen, R.R., et al. (2021). Geometric Deep Learning for the Assessment of Thrombosis Risk in the Left Atrial Appendage. *Cham. Springer International Publishing*. 639-49.
- Mozaffarian, D., Benjamin, E.J., Go, A.S., Arnett, D.K., Blaha, M.J., Cushman, M., et al. (2016). Heart Disease and Stroke Statistics—2016 Update. *Circulation*. 133, e38-e360. doi:10.1161/cir.0000000000000350

- Nedios, S., Kornej, J., Koutalas, E., Bertagnolli, L., Kosiuk, J., Rolf, S., et al. (2014). Left Atrial Appendage Morphology and Thromboembolic Risk After Catheter Ablation for Atrial Fibrillation. *Heart Rhythm*. 11, 2239-46. doi: 10.1016/j.hrthm.2014.08.016
- Otani, T., Al-Issa, A., Pourmorteza, A., McVeigh, E.R., Wada, S., and Ashikaga, H. (2016). A Computational Framework for Personalized Blood Flow Analysis in the Human Left Atrium. *Annals of Biomedical Engineering*. 44, 3284-94. doi: 10.1007/s10439-016-1590-x
- Pappone, C., Rosanio, S., Augello, G., Gallus, G., Vicedomini, G., Mazzone, P., et al. (2003). Mortality, Morbidity, and Quality of Life After Circumferential Pulmonary Vein Ablation for Atrial Fibrillation: Outcomes From a Controlled Nonrandomized Long-term Study. *Journal of the American College of Cardiology*. 42, 185-97. doi: 10.1016/S0735-1097(03)00577-1
- Petersen, M., Roehrich, A., Balzer, J., Shin, D.-I., Meyer, C., Kelm, M., et al. (2014). Left Atrial Appendage Morphology Is Closely Associated With Specific Echocardiographic Flow Pattern in Patients With Atrial Fibrillation. *EP Europace*. 17, 539-45. doi: 10.1093/europace/euu347
- Quemada, D. (1978). Rheology of Concentrated Disperse Systems Ii. A Model for Non-Newtonian Shear Viscosity in Steady Flows. *Rheologica Acta*. 17, 632-42.
- Qureshi, A., Darwish, O., Dillon-Murphy, D., Chubb, H., Williams, S., Nechipurenko, D., et al. (2020). Modelling Left Atrial Flow and Blood Coagulation for Risk of Thrombus Formation in Atrial Fibrillation. *2020 Computing in Cardiology*. 1-4. doi: 10.22489/CinC.2020.219
- Rayz, V.L., Bousset, L., Ge, L., Leach, J.R., Martin, A.J., Lawton, M.T., et al. (2010). Flow Residence Time and Regions of Intraluminal Thrombus Deposition in Intracranial Aneurysms. *Annals of Biomedical Engineering*. 38, 3058-69. doi: 10.1007/s10439-010-0065-8
- Reddy, V.Y., Doshi, S.K., Sievert, H., Buchbinder, M., Neuzil, P., Huber, K., et al. (2013). Percutaneous Left Atrial Appendage Closure for Stroke Prophylaxis in Patients With Atrial Fibrillation. *Circulation*. 127, 720-9. doi: 10.1161/circulationaha.112.114389
- Sakellaridis, T., Argiriou, M., Charitos, C., Tsakiridis, K., Zarogoulidis, P., Katsikogiannis, N., et al. (2014). Left Atrial Appendage Exclusion—Where Do We Stand? *Journal of Thoracic Disease*. S70-S7. <https://jtd.amegroups.com/article/view/1935>
- Sanatkhani, S., and Menon, P.G. (2017). "Relating Atrial Appendage Flow Stasis Risk from Computational Fluid Dynamics to Imaging Based Appearance Paradigms for Cardioembolic Risk," in *Imaging for Patient-Customized Simulations and Systems for Point-of-Care Ultrasound*; Lecture Notes in Computer Science, ed. M.J. Cardoso (Québec City, Québec, Canada: Springer), 86-93. doi: 10.1007/978-3-319-67552-7\_11

- Sanatkhani, S., and Menon, P.G. (2018). Generative Statistical Modeling of Left Atrial Appendage Appearance to Substantiate Clinical Paradigms for Stroke Risk Stratification. SPIE Medical Imaging. Houston, Texas, USA. 10574, 105742L.1-L.7. doi: 10.1117/12.2291568
- Sanatkhani, S., Menon, P.G., Shroff, S.G., and Sotirios Nedios (2018). Abstract 11255: Thrombus Risk Prediction in Atrial Fibrillation: Hemodynamic Model of Left Atrial Appendage. AHA Scientific Sessions. Circulation. 138, A11255. doi: 10.1161/circ.138.suppl\_1.11255
- Sanatkhani, S., Oladosu, M., Chera, K., Nedios, S., and Menon, P. (2018). Relating Regional Characteristics of Left Atrial Shape to Presence of Scar in Patients With Atrial Fibrillation, ed. SPIE). doi: 10.1117/12.2293947
- Sanatkhani, S., Nedios, S., Menon, P.G., Bollmann, A., Hindricks, G., and Shroff, S.G. (2021). Subject-Specific Calculation of Left Atrial Appendage Blood-Borne Particle Residence Time Distribution in Atrial Fibrillation. Frontiers in Physiology. 12. doi: 10.3389/fphys.2021.633135
- Sánchez-Quintana, D., López-Mínguez, J.R., Macías, Y., Cabrera, J.A., and Saremi, F. (2014). Left Atrial Anatomy Relevant to Catheter Ablation. Cardiol Res Pract. 2014, 289720-. doi: 10.1155/2014/289720
- Scarano, F. (2012). Tomographic PIV: Principles and Practice. Measurement Science and Technology. 24, 012001. doi: 10.1088/0957-0233/24/1/012001
- Shimizu, A., and Centurion, O.A. (2002). Electrophysiological Properties of the Human Atrium in Atrial Fibrillation. Cardiovascular Research. 54, 302-14. doi: 10.1016/s0008-6363(02)00262-6
- Sierra-Pallares, J., Méndez, C., García-Carrascal, P., and Castro, F. (2017). Spatial Distribution of Mean Age and Higher Moments of Unsteady and Reactive Tracers: Reconstruction of Residence Time Distributions. Applied Mathematical Modelling. 46, 312-27. doi 10.1016/j.apm.2017.01.054
- Tanne, D., Bertrand, E., Pibarot, P., and Rieu, R. (2008). Asymmetric Flows in an Anatomical-shaped Left Atrium by 2C-3D+t PIV Measurements. Computer Methods in Biomechanics and Biomedical Engineering. 11, 209-11. doi: 10.1080/10255840802298943
- Vainrib, A.F., Bamira, D.G., and Saric, M. (2017). Percutaneous Left Atrial Appendage Closure Devices. Current Cardiovascular Imaging Reports. 10, 40. doi: 10.1007/s12410-017-9437-x
- Vella, D., Monteleone, A., Musotto, G., Bosi, G.M., and Burriesci, G. (2021). Effect of the Alterations in Contractility and Morphology Produced by Atrial Fibrillation on the Thrombosis Potential of the Left Atrial Appendage. Frontiers in Bioengineering and Biotechnology. 9. doi: 10.3389/fbioe.2021.586041

- Virani, S.S., Alonso, A., Benjamin, E.J., Bittencourt, M.S., Callaway, C.W., Carson, A.P., et al. (2020). Heart Disease and Stroke Statistics---2020 Update: A Report From the American Heart Association. *Circulation*. 141, e139-e596. doi: 10.1161/cir.0000000000000757
- Wang, Y., Di Biase, L., Horton, R.P., Nguyen, T., Morhanty, P., and Natale, A. (2010). Left Atrial Appendage Studied by Computed Tomography to Help Planning for Appendage Closure Device Placement. *Journal of Cardiovascular Electrophysiology*. 21, 973-82. doi: 10.1111/j.1540-8167.2010.01814.x
- Yaghi, S., Chang, A.D., Hung, P., Mac Grory, B., Collins, S., Gupta, A., et al. (2018). Left Atrial Appendage Morphology and Embolic Stroke of Undetermined Source: A Cross-Sectional Multicenter Pilot Study. *Journal of Stroke and Cerebrovascular Diseases*. 27, 1497-501. doi: 10.1016/j.jstrokecerebrovasdis.2017.12.036
- Yaghi, S., Chang, A.D., Akiki, R., Collins, S., Novack, T., Hemendinger, M., et al. (2020). The Left Atrial Appendage Morphology Is Associated With Embolic Stroke Subtypes Using a Simple Classification System: a Proof of Concept Study. *Journal of Cardiovascular Computed Tomography*. 14, 27-33. doi: 10.1016/j.jcct.2019.04.005
- Ye, T., Zhang, X., Li, G., and Wang, S. (2020). Biomechanics in Thrombus Formation From Direct Cellular Simulations. *Physical Review E*. 102, 042410. doi: 10.1103/physreve.102.042410
- Zhang, L.T., and Gay, M. (2008). Characterizing Left Atrial Appendage Functions in Sinus Rhythm and Atrial Fibrillation Using Computational Models. *Journal of Biomechanics*. 41, 2515-23. doi: 10.1016/j.jbiomech.2008.05.012
- Zheng, X., Yazdani, A., Li, H., Humphrey, J.D., and Karniadakis, G.E. (2020). A Three-dimensional Phase-field Model for Multiscale Modeling of Thrombus Biomechanics in Blood Vessels. *PLOS Computational Biology*. 16, e1007709. doi: 10.1371/journal.pcbi.1007709